Development of a New Rapid Screening Method for High Throughput Electrochemical Characterization of NiMo Hydrogen Evolution Catalysts

By

Timothy D. McDonald

B.A. Chemistry, Saint Mary's University of Minnesota, Minnesota, USA 2012
B.A. Engineering Physics, Saint Mary's University of Minnesota, Minnesota, USA 2012

Submitted to the graduate degree program in Chemical & Petroleum Engineering and the Graduate Faculty of the University of Kansas in partial fulfillment of the requirements for the degree of Master of Science

Committee Members

_____

Dr. Kevin Leonard, Committee Chair

_____

Dr. Karen Nordheden

_____

Dr. Raghunath V. Chaudhari

Date Defended: March 27th, 2015

The Thesis Committee for Timothy D. McDonald

certifies that this is the approved version of the following thesis:

Development of a New Rapid Screening Method for High Throughput Electrochemical Characterization of NiMo Hydrogen Evolution Catalysts

_____

Dr. Kevin Leonard, Committee Chair

Date approved: April 16th, 2015

ABSTRACT

In order to effectively study new electrocatalysts for hydrogen evolution (using water as a renewable and clean feedstock) new advancements must be made with the analytic techniques used to characterize these electrocatalysts. In this thesis, two new methods are presented for measuring heterogeneous electrocatalyst electron transfer kinetics. The first of these methods is intended to advance the capabilities of high throughput rapid screening methods for electrocatalysts. By using piezoelectric printing, precursors for metal and metal oxide catalysts are printed onto a substrate, yielding arrays of 64 catalyst samples to be analyzed by linear sweep voltammetry (LSV). Combining piezoelectric printing technologies with automated process controls (used to control the electrochemical reaction systems) and automated high throughput COMSOL Multiphysics simulations allows for the number of catalyst samples that can be measured in one set are increased exponentially compared to other methods capable of returning kinetic parameter data (k^0_{eff}) without sample crosstalk. To verify the capabilities of this method, 2% incremental composition NiMo bimetallic hydrogen evolution catalyst arrays (from 100% Ni to 100% Mo) were studied in both acidic and neutral pH electrolyte solutions, yielding catalytic reactivity maps of the composition arrays. For the acidic reaction conditions, peak activity of the NiMo catalyst occurred in the composition range of 78-90% Ni, whereas for the neutral reaction conditions, peak activity regions occurred at 12-18% Ni and 46-62% Ni.

The second method of measuring kinetics of electron transfer reactions is an improved controls system for Scanning Electrochemical Microscopy (SECM) motion control. To improve the efficiency of the SECM approach for electrodes, a new variable

approach speed technique was developed to employ custom fuzzy logic control algorithms for automatically adjusting the speed of approach for the electrode based on tip size, detection method, enhancement factor, and distance of the electrode tip from the set-point. This algorithm is able to automatically switch from a coarse to a fine motion controller when the tip electrode is sufficiently close to the substrate. We validated that approach curves obtained using the fuzzy logic algorithm matched well with simulated approach curves for both large microelectrodes (d = 175 μm) and for conventional SECM ultramicroelectrodes (d = 6.2 μm and d = 4.2 μm). Using positive feedback approach curves, we obtained a tip/substrate gap distance of 6.5 μm for the 175 μm electrode, 800 nm for the 6.2 μm electrode, and 580 nm for the 4.2 μm electrode. The gap distances were obtained using the fuzzy logic control algorithm in roughly one-third of the time compared to the conventional constant-speed approach method. Also, the gap distances were closer using the fuzzy logic algorithm, with the 4.2 μm electrode gap being 120 nm smaller than the constant-speed approach method. In addition, at the 580 nm gap distance obtained with the fuzzy logic algorithm, linear sweep voltammetry was performed allowing us to quantify the kinetic rate constant (k^0) for the oxidation reaction of ferrocenemethanol to be 0.20 ± 0.05 cm s^{-1}.

ACKNOWLEDGMENTS

I would like to acknowledge Dr. Kevin Leonard, Dr. Karen Nordheden, and Dr. Raghunath V. Chaudhari for serving on my thesis committee as well as advising and helping me throughout my time as a graduate student at the University of Kansas. Dr. Nordheden provided me with the opportunity to prove my capabilities as an engineering student, for which I am eternally grateful. Dr. Leonard, my research adviser and PI, helped me learn an extensive amount of electrochemistry, code writing, reaction simulation, and process controls, as well as other valuable skills above and beyond the standard curriculum. He also proved to be an outstanding adviser, always involved and willing to have ideas bounced off of him and always the optimist, it was nothing short of a pleasure to work in his lab. Dr. Chaudhari served as an invaluable resource within the department and an outstanding Graduate Adviser.

I would also like to acknowledge the other members of the Center for Environmentally Beneficial Catalysis (CEBC) for their collaborative efforts and willingness to aid in instrumental techniques and helping me learn skills. Ed Atchison collaborated with reactor designs, schematics, machining, and electronics. Dr. Xin Jin lent his expertise to guide me through learning to use instrumentation. I would like to acknowledge my fellow graduate student in Dr. Leonard's group, Joe Barforoush, for his collaboration and related lab work. Also, the undergraduate researchers involved with my projects and research deserve acknowledgement; Cal Bayer, Tej Desai, Maeley Brown, and Anne Marie DeLee, who between them worked with me on many aspects of the research presented in this thesis. The many other members of the CEBC also deserve thanks for

their help throughout my time at KU. And a special thanks to Carol Miner who was a wealth of knowledge for all administrative and departmental procedure.

Finally, I would like to thank God for standing by me and giving me strength during my many all-nighters during Thermo season. I would be amiss if I did not acknowledge my family for being an unrelenting support for me during my study, especially my eldest brother, Ben, who through his experiences helped me decide which path I wanted to follow through school and research. The lessons I have learned through watching my family members achieve graduate degrees and excel in industry have proved to have immeasurable worth and application. If there is one person worth acknowledging the most, it would be my loving mother, who somehow managed to make sure all of her children would live up to their potential, never taking any opportunity for granted. She has raised a brood of world conquering giants, and for that I am grateful.

TABLE OF CONTENTS

LIST OF FIGURES

LIST OF TABLES

CHAPTER 2

CHAPTER 1: INTRODUCTION

Production of hydrogen gas is important for industrial chemical production methods, being used in the production of many highly consumed chemicals, such as ammonia and methanol, as well as many other applications including refining oil and boosting octane and reducing sulfur content. According to an Argonne National Laboratory market forecast of the hydrogen market, by 2003 consumption of hydrogen for industrial chemical processes had surpassed 40 million metric tons, and is expected to continue growing as energy consumption increases. The other possibility addressed by this study was hydrogen as a main source of transportation fuel. According to the Argonne study, they predict as much as 100 million metric tons of hydrogen being used in transportation, effectively more than tripling the demand for hydrogen from current conditions.[1]

Because of this level of demand on hydrogen, it is important to develop new methods of producing it, diversifying the market and employing new methods that utilize clean chemical processes and renewable feedstocks, such as water.

The current dominating method for hydrogen production is methane steam reforming, producing nearly 50% of hydrogen.[2] Roughly 96% of hydrogen is produced by natural gas, petroleum and coal sources [2], all of which lead to production of CO_2 as a byproduct. With the current ongoing push for clean energy, the sources of energy used to create new technologies must be weaned off of fuels that produce CO_2, otherwise the beneficial impact throughout the lifecycle of these new technologies will be limited by the high cost and emissions from production and manufacturing.

New methods of H_2 production that utilize renewable feedstocks (in the case of this research, water feedstocks are the focus) and eliminate potentially hazardous byproducts, such as greenhouse gases, will provide a better method of implementing clean energy sources in the chemical and petrochemical industries. These range from photocatalytic and electrochemical to hydroelectric, photovoltaic, and wind power. The drawbacks of many of these technologies is the high cost of production, based on the use of components, like silicon,[3] and the limitations on viable locations, such as hydroelectric dam locations. Because of this, there has been an effort to find more cost effective components and methods of implementation, making these technologies more economically viable. The goal of my research is to introduce new methods of electrochemically screening cost effective Earth-abundant metal and metal oxide catalyst combinations in a much more efficient manner that returns qualitative data. By accomplishing this feat, the result is an exponential increase in sample throughput for electrocatalyst testing.

CHAPTER 2: Rapid Screening Method for Hydrogen Evolution Electrocatalysts

INTRODUCTION

With current technological shifts in the energy sector focused on development of green energy and renewable energy sources, a need for both renewable fuels and energy storage methods has surfaced. Many of the clean, low greenhouse gas generating energy sources being used now (wind, solar, hydroelectric, nuclear, among others), are not easily tailored to efficiently match output with the constantly fluctuating energy demand. In addition, many of these clean energy sources are dependent on unpredictable and inconsistent sources, such as wind and sunlight. Because of these issues, implementation of these technologies is not as efficient as it could be. One method of increasing efficiency is through chemical energy storage, as proposed here, based on hydrogen gas.

Chemical storage of energy is a field that has been growing in recent years; from new developments in battery technologies to concentrating excess energy into value-added chemicals.[4] Depending on what the energy storage goal is, there are many different paths that can be followed to utilize this energy, including biomass conversions, production of value-added chemicals and fuels by means of renewable feedstock, and electrochemical storage as batteries or by water electrolysis.

One chemical used heavily in the production of industrial chemicals, such as methanol and ammonia, is hydrogen gas (H_2). According to a market analysis published by Agonne National Lab about the hydrogen market, over 40 million metric tonnes of hydrogen was consumed by industrial processes in 2003.[1] This amount is expected to

continue growing, especially if hydrogen is ever utilized in the transportation fuel market. Current feedstocks for hydrogen are dominated (~95% of H_2 produced) by methane, which is steam reformed to produce hydrogen gas.

Effective and affordable catalysts for the hydrogen evolution reaction (HER) have been the focus of many recent research ventures. These catalysts could provide an important step forward in the field of renewable energies. Current hydrogen production methods are energy intensive and produce CO_2 and CO as byproducts, such as the steam reforming reactions:[5-6]

$$CH_{4(g)} + 2H_2O_{(g)} \rightarrow CO_{2_{(g)}} + 4H_{2(g)} \qquad \text{(Eq. 2.1)}$$

$$CO_{(g)} + H_2O_{(g)} \rightarrow CO_{2(g)} + H_{2(g)} \qquad \text{(Eq. 2.2)}$$

as well as other reaction byproducts and mechanisms, including over-reacting to form carbon coking, which can deactivate the catalyst.[7] Moreover, the presence of other compounds, such as sulfur, can result in other byproducts that are detrimental to the environment and also play a major role in the deactivation of catalysts.[8]

One possible method of generating hydrogen gas in a cleaner, more controllable method is electrochemical hydrogen evolution. Because of the nature of this reaction it does not have the same issues of producing greenhouse gases as byproducts, as well as being supplied by water as the reaction feedstock. The HER reaction involving protons in electrolytic solution follows the simplified pathway:

$$2H^+_{aqueous} + 2e^-_{aqueous} \rightarrow 2H_{2(g)} \qquad \text{(Eq. 2.3)}$$

But more accurately, the catalyzed reaction follows the surface adsorption reaction model of:

$$H^{+}_{aqueous} + M + e^{-} \rightarrow MH_{adsorbed} \qquad \text{(Eq. 2.4 Volmer Reaction)}$$

$$MH_{adsorbed} + H^{+} + e^{-} \rightarrow H_2 + M \qquad \text{(Eq. 2.5 Heyrovsky Reaction)}$$

$$MH_{adsorbed} + MH_{adsorbed} \rightarrow H_2 + 2M \qquad \text{(Eq. 2.6 Tafel Reaction)}$$

where the required electrons for the reaction are supplied by current through the metal catalyst site, M.[9] The Volmer Reaction occurs first, then either the Heyrovsky Reaction or the Tafel Reaction occurs, with the dominant one depending on the catalyst used and reaction conditions.

Other applications of the HER reaction include the use of renewable clean electricity to convert wind, solar, or hydroelectric power into stored chemical energy by means of electrochemical processes such as artificial photosynthesis.[10-14]

Currently, the best hydrogen evolution catalysts are based on precious metals, namely Pt, which is expensive on an industrial production scale. Efforts to increase the efficiency and affordability of photoelectrochemical energy have led to HER catalysts being investigated for energy storage. In an attempt to create catalyst combinations that optimize performance and cost, the most promising materials have been Earth-abundant transition metal-based catalysts. Most multi-metal catalyst characterization efforts take a substantial amount of time to perform due to the amount of work required for preparing each catalyst composition separately and running individual experiments. In addition, the

catalytic properties of multi-component transition metal catalyst systems cannot be simulated or predicted with any appreciable accuracy with current techniques and technologies, requiring all characterizations to be experimentally completed. Because of this, there has been a recent push to develop faster catalyst screening methods, allowing for a vast amount of data, both physical and catalytic properties, to be more efficiently generated with ease. The overall goal for developing rapid data acquisition is to provide a means of using vast amounts of data to identify trends within catalyst properties (bulk modulus, melting point, crystal structure/lattice spacing, metal combinations, etc.), providing a more knowledgeable basis on which to direct further research without wasting time and resources on non-effective catalysts. There have been attempts to identify trends and compositions of effective catalysts based on physical properties of the metallic elements present[15] but the current amount of data for multi-metallic systems is rather sparse, limiting the scope of application for this approach at this time. Previous research in the area of high throughput catalyst screening has led to multiple methods of qualitative rapid analysis.[16-18] These methods have included bipolar electrode chemistry,[19] parallel multi-reactor cells,[20] rapid throughput scanning in SECM (arrays of catalysts on a single electrode, such as FTO coated glass),[21] gas generation monitoring,[18] and even fiber optic SECM for photoelectric catalysts;[22-24] however, each have their limitations. These limitations present difficulties when characterizing the catalyst in a quantitative method, since the methods are mainly qualitative and require in depth noise corrections for crosstalk and interference with the other samples that are present.

A substantial amount of research has already been done on Nickel/Molybdenum hydrogen evolution reaction catalysts[10, 16, 25-36] which is one reason for it being chosen for

this experiment. In order to validate the function of the rapid screening method presented, a well-studied system was ideal so that results could be compared to prior research and results.

In this paper, an electrochemical method is being proposed that allows for individual catalyst samples to be evaluated by a high-throughput arrayed rapid scanning method, using a system of individually isolated electrodes which eliminates cross-talk between samples and yields quantitative data for analysis of kinetic parameters (rate constant: k^0_{eff}, and charge transfer coefficient: α). Other attempts have been made to eliminate this issue of cross talk between the catalyst samples, such as plating a secondary electrode on the outside of an SECM electrode, allowing for more accurate modeling of the crosstalk and using simulations to eliminate crosstalk and background noise from the data collected.[37]

This new rapid screening method is meant to be an initial step into understanding which catalysts should be investigated at a much more in-depth level. It is a means of high throughput testing to weed out the ineffective catalysts in a more efficient manner so that the more effective ones can be found in less time and then analyzed by more effective means later on. That is not to say that this method does not have potential to become more accurate and analytically feasible, but for the time being it is in early stages of development.

To obtain high quality amperometric and voltammetric data (charge current density…etc), via linear sweep voltammetry, past methods have required a single catalyst being measured to avoid cross-talk with other catalyst depositions that would be present in a high throughput array on FTO glass or another conductive substrate electrode. This

requires a large amount of effort for each sample to be characterized. The proposed method employs a cell with 64 individual and separate electrodes, each capable of hosting a catalyst sample, printed with piezoelectrics on a glass slide. Because each electrode is isolated, the electrodes can be made active or passive by means of a control box, eliminating interference among the catalyst samples and allowing for automated experiment control for 64 runs in one reaction cell setup. This also helps by keeping reaction conditions identical between the 64 different electrodes, since they are in the same electrolytic solution and cell.

The advantages of this method have to do with the ease of fabrication, high-throughput capabilities, the versatility of the materials that can be used, and the ability to get quantitative results. Other methods of printing circuitry have been used to create custom architectures, such as screen printing,[38] inkjet printing,[39] aerosol precursor applications[40] lithographic techniques,[41] and sputter coating,[42] but the printing resolution requirements of this system are roughly on the tens of microns range, which is easily achieved with piezoelectric printing. In addition to meeting our print resolution needs, piezoelectric printing allows for a very customizable and nearly endless amount of precursor inks to be used. Since it works with a wide range of viscosities and surface tensions, this technology allows for a very large amount of experimental leeway when it comes to materials used and the capabilities of the system for future adaptations and uses.

MATERIALS AND METHODS

Chemicals

Tetrachloroethylene (99+% Acros Organics), 1,2-dichlorobenzene (99+% Acros Organics), Bright Brushing Gold (Alfa Æsar), ethanol (95% denatured MIBK Fisher), ethylene glycol (99+% Fisher ACS certified), perchloric acid (70% ACS reagent grade Acros Organics), concentrated phosphoric acid (85% ACS reagent grade Acros Organics), sodium sulfate (anhydrous ACS certified Fisher), potassium chloride (ACS certified Fisher), ammonium molybdate (VI) tetrahydrate (ACS certified Acros Organics), nickel nitrate hexahydrate (ACS certified Fisher), polymethyl methacrylate (PMMA) beads (Acros Organics), ferrocenemethanol (97% Acros Organics), DI water, hydrogen gas, nitrogen gas, and argon gas (HP grade Matheson Gas), sodium phosphate dihydrate monobasic (99+% Acros Organics), sodium phosphate anhydrous dibasic (ACS grade Acros Organics), Thermo Scientific Orion Application Solution pH buffers; pH 4.01 (#910104), pH 7.00 (#910107), and pH 10.01 (#910110).

Fabrication Catalyst Sample Array

Electrode Fabrication Method: A total of 64 gold electrodes for the rapid screening reactions were printed on 3” x 1” x 1mm glass microscope slides (Fisher Scientific). An acid bath of 10% perchloric acid was used to clean the surfaces of the slides overnight. Each electrode was printed with ink made from the bright brushing gold (Alfa Æsar) cut with tetrachloroethylene in a 5:4 ratio (BBG:TCE), yielding thin gold wires (~300 μm width) on the slides. The printing was performed by a Sonoplot GIX Microplotter Desktop printer, utilizing piezoelectric dispensing to pump the ink onto the

slide. To create the design for the printed features on the slide, Sonoplot SonoDraw software was used (Figure 2.1). Piezoelectric dispenser tips for the GIX Microplotter Desktop were borosilicate glass pipet tips pulled from capillary tubes (1.0 mm OD, 0.5 mm ID) using a Sutter Instruments P2000 pipet puller, resulting in a tip diameter roughly 60µm for printing the gold electrodes onto the glass slide substrate (Figure 2.2). Once the electrodes were printed, the ink was fired in a vented box furnace (Barnstead Thermolyne 48000) at 525°C for an 8 hour dwell following a $1\frac{^{\circ}C}{min}$ ramp rate to set the gold.

Catalyst Deposition Method: After the gold electrodes were fired on the glass slide, precursor solutions for the catalyst depositions were printed at the ends of the electrodes by the GIX Microplotter Desktop using a roughly 80-100µm diameter dispenser tip. Due to the method used to measure catalytic activity, catalyst deposition composition and reactive surface area were the important parameters in printing, not the overall volume of precursor printed, since this is a surface reaction and results can be normalized to electrode surface area. Optimized concentration combinations were used to keep the amount of printing at a minimum. This concentration optimization, accomplished by a C# based computer algorithm (Appendix B), allowed for the least number of drops necessary to achieve 2% increments of concentration while using only 4 precursor solution concentrations for each salt. By setting the number of precursor solutions desired and the incremental concentration change, the program would output the concentrations of each of the precursor solutions and the number of dots needed for each precursor at all electrodes. From this output, another program in LabView was created to input the data from concentration optimization program and convert it into the correct format and syntax for

the Sonoplot SonoGuide software to read. By writing these two programs, the efficiency of printing was drastically increased from the standard piezoelectric deposition method, which would require 50 deposition spots on each sample to achieve a 2% incremental concentration, resulting in an average of roughly 5 depositions on each electrode. The result is a reduction in time required to print the catalyst precursors by a full order of magnitude. Solutions of metal ion concentration used for both precursor solutions were 0.125, 0.100, 0.042, 0.008 M. For each of the depositions, since the metallic catalyst cannot be printed, a precursor solution had to be made for each metallic catalyst from metal salts dissolved in ethylene glycol. The precursor for metallic nickel was nickel nitrate hexahydrate, whereas ammonium molybdate (VI) tetrahydrate was used for the metallic molybdenum precursor. After the catalyst precursor spots were printed on the ends of the gold wires by the GIX Microplotter Desktop, the slide was fired in a tube furnace (Carbolite HST 12/300) under a 100ccm flow of hydrogen gas. The furnace was purged with nitrogen then heated to 150°C at a $3\frac{^{\circ}\mathrm{C}}{\mathrm{min}}$ ramp rate under nitrogen gas, at which point the feed was switched to hydrogen and the furnace was heated to 300°C at a $3\frac{^{\circ}\mathrm{C}}{\mathrm{min}}$ ramp rate and held at 300°C for 2 hours, much like the metal precursor method used by Fernandez et al.[43] After the baking was completed, the tube furnace was allowed to cool to ambient temperatures. This baking under hydrogen reduces the metal ions from the salts to their neutral charge state, leaving behind the bimetallic catalyst.

Electrode Wire Insulation: Following the catalyst spot printing, the exposed gold wires were insulated between the contact pad and the catalyst spot to isolate the current flow and reactive surface area solely to the catalyst spot surface. To accomplish this

insulating layer, poly(methyl methacrylate) (PMMA) was dissolved in tetrachloroethylene at a concentration of $0.125\frac{g}{L}$ and printed over the gold with the GIX Microplotter Desktop. Once printed, the polymer solution was dried at 120 °C for 1 hour (Quincy Lab Inc. Model 30GC Lab Oven) and the procedure was repeated for a second coat of polymer. Following the printing of the PMMA coating, the size of the catalyst dots is in the range of microelectrodes (80-100 μm). This allows for the steady state reaction current to be measured, providing data to calculate the exact surface area of the printed electrode using the following equation for flat disk-type electrodes[44]

$$i_{ss} = 4nFDc^{*}r \qquad \text{(Eq. 2.7)}$$

where $i_{ss}$is the steady state current, n is the number of electrons required in the reaction mechanism, F is Faraday's constant, D is the diffusion coefficient of the species being reacted within the electrolyte, c* ist the electrolyte concentration, and r is the radius of the electrode surface assuming it is circular. By making this calculation to find the area of the electrode, the data can be normalized to electrode area and proper simulations can be run with realistic initial input values to determine the kinetic parameters k^{0}_{eff} and α. Other rapid screening methods are more sensitive to details, such as exact deposition size (reactive surface area), and are limited in their scope and ease of operation.

The PMMA printing was the least reliable part of the print procedure, due to the low viscosity of the tetrachloroethylene solvent occasionally causing coverage to extend farther than desired. The overall yeild of operational electrodes was roughly 95%.

Reaction Cell Fabrication

A reaction cell (Figure 2.3) was custom fabricated to utilize the rapid scanning capabilities of the printed catalyst array on the slide. This cell was constructed of a PTFE core, in which the printed slide was secured and gold lugs contacted the pads on the slide, an acrylic base to hold the slide in place, and an aluminum top plate tapped and threaded to act as an anchor to hold the cell together with four screws. The slide fits into a milled out pocket in the PTFE with a Viton O-ring sealing around the cell perimeter. This allows for the reaction cell to be filled with electrolytic solution for the reaction, sealing off the uncoated gold from the solution and keeping all reactive current passing through the catalyst spots.

Each electrode contacted its respective gold lug in the reaction cell, which in turn were wired to an Analog Devices ADG732 32-channel analog multiplexer chip controlled by a National Instruments USB-6009 control box. This allowed for a Labview program to be utilized, by which each electrode was activated individually, and a linear sweep voltammagram (LSV) was taken to measure the electrocatalytic properties of the bi-metallic catalyst. The LSVs were performed with a CH Instruments CHI660E potentiostat using a platinum wire counter electrode and a CH 111 Ag/AgCl reference electrode standardized with a 0.5mM ferrocenemethanol redox reaction.

Reaction Conditions and Methods

Data was taken in aqueous electrolyte solutions of two different pH buffers at pH values of 2.2 and 6.7. The electrolytes used for each of the pH values are as follows: For the pH 2 phosphate buffer electrolyte, 0.10 M total concentration (0.04145M sodium

phosphate monobasic (NaH_2PO_4): 0.05855M phosphoric acid (H_3PO_4)), giving 0.01M H^+ concentration; for the pH 7 electrolyte, a 0.10 M total concentration phosphate buffer solution of 0.0422M sodium phosphate monobasic (NaH_2PO_4) and 0.0578M sodium phosphate dibasic (Na_2HPO_4), yielding 1E-7M H^+ concentration. These different pH values allowed for the catalytic properties of NiMo to be measured at a wider range of H^+ concentrations while having the pH remain stable in buffered solutions. Calculations for these concentrations were made using the sodium phosphate pK_a values with the Henderson-Hasselbalch equation. Completed pH buffer solutions were measured with a Fisher Scientific accument AB150 pH meter calibrated with Thermo Scientific Orion Application pH buffer solutions (pH 4.01, 7.00, 10.01), resulting in an the acidic buffer with a pH 2.2 and the neutral buffer with a pH 6.7, maintaining 0.10 M total electrolyte concentration. Previous bulk catalytic testing in NiMo HER research has focused mainly on relatively neutral pH solution, since it is most realistic for water splitting applications, but also because rapid analysis in acidic conditions has provided challenges for experimental setup due to the catalyst stabilities over prolonged exposure[31] and analytic method restrictions. Therefore, completing a bulk screening method on this catalyst system in 2% incremental steps with both neutral and acidic conditions provides new insight into the catalyst with a method fast enough to analyze relatively time critical reactions.

To set up each array of reactions, 30 mL of the pH buffer electrolyte solution was bubbled with argon gas for 10 minutes to displace all non-inert gases in solution. Once the slide was secured in the reaction cell, the top of the cell was covered with parafilm pierced with 3 small holes for the counter electrode, reference electrode, and argon purge needle. The argon purge needle was set in the headspace of the cell for 10 minutes to purge the cell

of non-inert gases, then the argon-purged electrolyte was pipetted into the reaction cell and the counter and reference electrodes were put in place.

The HER reaction was carried out by means of linear sweep voltammetry, an electrochemical analytical method of potential sweep, starting at 0.00 volts vs. Ag/AgCl reference and sweeping to -1.20 volts vs. Ag/AgCl. This sweep in potential allows for the reaction to begin once the reaction potential is reached, at which point the reaction speeds up in accordance with the kinetics of the system as the overpotential increases until the mass transfer mechanism finally begins to limit the reaction rate. From the current vs. potential data collected with LSV, the desired kinetic parameter values, k^0_{eff} and α, can be extracted via curve fitting COMSOL Multiphysics simulations.

RESULTS AND DISCUSSION

Catalyst composition and structural characterization

SEM/EDS: The catalyst spots were analyzed using an FEI Versa 3D Dual Beam scanning electron microscope. The gold wires and catalyst spot surfaces were inspected to ensure relatively consistent surface features (Figure 2.4). In addition, the SEM was also used to perform EDS elemental analysis of the metals present in the different catalyst spots. This allowed for the distribution of metals within the catalyst spots to be verified as relatively uniform (only minor metal composition variance within the spots) and in the proportions desired (Figure 2.5). EDS analysis confirmed that the piezoelectric printing-based deposition technique employed was accurate and reliable when using precursor salts dissolved in ethylene glycol.

Catalytic Electrochemical Testing

LSV Data Analysis and Simulation: After obtaining the linear sweep voltammograms for each of the catalyst compositions, the data was initially analyzed using National Instruments DIAdem to determine initial values for the catalyst spot radii as well as converting the LSV data to an appropriate format for input to COMSOL Multiphysiscs software. Once the LSVs were prepared by DIAdem, the next step was analysis with simulation software to extract the desired kinetic parameters, k^0_{eff} and α. An example of this is shown in Figure 2.6 where the effective pH 2.2 trends in results are compared. To accomplish this, COMSOL Multiphysics software was used to simulate the physical reaction geometry of the catalyst coated electrode surface and the reactive species within the electrolyte solution, also accounting for the potential difference between the catalyst spot and the platinum counter electrode. Then the LSVs acquired by the rapid screening method were fed into COMSOL and the known physical parameters of the reaction were input. A proprietary Java program within COMSOL was written to perform automated progression through simulations on different data sets in order to optimize ease and efficiency of simulations, effectively starting a new simulation as soon as the last one finished. The optimization software module was used to fit a simulated LSV plot to the raw data. By constraining the variables to be only k^0_{eff}, α and electrode area the COMSOL optimization module was used to solve for these kinetic parameters. The numerical solution method employed for these simulations was SNOPT, using the Butler-Volmer equation (Eq. 2.8)[44] to solve for k^0_{eff}, α and the exact radius of the electrode:

$$i = FAk^0\left[C_O(0,t)e^{-\alpha f(E-E^0)} - C_R(0,t)e^{(1-\alpha)f(E-E^0)}\right] \qquad \text{(Eq. 2.8)}$$

where i is the reaction current, F is Faraday's Constant, A is the electrode area, C_O and C_R are the oxidized and reduced species concentrations, respectively, t is a given time, $E-E^0$ is the reaction overpotential, f is the equivalent of $\frac{F}{RT}$ and k^0_{eff} and α are the kinetic parameters rate constant and transfer coefficient, respectively.

It was noticed that the value of α was settling closely around 0.3, so the program was modified to fix α to this value, leaving k^0_{eff} and A as the only variables, speeding up the time required for each simulation while still providing exceptional curve fitting. This method allows for the kinetic parameters, a quantitative measurement of catalytic abilities, of the catalyst to be found. Compared to previous efficient rapid screening methods, which to this point have yielded qualitative results, this offers quantitative results that can be compared across data sets, allowing for a database of kinetic data to be developed with more ease and accuracy.

The advantages to using linear sweep voltammetry include ease of procedure, capable of being run without precise alignment of the electrodes within electrolyte solution, and most importantly, the ability to extract kinetic parameters from the profile of the curve. The disadvantages with using linear sweep voltammetry occur when attempting to study more than one sample on the same substrate. When attempting to study catalyst arrays on FTO or other conductive substrates, the counter electrode must be capable of moving to focus on each individual sample, reducing cross talk reactions with the other samples in the array. This method also requires the use of an SECM to accomplish screening. Most other rapid methods, such as the bipolar electrochemistry method used by

Fosdick et al.[16] or the gold shielded SECM electrode used by Minguzzi et al.,[37] still create some cross-sample interference that must be accounted for and correctly simulated, as they did with COMSOL. This new LSV-based method being reported completely eliminates all of these interferences and cross talk issues by effectively isolating each individual sample in the array as an individual electrode, rather than having an array of samples on one single electrode surface. Because of this feature, there is no need to simulate the background interference of the surrounding samples in order to determine the true signal produced by the desired sample in the array, which in turn decreases the number of steps needed to analyze the data, speeding up the process even further.

As shown in Figure 2.6, the curve fitting from the COMSOL simulations directly relates to the LSV data, matching the data rather well in the kinetic regions, with minor deviations in the mass transfer controlled region for some of the samples. When comparing the results, any changes in α would affect the curvature of the inflection points, which seem to fit relatively well across the samples; and any change in k^0_{eff} would affect the slope of the near-linear region of the plots, with a larger k^0_{eff} resulting in a steeper climb in current. The simulation results for k^0_{eff} match the progression of slopes between the samples in Figure 2.6, giving a favorable measure of accuracy to the simulations.

Experimental Results

Acidic: The pH 2.2 phosphate buffer solution show peaks in catalytic activities at multiple composition regions, with the best properties occurring at 78-90% Ni and 10-22% Mo, with the former region as the most active region as shown in Table 2.1. This trend in the results is in agreement with previous literature published on the NiMo bimetallic

system for aqueous hydrogen evolution at acidic conditions.[33] The expected result was Ni providing a better catalytic response than Mo, but the combination of the two outperforms each individual metal. The LSV data and corresponding simulations for the pH 2.2 catalytic activity table are shown in Figure 2.7 a-f.

Neutral pH: For the pH 6.7 phosphate buffer solution, the results differed from the pH 2 results. Peaks in catalytic activity were clearly visible, but occur at different concentrations within the gradient (Table 2.2). Once again, Ni was a better pure metal catalyst than Mo, but there were combinations of the two metals that outperformed both of the individual metals, mainly occurring in two regions of increased activity around 12-18% and 46-62% Ni. These trends in the results agree with findings by Fosdick et al.[16] The LSV data and corresponding simulations for the pH 6.7 catalytic activity table are shown in figure 2.8 a-f.

CONCLUSION

Bimetallic NiMo HER catalyst composition arrays were studied using a new linear sweep voltammetry-based rapid screening method for finding catalytic reaction rate parameters. The goal was to validate this new method of high throughput electrocatalyst screening which is more ease and efficiency than previous methods while returning quantitative data with, something that has been more difficult to accomplish previously, especially when needing to account for crosstalk and noise between samples. This combinatorial screening method employs a piezoelectric printing method to create catalyst arrays which can be studied individually without any interference from the other samples.

In addition, automated reaction simulations with COMSOL Multiphysics were utilized to perform curve fitting on the experimental data, effectively determining the kinetic parameters for each linear sweep votammogram. The results from this method agree with the other research that has been done on the NiMo system, with peaks in catalytic activity at 78-90% for acidic pH and 46-62%, 12-18% for neutral pH, validating the feasibility of this method for rapid data acquisition. The flexibility of the piezodipensed catalyst deposition method used opens up the possibilities for virtually any multimetallic combinations to be analyzed.

CHAPTER 2 FIGURES

a)

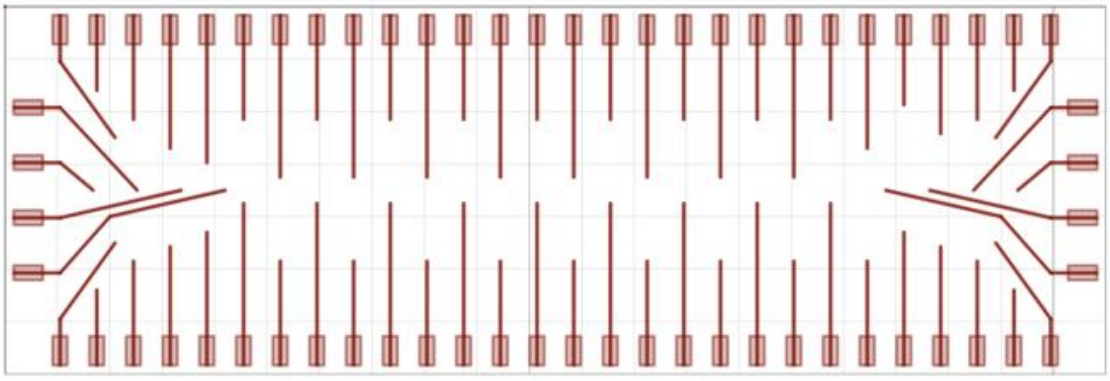

b)

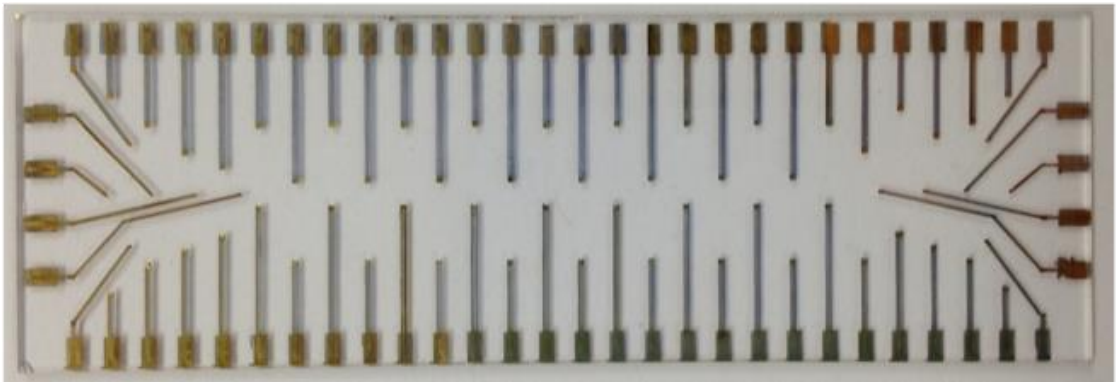

Fig 2.1: (a) The SonoDraw design software schematic of the gold wire print for the Sonoplot GIX Microplotter Desktop, and (b) the printed gold wires on the glass slide substrate after firing but prior to the catalyst spot printing.

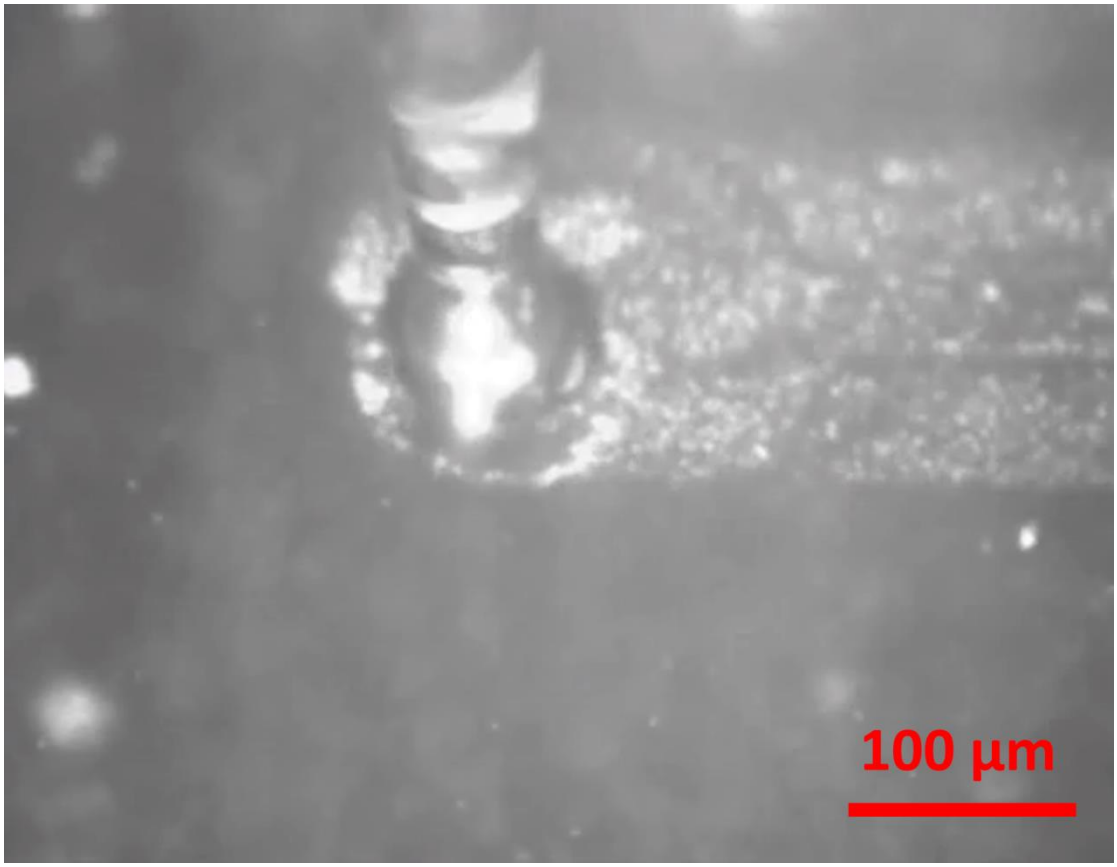

Fig 2.2: A 60 µm laser pulled glass pipet tip on the piezoelectric dispenser head of the Sonoplot GIX Microplotter Desktop. This tip is in the process of depositing the metal precursor solutions on the ends of the printed gold wires.

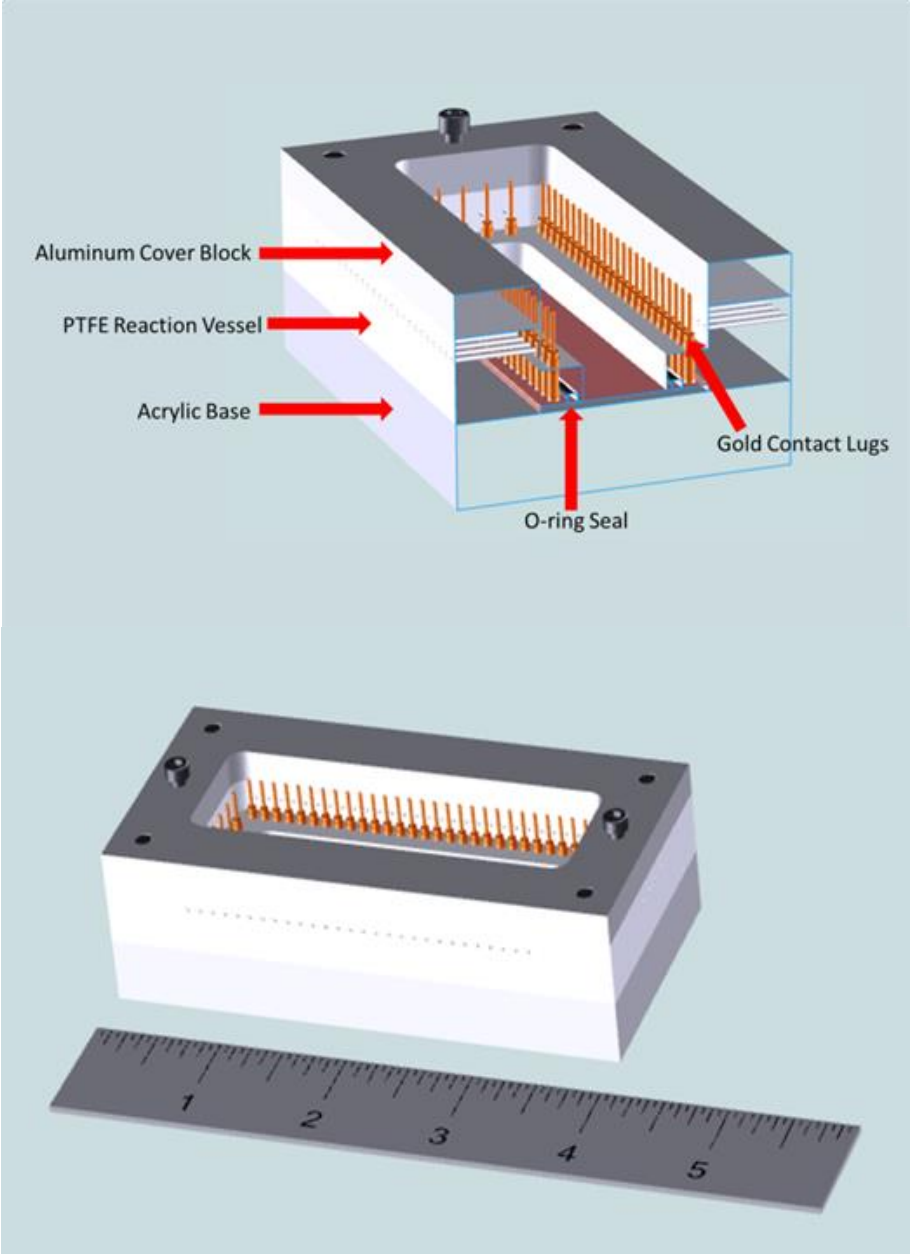

Fig 2.3: CAD schematic of the reaction cell used for the rapid screening tests. The layers of the cell are held together by screws that are captured in the acrylic base and thread into the aluminum cover block. Each gold contact lug is wired through holes in the Teflon body to 2 32-channel multiplexers controlled by a National Instruments USB control box. The O-ring seal allows the electrolytic solution to be isolated from the contact lugs and uninsulated parts of the gold wires.

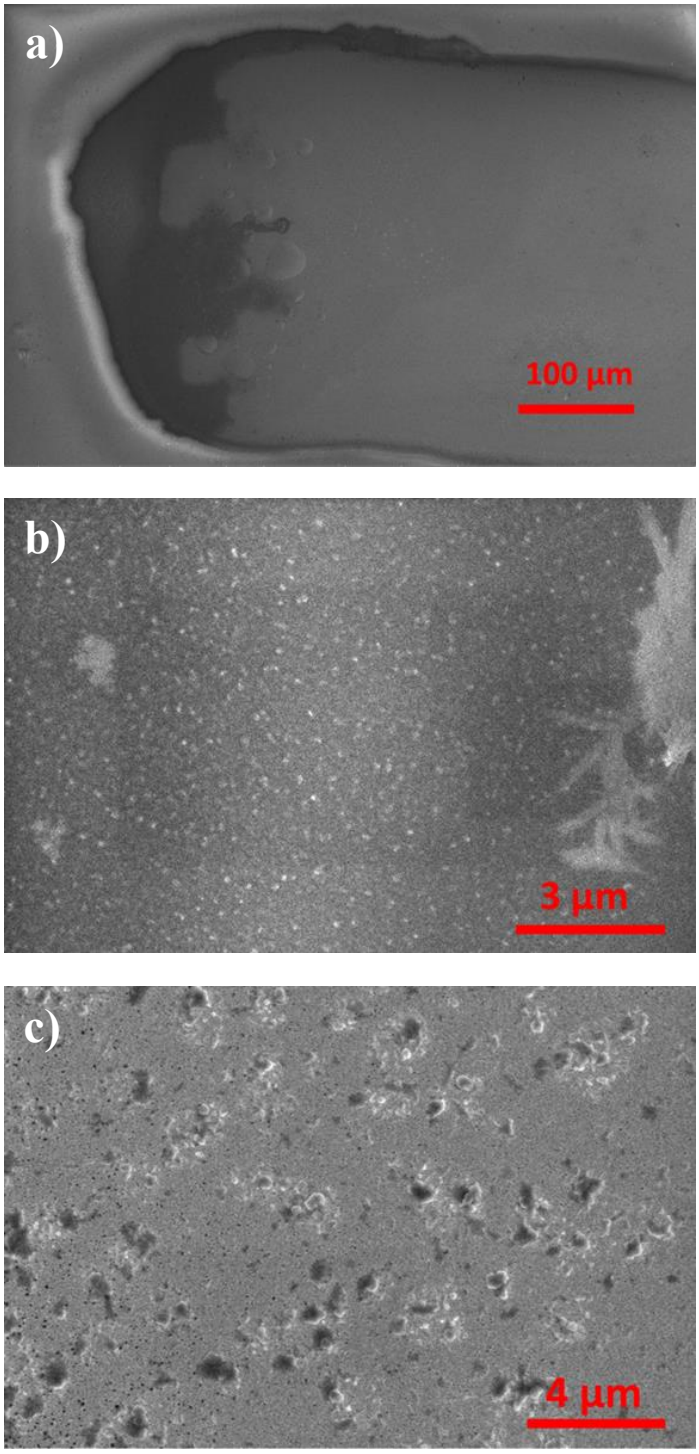

Fig 2.4: (a) SEM image of the end of a gold wire with catalyst coating (20% Ni : 80% Mo). Sites of catalyst concentration can be seen, but the coating is a uniform film aside from these spots, with the coated region having a slight darker shading. The light colored region on the edge of the wire is due to the catalyst film layer terminating just off of the edge of the gold wire. (b) A closer look at the catalyst film surface as opposed to the bare gold electrode wire surface seen in (c).

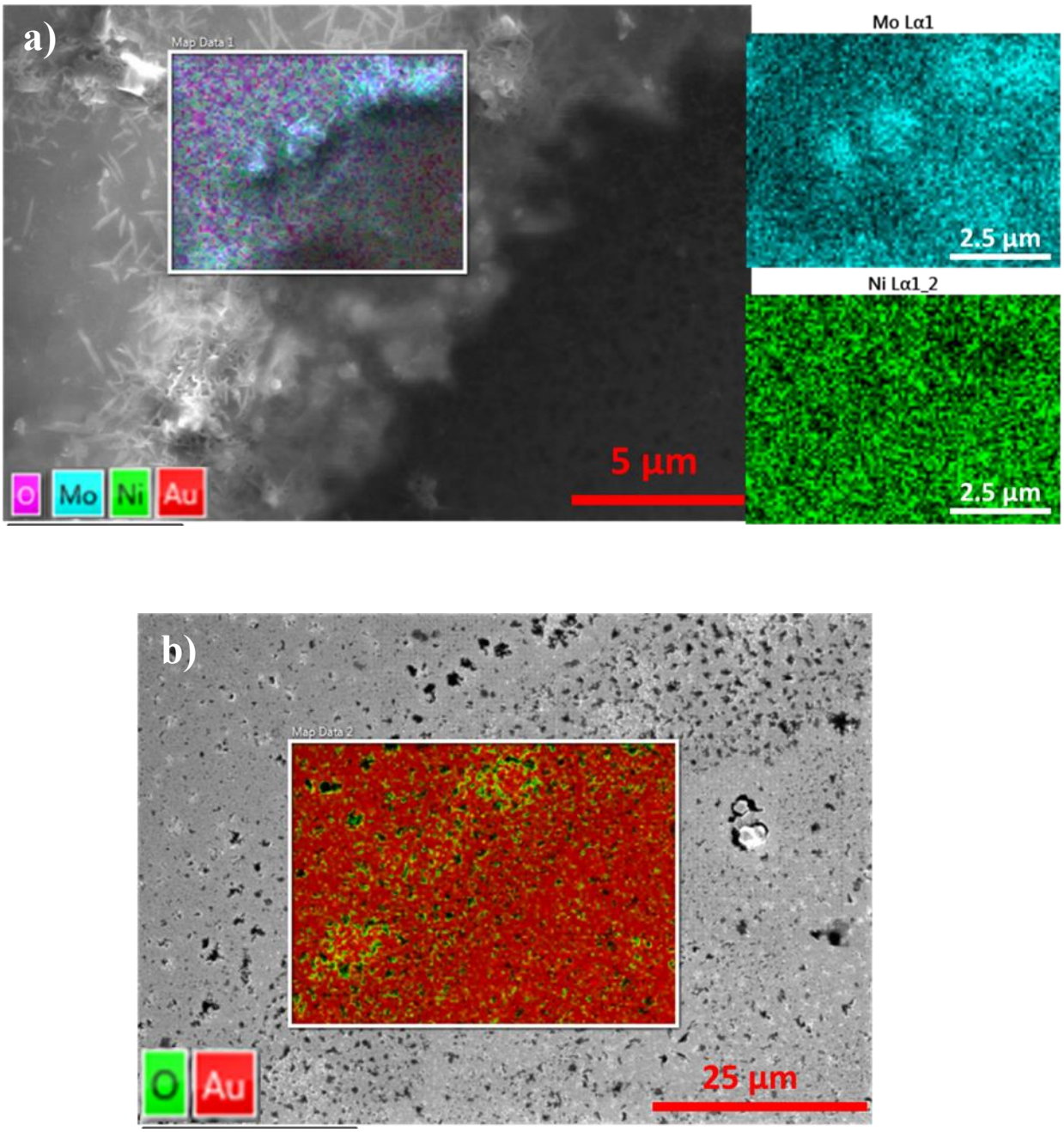

Fig 2.5: SEM and EDS imaging of NiMo catalyst spot showing some minor segregation of the catalyst metals at points, namely clumping of the molybdenum within the EDS region, but overall confirming the successful 80% Ni to 20% Mo deposition that was desired.

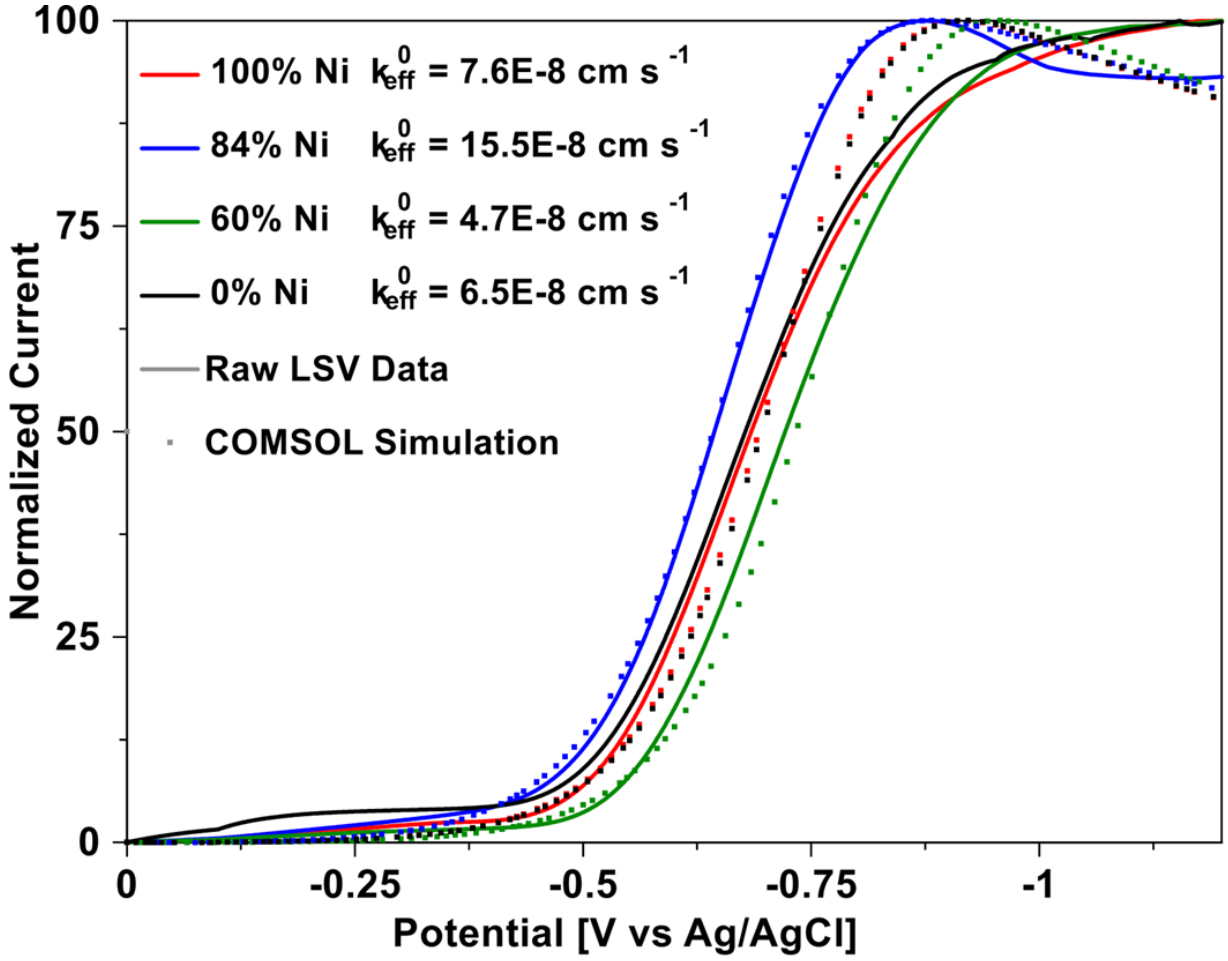

Fig 2.6: Linear sweep voltammagrams (normalized to reaction peak current) and corresponding COMSOL simulation curves for a range of bimetallic NiMo HER catalyst compositions at pH 2.2. As can be seen in both the slopes of the kinetically controlled reaction region of the plot and the k^0_{eff} values, an optimum composition of NiMo (84% Ni) gives markedly better performance than either pure Ni or pure Mo, whereas a non-optimal composition (60% Ni) gives markedly worse performance than the pure metal components.

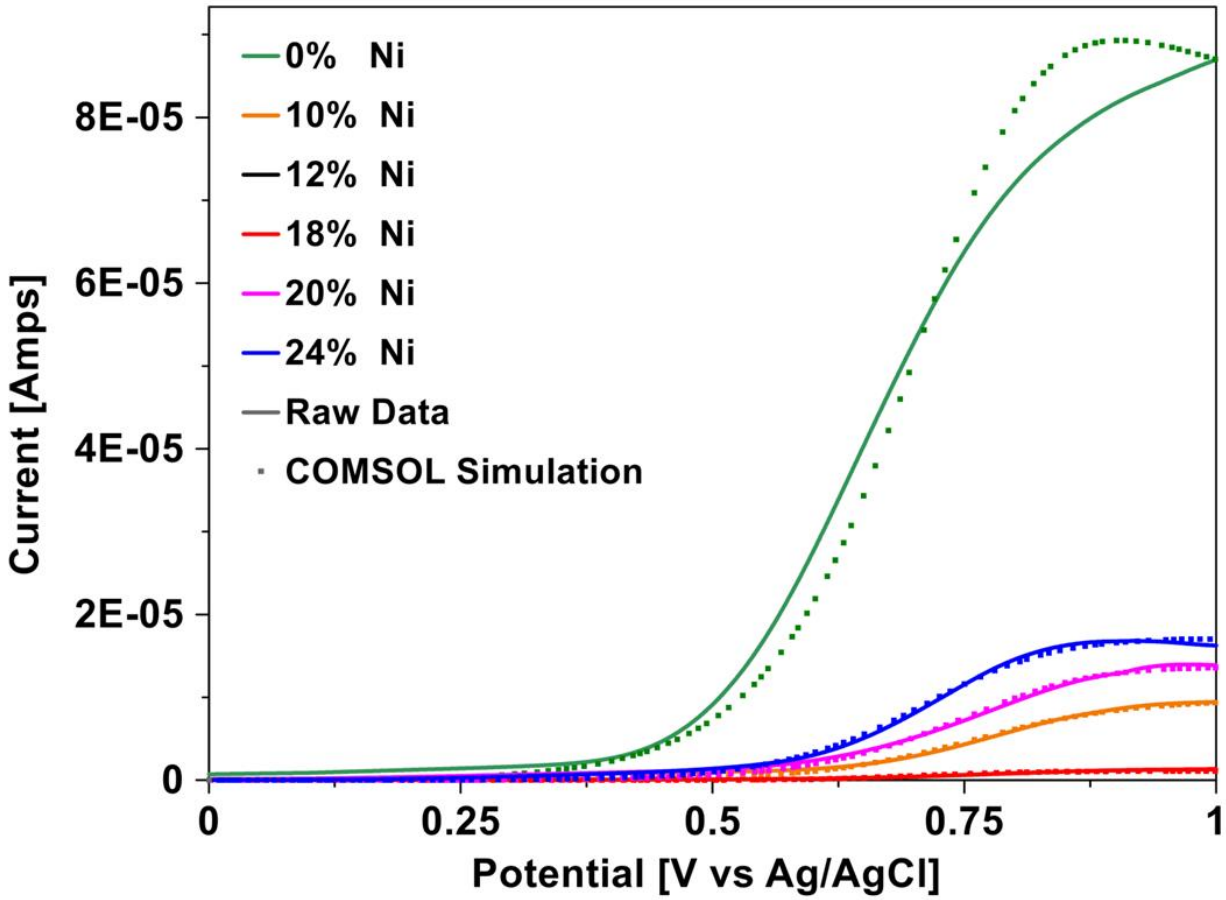

Fig 2.7 a: Raw data and corresponding simulation results for NiMo bimetallic catalyst in acidic (pH 2.2) electrolyte.

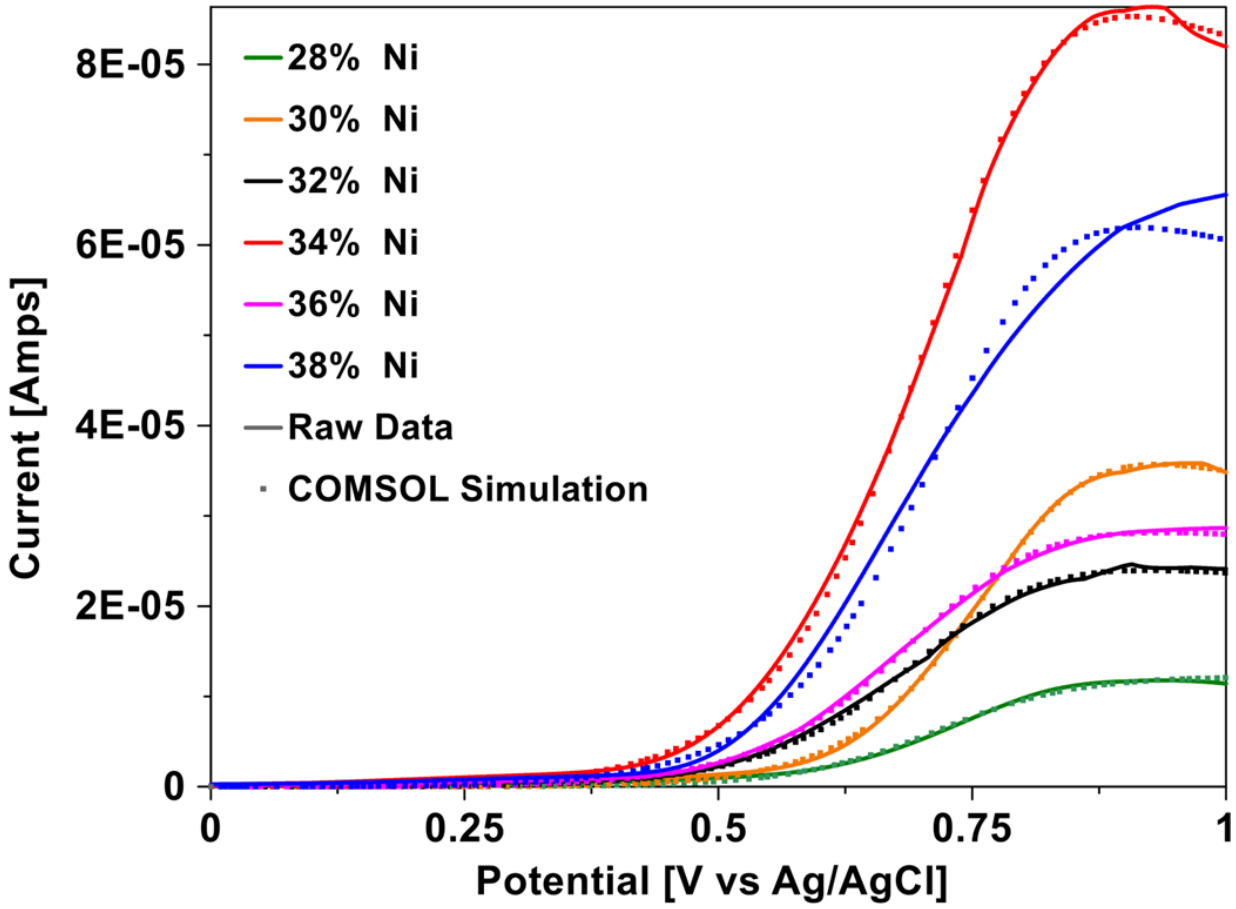

Fig 2.7 b: Raw data and corresponding simulation results for NiMo bimetallic catalyst in acidic (pH 2.2) electrolyte.

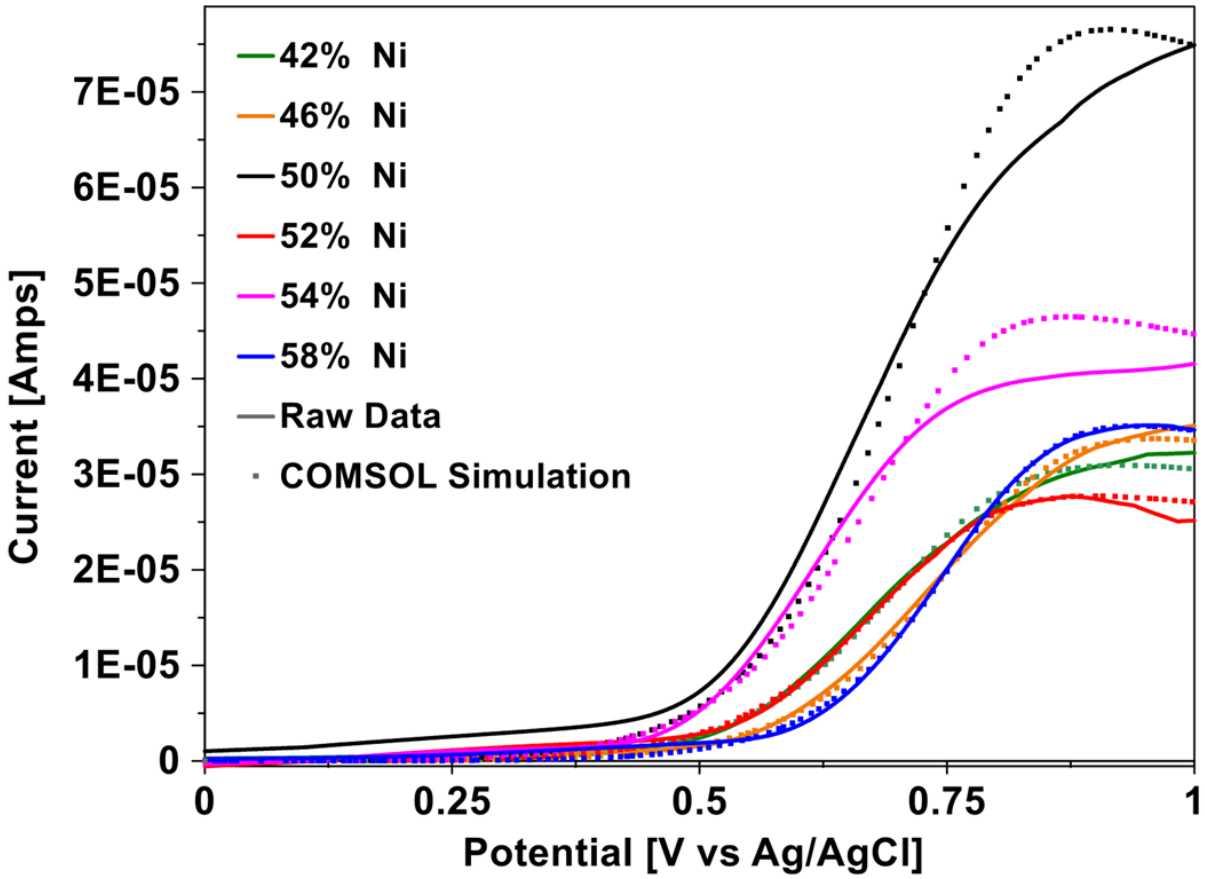

Fig 2.7 c: Raw data and corresponding simulation results for NiMo bimetallic catalyst in acidic (pH 2.2) electrolyte.

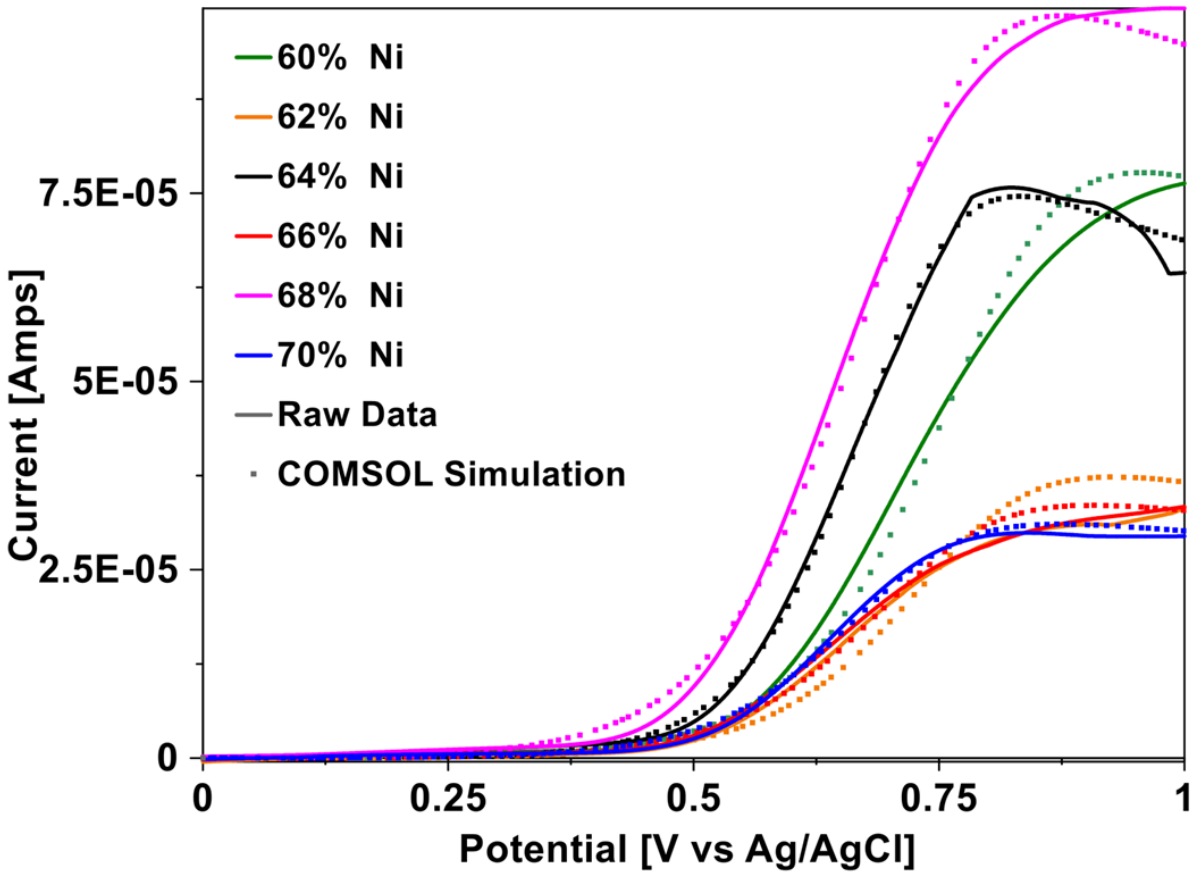

Fig 2.7 d: Raw data and corresponding simulation results for NiMo bimetallic catalyst in acidic (pH 2.2) electrolyte.

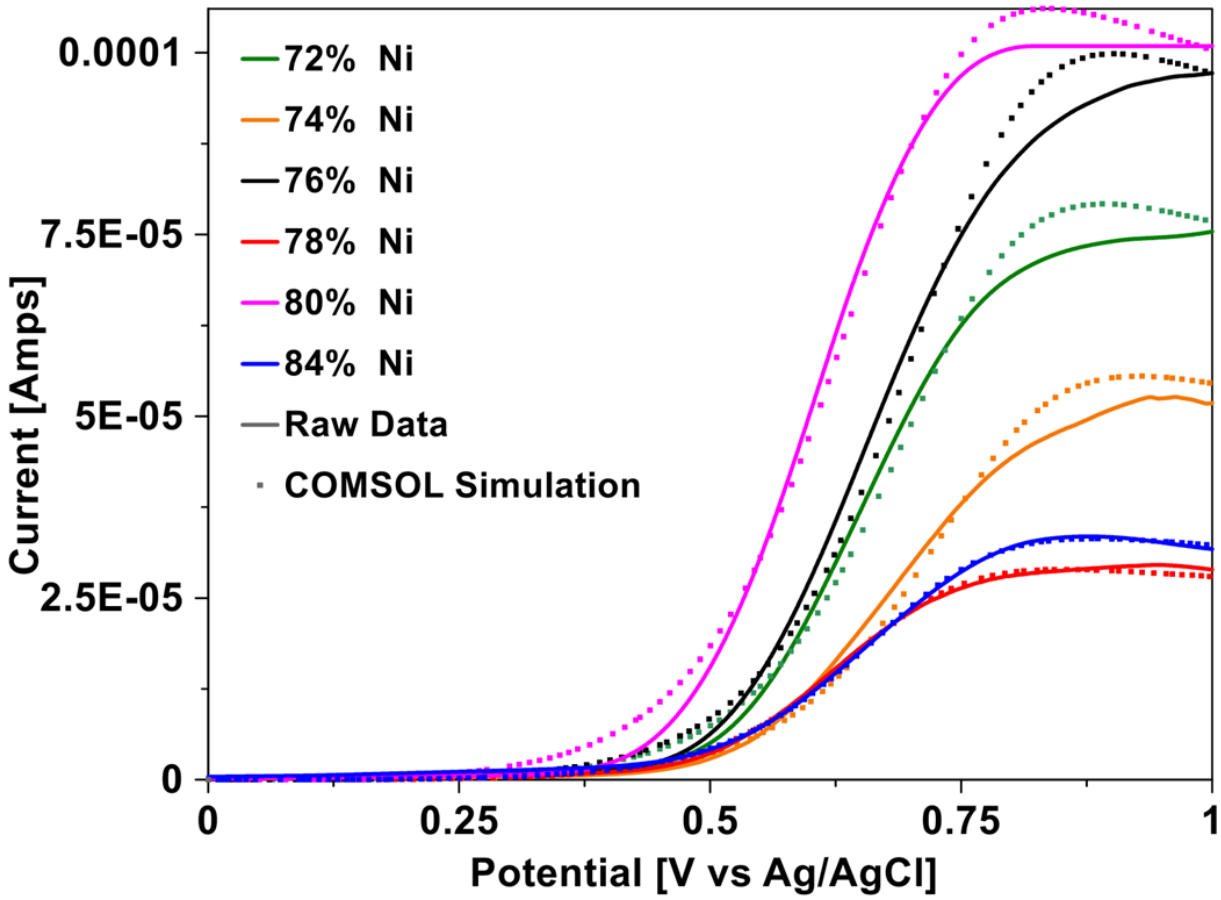

Fig 2.7 e: Raw data and corresponding simulation results for NiMo bimetallic catalyst in acidic (pH 2.2) electrolyte.

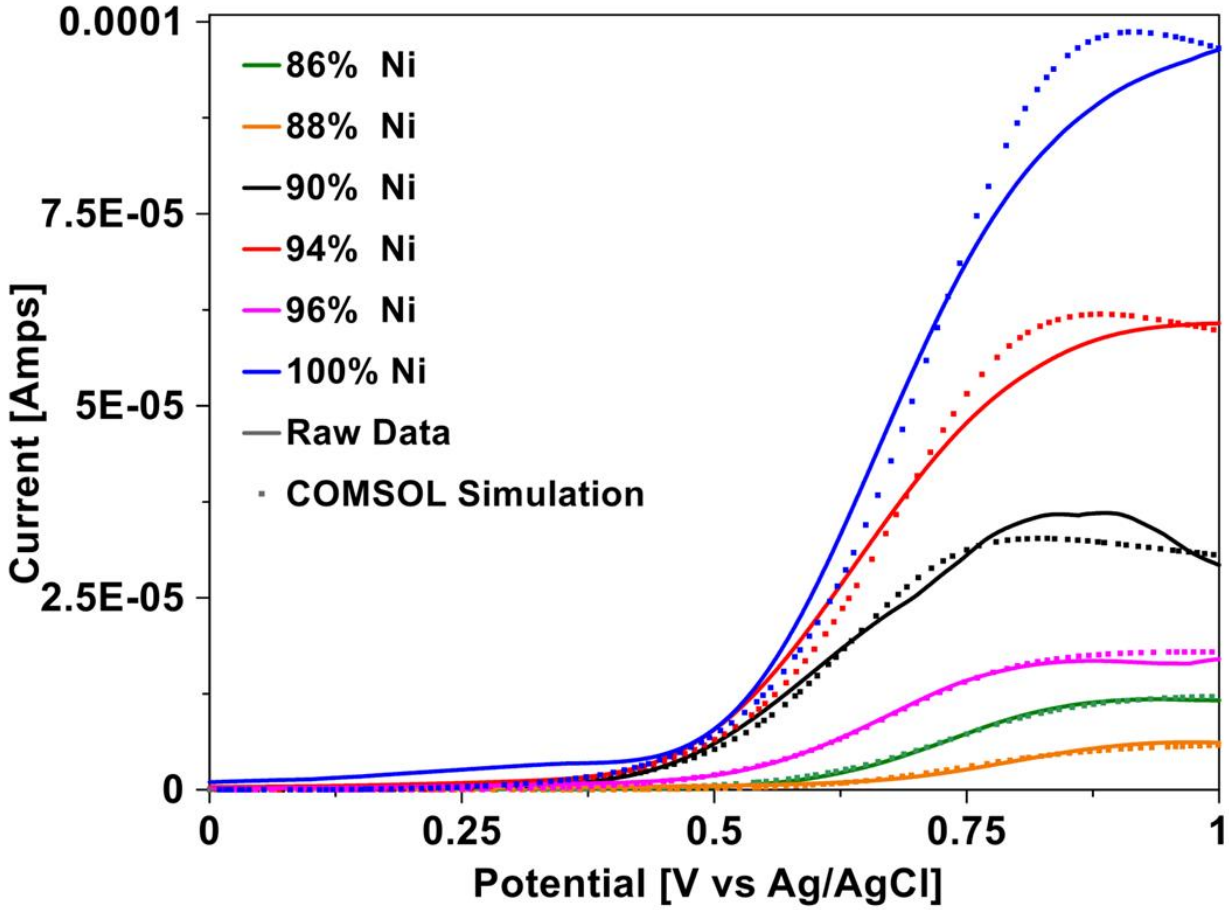

Fig 2.7 f: Raw data and corresponding simulation results for NiMo bimetallic catalyst in acidic (pH 2.2) electrolyte.

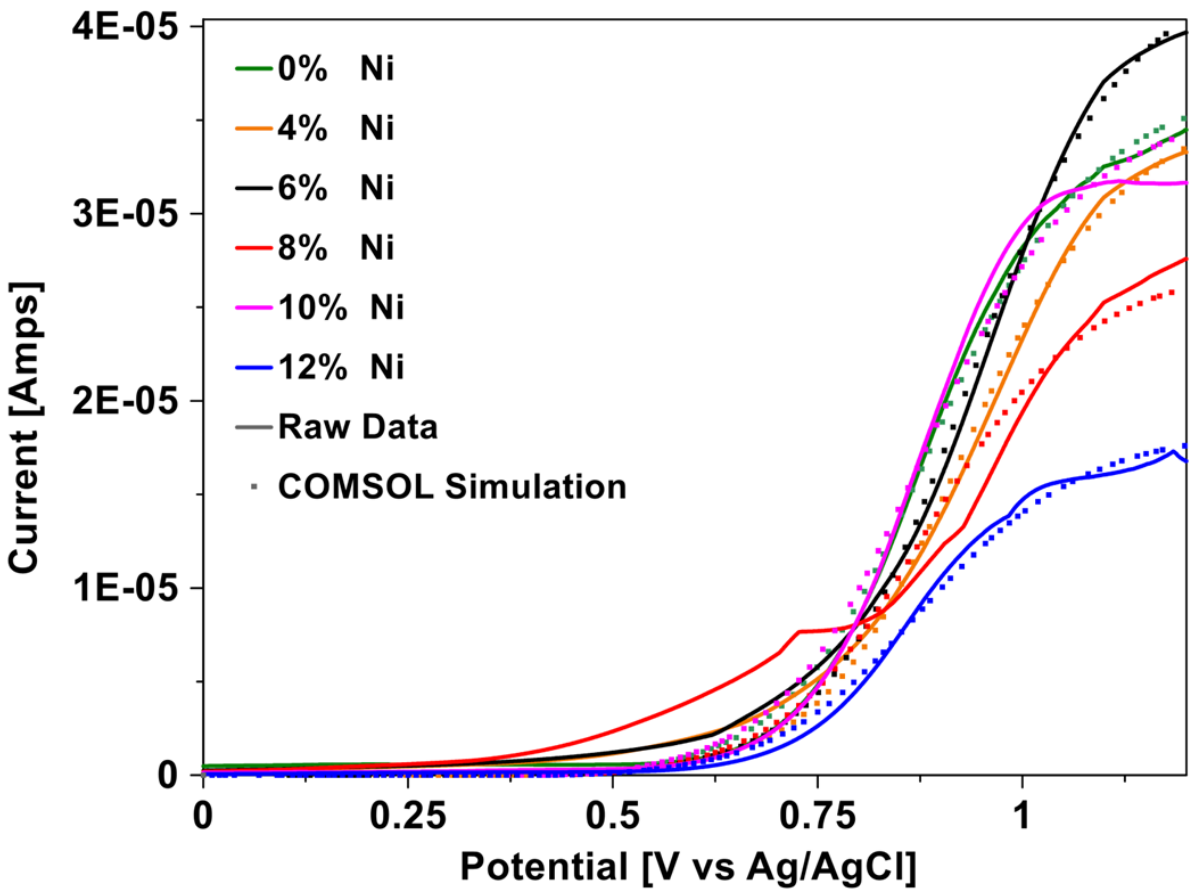

Fig 2.8 a: Raw data and corresponding simulation results for NiMo bimetallic catalyst in neutral (pH 6.7) electrolyte.

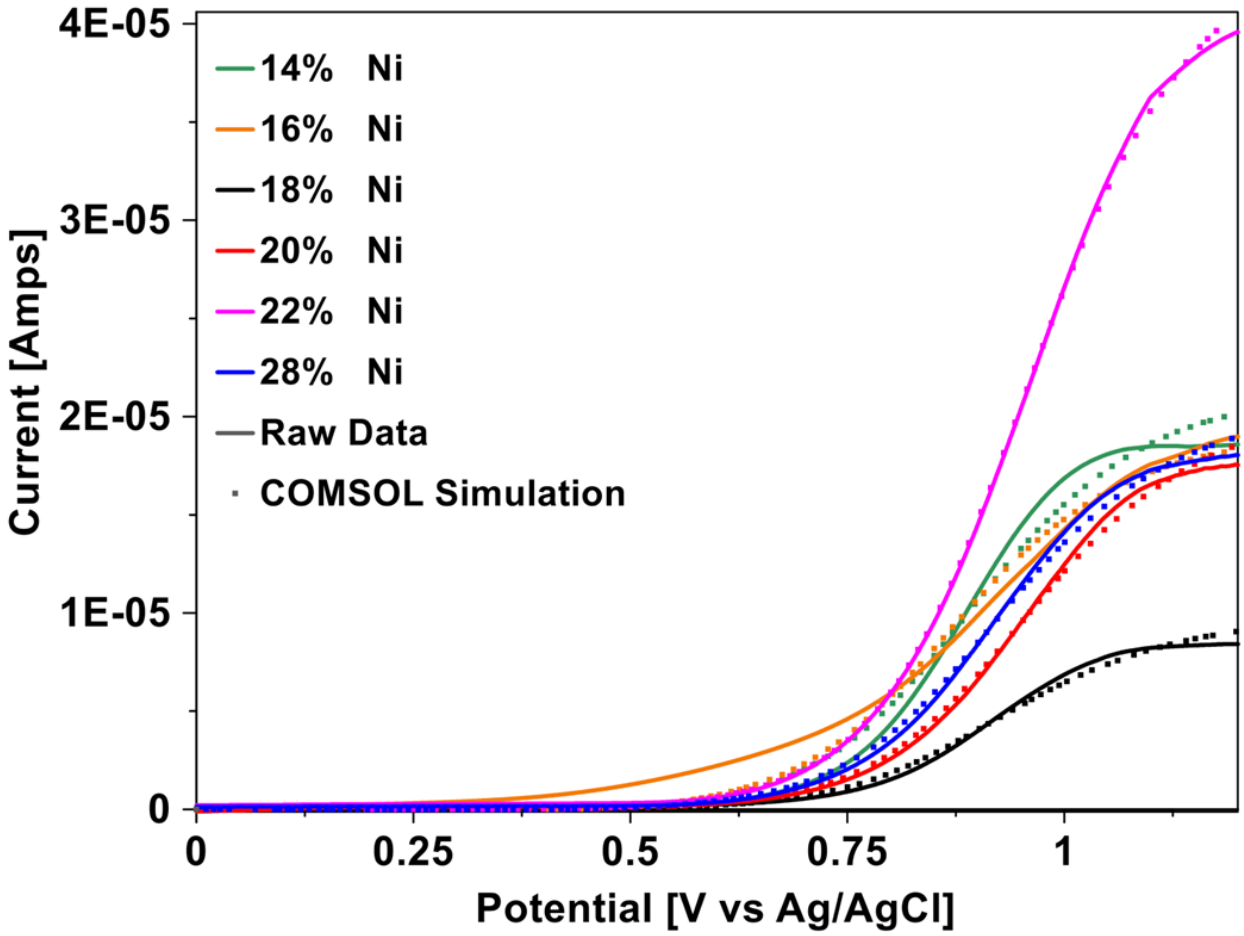

Fig 2.8 b: Raw data and corresponding simulation results for NiMo bimetallic catalyst in neutral (pH 6.7) electrolyte.

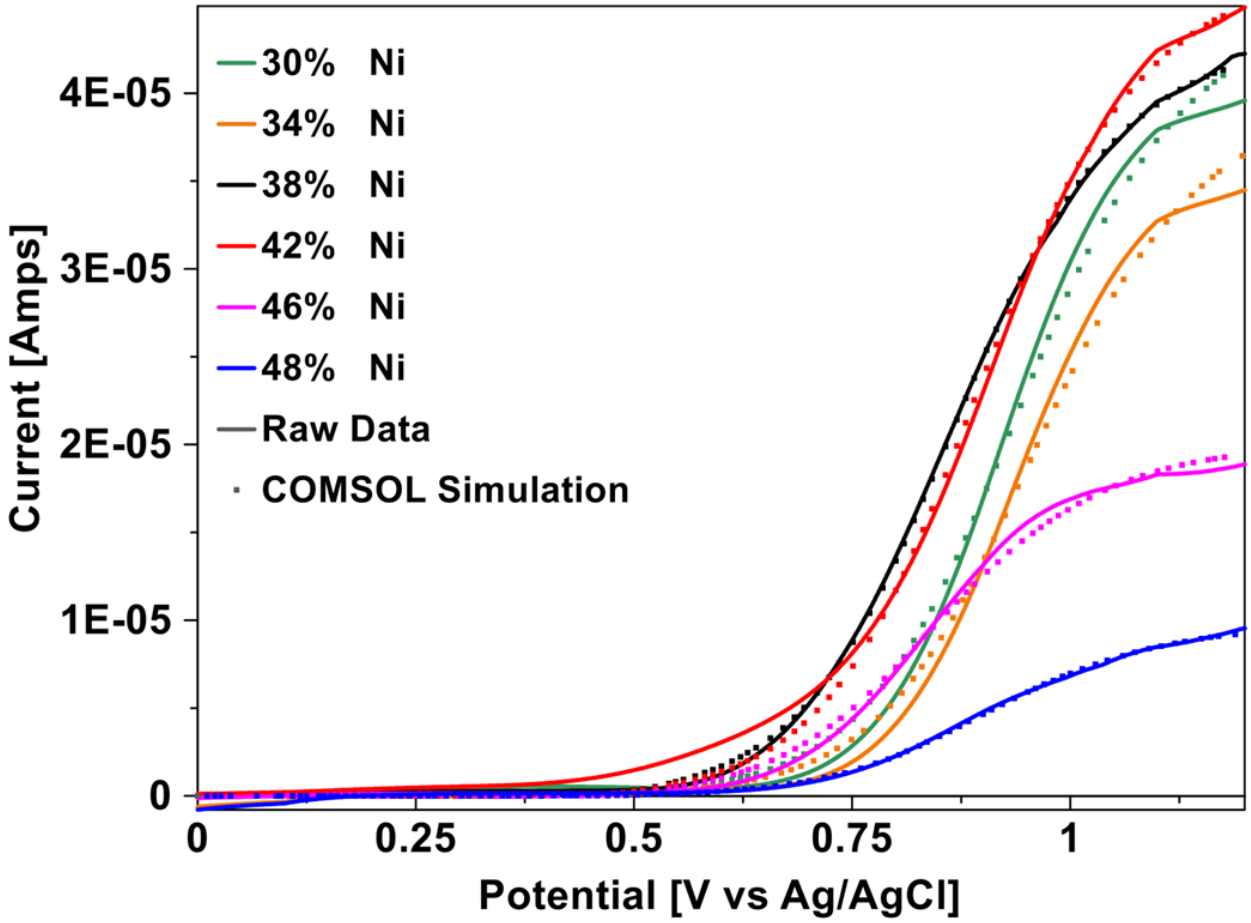

Fig 2.8 c: Raw data and corresponding simulation results for NiMo bimetallic catalyst in neutral (pH 6.7) electrolyte.

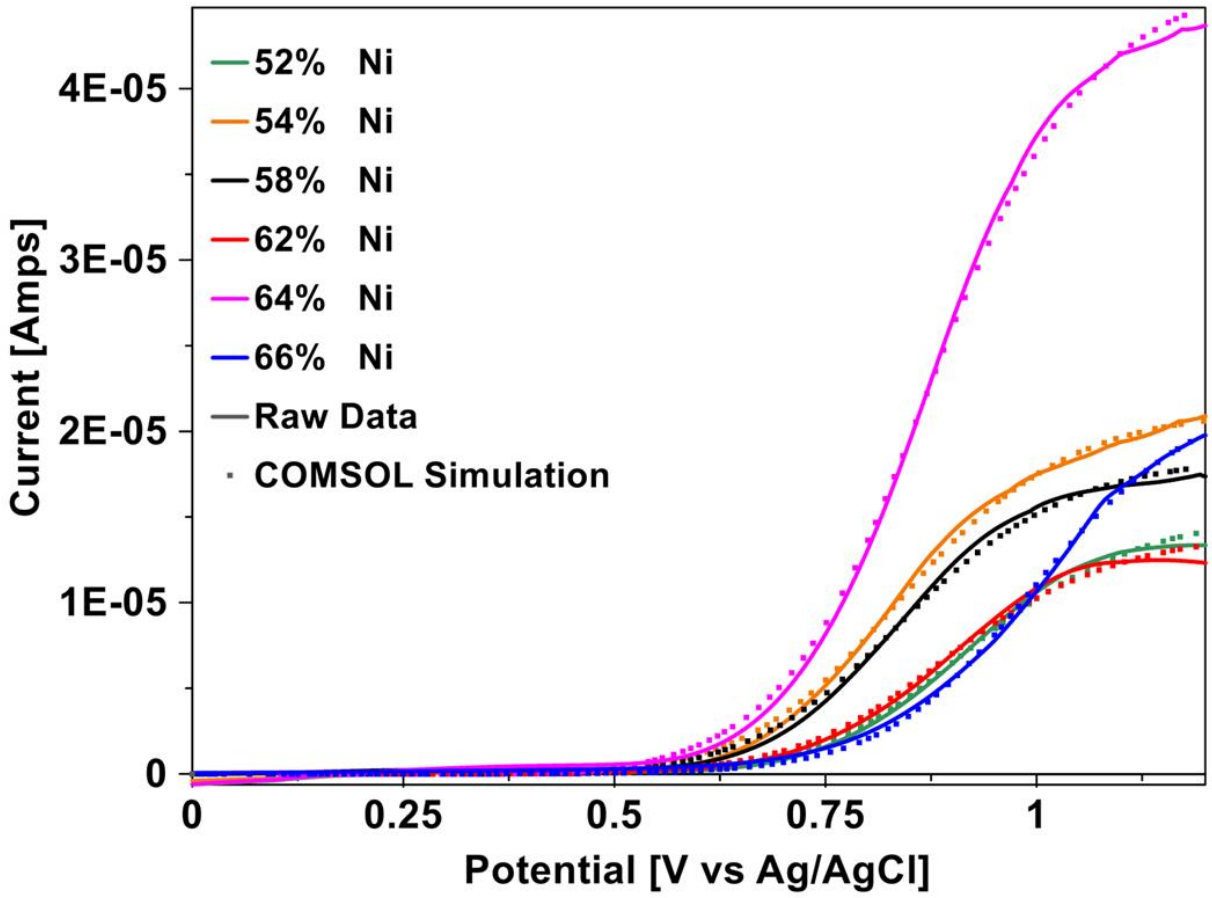

Fig 2.8 d: Raw data and corresponding simulation results for NiMo bimetallic catalyst in neutral (pH 6.7) electrolyte.

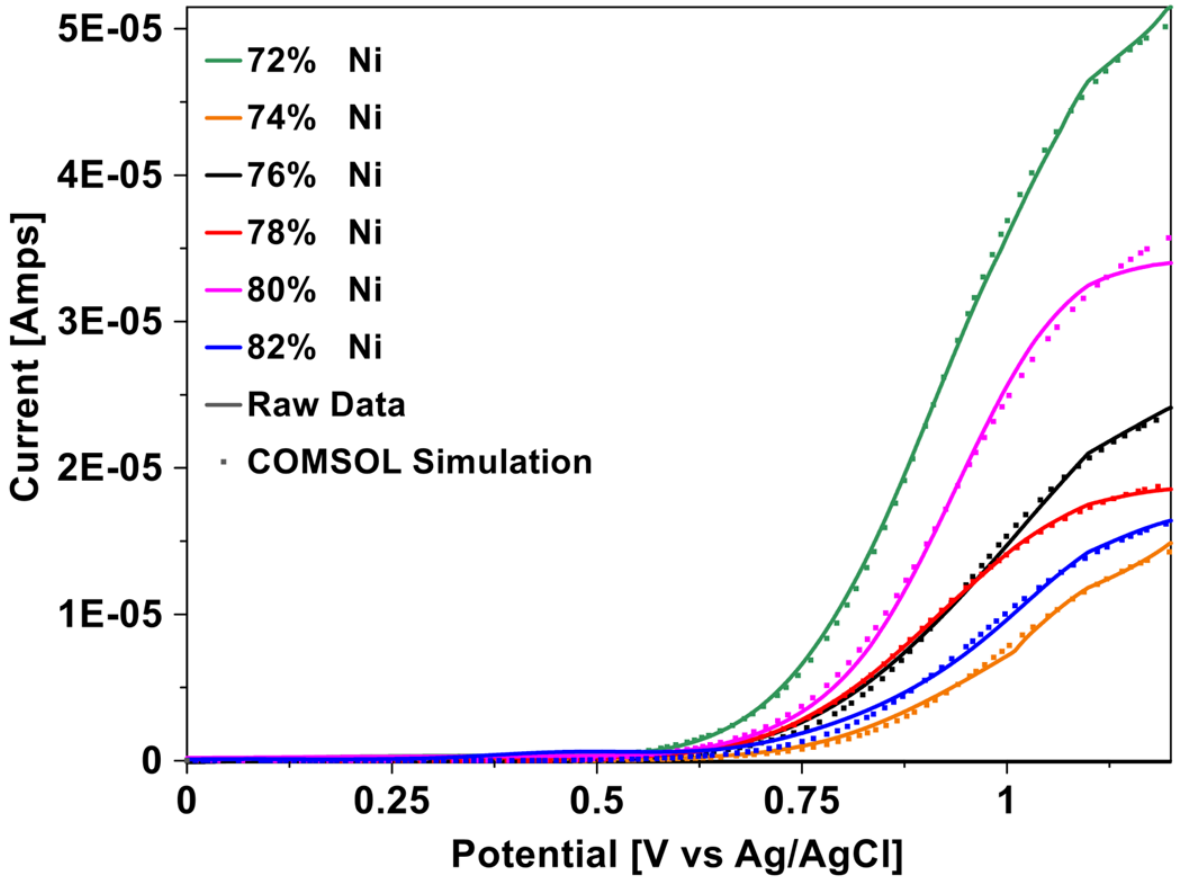

Fig 2.8 e: Raw data and corresponding simulation results for NiMo bimetallic catalyst in neutral (pH 6.7) electrolyte.

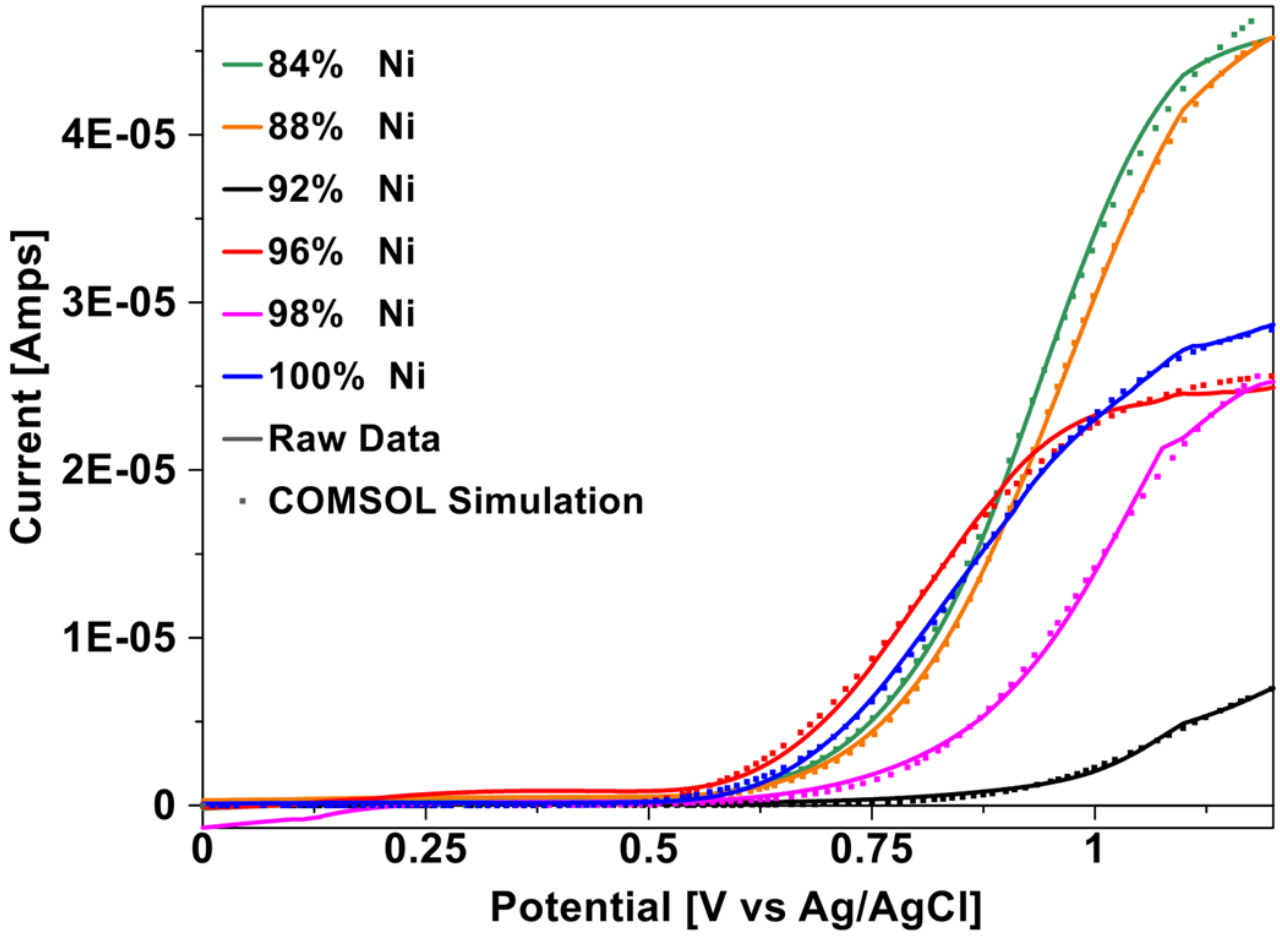

Fig 2.8 f: Raw data and corresponding simulation results for NiMo bimetallic catalyst in neutral (pH 6.7) electrolyte.

CHAPTER 2 TABLES

Ni%: 0 k^0_{eff}: 8.9	Ni%: 10 k^0_{eff}: 12.9	Ni%: 12 k^0_{eff}: 6.5	Ni%: 18 k^0_{eff}:14.8	Ni%: 20 k^0_{eff}:10.2	Ni%: 24 k^0_{eff}:12.9
Ni%: 28 k^0_{eff}:14.2	Ni%: 30 k^0_{eff}: 4.3	Ni%: 32 k^0_{eff}:11.2	Ni%: 34 k^0_{eff}: 8.3	Ni%: 36 k^0_{eff}:12.6	Ni%: 38 k^0_{eff}:12.0
Ni%: 42 k^0_{eff}:10.5	Ni%: 46 k^0_{eff}: 5.4	Ni%: 50 k^0_{eff}: 7.8	Ni%: 52 k^0_{eff}:12.3	Ni%: 54 k^0_{eff}:12.6	Ni%: 58 k^0_{eff}: 6.2
Ni%: 60 k^0_{eff}: 4.7	Ni%: 62 k^0_{eff}: 6.6	Ni%: 64 k^0_{eff}: 8.9	Ni%: 66 k^0_{eff}: 8.7	Ni%: 68 k^0_{eff}: 9.3	Ni%: 70 k^0_{eff}:17.2
Ni%: 72 k^0_{eff}:10.0	Ni%: 74 k^0_{eff}:10.5	Ni%: 76 k^0_{eff}: 8.9	Ni%: 78 k^0_{eff}:21.9	Ni%: 80 k^0_{eff}:19.5	Ni%: 84 k^0_{eff}:15.5
Ni%: 86 k^0_{eff}:13.2	Ni%: 88 k^0_{eff}:22.4	Ni%: 90 k^0_{eff}:20.0	Ni%: 94 k^0_{eff}:11.2	Ni%: 96 k^0_{eff}:17.4	Ni%:100 k^0_{eff}: 8.1

Table 1: Concentration gradient for NiMo bimetallic catalyst HER in pH 2 phosphate buffer electrolyte with respective $k^0 = k^0_{eff} * 10^8$ values in cm s^{-1}.

Ni%: 0 k^0_{eff}: 278	Ni%: 4 k^0_{eff}: 200	Ni%: 6 k^0_{eff}: 151	Ni%: 8 k^0_{eff}: 389	Ni%: 10 k^0_{eff}: 389	Ni%: 12 k^0_{eff}: 634
Ni%: 14 k^0_{eff}: 575	Ni%: 16 k^0_{eff}: 806	Ni%: 18 k^0_{eff}: 977	Ni%: 20 k^0_{eff}: 456	Ni%: 22 k^0_{eff}: 102	Ni%: 28 k^0_{eff}: 389
Ni%: 30 k^0_{eff}: 141	Ni%: 34 k^0_{eff}: 132	Ni%: 38 k^0_{eff}: 216	Ni%: 42 k^0_{eff}: 507	Ni%: 46 k^0_{eff}: 977	Ni%: 48 k^0_{eff}:1023
Ni%: 52 k^0_{eff}: 661	Ni%: 54 k^0_{eff}: 933	Ni%: 58 k^0_{eff}: 955	Ni%: 62 k^0_{eff}: 977	Ni%: 64 k^0_{eff}: 275	Ni%: 66 k^0_{eff}: 135
Ni%: 72 k^0_{eff}: 123	Ni%: 74 k^0_{eff}: 162	Ni%: 76 k^0_{eff}: 195	Ni%: 78 k^0_{eff}: 403	Ni%: 80 k^0_{eff}: 170	Ni%: 82 k^0_{eff}: 302
Ni%: 84 k^0_{eff}: 114	Ni%: 88 k^0_{eff}: 98	Ni%: 92 k^0_{eff}: 117	Ni%: 96 k^0_{eff}: 566	Ni%: 98 k^0_{eff}: 526	Ni%:100 k^0_{eff}: 385

Table 2. Concentration gradient for NiMo bimetallic catalyst HER in pH 7 phosphate buffer electrolyte with respective $k^0 = k^0_{eff} * 10^8$ values in cm s^{-1}.

CHAPTER 3: Use of Fuzzy Logic Controls for Automated Approach of SECM UME for Surface Interrogation

INTRODUCTION

Scanning Electrochemical Microscopy (SECM) is an electrochemical scanning probe technique that is frequently used to study homogeneous[45-46] and heterogeneous kinetics,[47-50] biological systems,[11, 51-55] electrocatalysts,[37, 43] semiconductor surfaces,[24, 56] reaction intermediates,[57-59] and topographical and reactivity imaging[60-66] (including constant current techniques)[67-68] among many others.[69-71] Several variations of SECM, such as Scanning Electrochemical Cell Microscopy (SECCM), which is a pipette based imaging technique that is able to obtain electrochemical and topographical images, have also been developed.[61-62, 72] For all of these SECM techniques, one typically approaches a small tip electrode to be in very close proximity to a substrate electrode.[73] For example, when studying homogeneous kinetics, a small tip/substrate distance is obtained to increase mass transfer to the tip electrode so that fast kinetics can be measured more accurately.[74]

Typically the first step in obtaining a small tip/substrate distance is to perform an "approach curve" where the tip electrode steadily approaches the substrate electrode and stops a short distance from the substrate. When using the feedback mode of SECM to measure homogenous kinetics, one usually performs an approach curve to obtain tip/substrate distance of less than 1 tip radius in order to be in a regime with increased mass transfer to the tip electrode.[74] Obtaining this small tip/substrate distance can prove challenging when approaching the substrate at a constant-speed. When approaching at a constant-speed, the tip electrode must approach slowly in order to avoid crashing into the

substrate, but quickly enough that it does not make a single measurement impractical due to the requisite length of time.

In this manuscript we present an alternative method in which the speed of the SECM electrode varies depending on the tip/substrate distance and the size of the electrode. In addition, this technique alternates between using coarse and fine motion controllers depending on the tip/substrate distance and also stops the tip electrode once a preprogrammed set-point has been reached to avoid crashing the tip into the substrate. Thus, this technique will approach large electrodes relatively quickly at greater distances from the substrate and approach smaller electrodes comparatively slowly as the ultramicroelectrode, UME, gets closer to the substrate. It also allows for relative small tip/substrate distances to be obtained rapidly for both large and small tip electrodes without crashing the tip electrode. Upon reaching the desired distance of less than one radius from the substrate surface, our algorithm stops the tip electrode so experiments can be performed at small tip/substrate distances.

While many control mechanisms have been utilized for motion control (e.g. PID),[65, 75] in this manuscript a fuzzy logic algorithm was used to control the SECM tip motion. Fuzzy logic utilizes rule-based decision making for process control and, as opposed to Boolean logic where events are in either one set or another, fuzzy logic allows for events to have partial memberships in multiple sets.[75] Thus, with fuzzy logic control, one describes the control strategy qualitatively and the controller uses a rule strategy to determine the output of the controller.

Fuzzy logic was the control mechanism of choice because of its ease of creating linguistic variables, linguistic terms, and membership functions for the inputs (tip size, tip

current, and set-point) and outputs (tip speed) as well as a rule-based linguistic control strategy to facilitate smooth changes in tip speed as the tip approaches the substrate. This allows for one single algorithm to be used for both large and small tip electrodes.

Here we demonstrate the functionality of this fuzzy logic control algorithm by obtaining positive feedback[74, 76] approach curves with a large tip electrode (d = 175 µm) typical of the size used in Surface Interrogation SECM,[59] and with a conventional UME, (d = 4.2 µm and d = 6.2 µm). In addition, we were able to demonstrate the ability to accurately measure homogenous electron transfer kinetics with small tip/substrate distances by quantifying the kinetic rate constant for ferrocenemethanol oxidation.

EXPERIMENTAL

Chemicals: All solutions were prepared with deionized Milli-Q water, and the chemicals purchased from the following were used as received: ferrocenemethanol (FcMeOH, 97%) from Sigma-Aldrich and sodium nitrate ($NaNO_3$, ≥ 99%) from Fisher Scientific.

Pt Microdisk Electrodes: Microdisk electrodes of two different tip diameters (c.a. 200 µm and c.a. 10 µm) were fabricated for the SECM experiments. Quartz capillaries (1 mm O.D., 0.3 mm I.D., Sutter Instruments, USA), 200 µm diameter platinum wire (Electron Microscopy Sciences 99.95% Pt wire), borosilicate glass capillaries (1 mm O.D., 0.5 mm I.D., Sutter Instruments, USA), 10 µm diameter platinum wire (0.01 mm, 99.9% Pure, Hard, Goodfellow, Cambridge, England), a laser pipet puller (Model P-2000, Sutter Instruments, USA), standard razor blades, conductive silver epoxy (Circuit Works, USA),

and silver connection wire (30 AWG, Belden, USA) were utilized to manufacture the UME's. MicroCut 1200 grit silicon carbide grinding paper (P2500, Buehler, Canada), alumina micropolish (1 µm, 0.3 µm, 0.05 µm, Beuhler, Canada), and MicroCloth polishing disks (Beuhler, Canada) were used to polish the tips of the UME's before experimentation.

Electrode Fabrication: Fabrication of micro- and ultramicro- electrodes were completed by nesting platinum wire in capillary tubes, then using a laser capillary pipet puller (Sutter P-2000) to seal the capillary around the wire and pull it to a tip. Each electrode tip was then polished flat and smooth using alumina micropolish. The resulting tips that were used in these experiments were of 4.4 µm, 6.2 µm, and 175 µm diameters.

200 µm Electrodes: The quartz capillary and 200 µm Pt wire were rinsed with deionized water and allowed to air dry before assembly. A short (~3cm) section of Pt wire was threaded and centered in the quartz capillary. The capillary/wire assembly was then centered and secured to the laser pipet puller. A single line program (Heat: 850, Filament: 1, Velocity: 50, Delay: 100, Pull: 225) was run so that the capillary/wire assembly split and sealed into two UME's of approximately equal size. The UME's were polished on the MicroCut grinding paper to expose the Pt wire at the tip. A figure eight motion was used in polishing to ensure a flat platinum disk surface. Using the 1 µm and 0.3 µm alumina micropolish and MicroCloth disks, rough patches and scratches on the UME tip were buffed out to leave a smooth, even surface. The final size of the electrode was determined to be d = 175 µm due to slight stretching of the Pt wire during fabrication.

10 µm Electrodes: The general procedure for the 10 µm capillary/wire assembly was similar to the steps outlined for the 100 µm assembly. The borosilicate glass capillary and 10 µm Pt wire were rinsed with deionized water and allowed to air dry. A small section of Pt wire (~3 cm) was threaded and centered into the quartz capillary. The capillary/wire assembly was secured to the laser puller. The UME fabrication procedure required three steps: stretching, sealing, and pulling. To stretch and thin the capillary, a four-line program was run (Heat: 300, Filament: 4, Velocity: 14, Delay: 120, Pull: 0) followed by a single-line break (Heat: 0, Filament: 4, Velocity: 14, Delay: 120, Pull: 0). Without removing the assembly, the sealing step was performed by blocking the slight pulling force (at Pull: 0) with razor blades placed between the bearing and the capillary clamp on each side of the puller. A single line program (Heat: 320, Filament: 4, Velocity: 12, Delay: 120, Pull: 0) was manually run and repeated eight times at intervals of five seconds. To pull the electrodes, the razor blades were removed and the sealing program was allowed to run automatically, with one heating cycle followed by a clean split (~0.6 seconds to complete) resulting in two sealed UME's of approximately equal size. The UME's were polished on a microcut disk with 0.05 µm alumina micropolish in a slight side-to-side movement, ensuring no pressure was applied on the tip.

UME Completion: To complete each UME, a conductive epoxy and silver wire were applied to the open end of the capillary. Silver epoxy and hardener were mixed together. This mixture was forced into the open end of the UME through capillary action, carefully tapping the mixture into the tube. A large segment (~6 cm) of silver connection wire was straightened by rolling it against a flat surface and epoxy was applied to the end

of the wire before inserting into the capillary. The wire was inserted through the epoxy mixture until it met the 10 µm wire. A final epoxy application to the end of the capillary ensures the silver wire is sealed into place. The UMEs were allowed to cure at room temperature in a well ventilated area for 24 hours. Each UME was imaged with a digital compound microscope (Micromaster II Digital Microscope with Phase Contrast, Fisher Scientific, USA). A top view of each UME was generated by suspending the UME on the microscope stage with forceps (Figure 3.1). Both views were saved as images using the microscope's accompanying digital program (Micron) to capture the field of the microscope view. The contrast levels were then adjusted to improve the image clarity.

SECM Instrumentation: All SECM experiments were performed with our custom-built SECM (Figure 3.2). For the motion control, two separate systems were utilized to achieve both coarse and fine control. The coarse substrate control is performed with a Newport VP-25XL- XYZ, which moves the substrate electrode into close proximity of the SECM tip. This stage is able to move in the X, Y, and Z directions and has a total range of 25 mm with a minimum increment motion of 10 nm in each direction. This coarse control allows us to position the SECM tip close to the substrate before engaging the fine nanopositioner control. For the fine tip control, we use a highly-precise 3-axis piezo controller (Newport NPXYZ100SG-D) with a feedback system to eliminate any hysteresis in the piezo control. This nanopositioner is able to move in the X, Y, and Z directions and has a travel range of 100 µm and a resolution of 0.2 nm. The entire system, including the bipotentiostat (CHI Instruments 660E), is computer-controlled using custom software built with LabVIEW.

RESULTS AND DISCUSSION

Control Algorithm: To control the motion of the SECM tip electrode, a custom fuzzy logic control algorithm was developed using National Instruments (Austin, TX) PID and Fuzzy Logic Toolkit. We used three linguistic variables for the inputs into the fuzzy logic algorithm and one linguistic variable for the output. The input linguistic variables are tip size (i.e. radius of the tip), present enhancement factor (i.e. the current enhancement factor defined as the ratio of the tip current over the tip current at infinite distance from the substrate at the present instance in time), set-point difference (i.e. the difference between the present enhancement factor and the user-entered enhancement factor at which to stop the SECM tip electrode), and the output linguistic variable is step size (i.e. the size of the step to move the SECM tip electrode towards the substrate). The output variable step size is directly related to the speed of the approach curve because this process is repeated in a continuous loop with a specified loop duration.

Each of the input and output linguistic variables has five linguistic terms: extra-small, small, medium, large, and extra-large. Each of these linguistic terms is defined using membership functions (Figures 3.3 a-c) which represents the degree of membership that each of the linguistic variables has with its corresponding linguistic terms.

The implementation of the control algorithm is described in Figure 3.3. First, the algorithm takes the user-entered values for the SECM tip size and the enhancement factor set-point. Then, using the bipotentiostat, the LabVIEW software measures the present enhancement factor by measuring SECM tip current and dividing by the tip current at

infinite distance away from the substrate. The set-point difference is calculated by subtracting the present enhancement factor by the enhancement factor set-point. The three input linguistic variables are then assigned membership to a linguistic term (e.g. extra-small, small, medium, large, extra-large) via the membership functions shown in Figure 3.3 a-c. Recall that, with fuzzy logic, the input values do not need to be assigned membership to only one linguistic term, but can be assigned a weighted partial membership to multiple linguistic terms based on the membership functions.

Once each of the input linguistic variables is assigned membership, the output is then determined via the rule base shown in Figure 3.3 d. This rule base is a compilation of weighted rules, which assign a linguistic term to the output variable based on the inputs. The final output of the fuzzy logic algorithm gives the velocity of the SECM tip based on the linguistic variable inputs, as shown by the flow chart in Figure 3.3. Figures 3.3 f-i show the output speed as a function of the present enhancement factor and set-point difference for four different tip sizes.

SECM Measurements: To test how well the algorithm can generate approach curves for smaller SECM tip electrodes, we fabricated a 4.2 µm diameter electrode as described above and used the fuzzy logic algorithm to obtain a positive feedback approach curve (Figure 3.4 a-b) in a 0.5 mM ferrocenemethanol solution (with 0.1M NaNO3 supporting electrolyte) with a 2 mm diameter Pt substrate electrode. An optical image of the SECM tip is shown in Figure 3.1 a. Before starting the SECM experiment, linear sweep voltammetry was performed at a tip/substrate distance of 100 µm. Then, the approach algorithm was executed producing an approach curve with an enhancement factor of 3.5

which corresponds to a tip/substrate gap of 580 nm (Figure 3.4 a). Linear sweep voltammetry was performed again at this electrode gap size. COMSOL Multiphysics was used to simulate the approach curve and linear sweep voltammograms in order to extract kinetic parameters and rate constants.

Another approach curve was conducted with the 4.2 μm diameter UME using a conventional constant-speed linear approach, the most commonly used method, to compare the conventional and fuzzy logic approach curves. Figure 3.4 a shows the comparison between the constant-speed approach curve, the fuzzy logic approach curve, and a simulated approach curve using COMSOL. Both the constant-speed approach curve and the fuzzy logic approach curve fit the simulated approach curve. However, the conventional constant-speed approach curve obtained an electrode gap of 700 nm (enhancement factor of 3.3), while the fuzzy logic approach curve obtained an electrode gap of 580 nm.

Figure 3.4 b shows the tip displacement and tip speed as a function of time for the fuzzy logic approach curve and the constant-speed approach curve. Figure 3.4 b also shows that, by utilizing the fuzzy logic control algorithm, the user has more control, precision, and adaptability as compared to the conventional constant-speed approach. In these experiments, the same approach distance with a 4.2 μm diameter UME consistently took approximately one-third of the time to complete. In addition, the fuzzy logic algorithm varies the speed of the approach from c.a. 300 nm/s at large tip/substrate distances to 10 nm/s as the tip electrode nears the substrate electrode. This provides more data points and slower approach where there is more rapid change in enhancement factor and faster approach through the lower enhancement factor regions, saving time and improving the

data collection at higher sensitivities. The fuzzy logic approach curve is also able to switch between the coarse control and the fine control when the speed goes below 20 nm/s and the enhancement factor can be set as a target and updated to give a stepwise approach. Also, the fuzzy logic algorithm is able to stop the tip electrode at a pre-programmed enhancement factor, which prevents the tip from "crashing" into the substrate.

To test how the algorithm can generate approach curves for larger SECM tip electrodes, typical of the size used for SI-SECM, the same procedure was completed with the 175 µm electrode. The fuzzy logic algorithm produced an approach curve to an enhancement factor of 10 (Figure 3.5 a-b). This resulted in a tip/substrate distance of 6.5 µm, at which linear sweep voltammetry was performed to measure the FcMeOH redox reaction (Figure 3.6). We also report using this fuzzy logic algorithm on a 6.2 µm UME, for which we obtained an 800 nm tip/substrate distance (Figure 3.7 a-b).

From the linear sweep voltammetry experiments, using both the 4.2 µm and 6.2 µm electrodes at the tip/substrate distances of 580 nm and 800 nm respectively, the reaction kinetics for ferrocenemethanol oxidation were simulated and fit to the raw experimental data to determine the reaction rate constant, k^0, for the 4.2 µm (Figure 3.8) and 6.2 µm (Figure 3.9) electrodes. Figures 3.8 and 3.9 show how the 580 nm gap is able to better distinguish between rate constants between 0.1 and 0.5 cm s^{-1} compared to the 800 nm gap. Using these simulations along with a more focused array (Figure 3.10), we quantify the kinetics of ferrocenemethanol oxidation to be k^0=0.20±0.05 cm s^{-1}. This is in agreement with previous results, which used fast scan linear sweep voltammetry[77] and SECM.[78]

SECM Experimental Procedure: A custom SECM was used for these experiments (Figure 3.2). Components include the following from Newport: 3-axis motion stage (VP-25XL-XYZL), Series 37 tilt stage, piezoelectric nanopositioner (NPXYZ100SG-D), Vision Isostation air table (VIS2436-IG2-125A), faraday cage for air table, XPS Motion Controller/Driver with XPS-DRVP1 driver boards, 2 tilt stage motors (LTA-HS), small L-mount (EQ80-I), larger L-mount (EQ80-E), Cable Management System (CMS), vertical rail and mount for nanopositioner. In addition to these components, the SECM also includes a CH Instruments potentiostat (CHI730E) and an iMac computer running custom designed LabVIEW software to control the instrument.

The custom LabVIEW software is capable of performing linear sweep voltammetry, linear approach curves, and fuzzy logic-based approach curves. By inputting parameters (electrode tip size, desired setpoint difference, desired enhancement factor), the fuzzy logic approach software will dictate what speed of approach is appropriate for the system parameters at the given point, adjusting the speed and slowing down gradually as the electrode gap is lessened.

COMSOL Multiphysics Simulation Details

In order to analyze the SECM approach curves and linear sweep voltammograms, COMSOL Multiphysics simulation software was used to fit the experimental results. A two-dimensional axial symmetric geometry of the SECM tip electrode and substrate counter electrode system with electrolyte solution was constructed for conducting these simulations. A mesh was then assigned to this geometry, concentrating calculations on and

around the surface reaction sites. Once the geometry and mesh were complete, the physics packages were loaded, including Transport of Dilute Species and Electroanalysis.

The Transport of Dilute Species physics solves the reactive species concentrations by means of the equations from Fick's laws of diffusion. Coupled with the species transport is the Electroanalysis physics package, which incorporates the Butler-Volmer equation of electrochemical reaction kinetics. Since the concentrations from the transport physics is coupled with the concentrations in the Butler-Volmer equations, these equations must be solved simultaneously by numerical methods. For the simulations used in this manuscript, the diffusion coefficient of both the oxidized and reduced form of FcMeOH was taken to be 7.1 x 10-6 cm2 s^{-1} and E^0 for the oxidation of FcMeOH was taken to be 0.218 V vs Ag/AgCl.[78] By feeding in the raw experimental data, the other variables in these equations are known, allowing COMSOL to determine the unknown kinetic parameters, such as k^0, by curve fitting at multiple k^0 values and comparing the results. For all Butler-Volmer simulations, the transfer coefficient, α, was taken to be 0.5. The results of these simulations (k^0 = 0.20 ± 0.05 cm s^{-1}) can be seen in the curve fittings in Figure 3.10.

CONCLUSION

The fuzzy logic based automated variable-speed approach method proposed in this paper proved to be an effective development for SECM automation and adaptable system programming. The implementation of this method using a UME to approach a substrate surface and collect kinetic data via linear sweep voltammetry on ferrocenemethanol, a difficult-to-measure reactive system, shows the viability and capability of this technique.

The value of k^0=0.20±0.05 cm s^{-1} agrees with past research conducted with different measurement techniques. With one system setup, a wide range of tip sizes and approach methods are possible, allowing for more control and precision, while substantially reducing the risk of "crashing" the tip into the substrate. Fuzzy logic, as used in this instance, provides a more adaptable, smoother step transitioning method for programming process controls in SECM motion control and approach algorithms.

CHATER 3 FIGURES

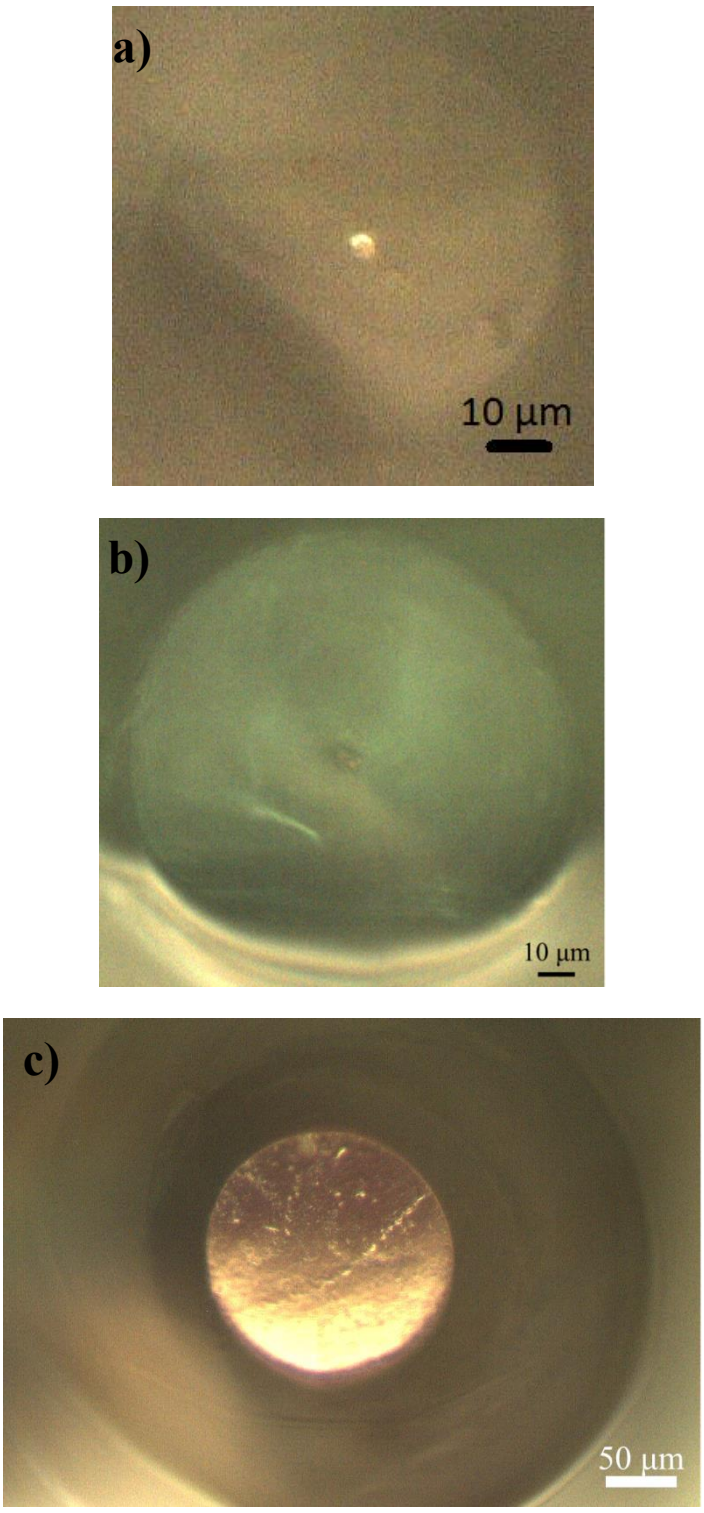

Fig 3.1: Optical microscope images of: (a) 4.2 µm diameter SECM electrode tip, (b) 6.2 µm diameter SECM electrode tip, and (c) 175 µm diameter SECM electrode tip.

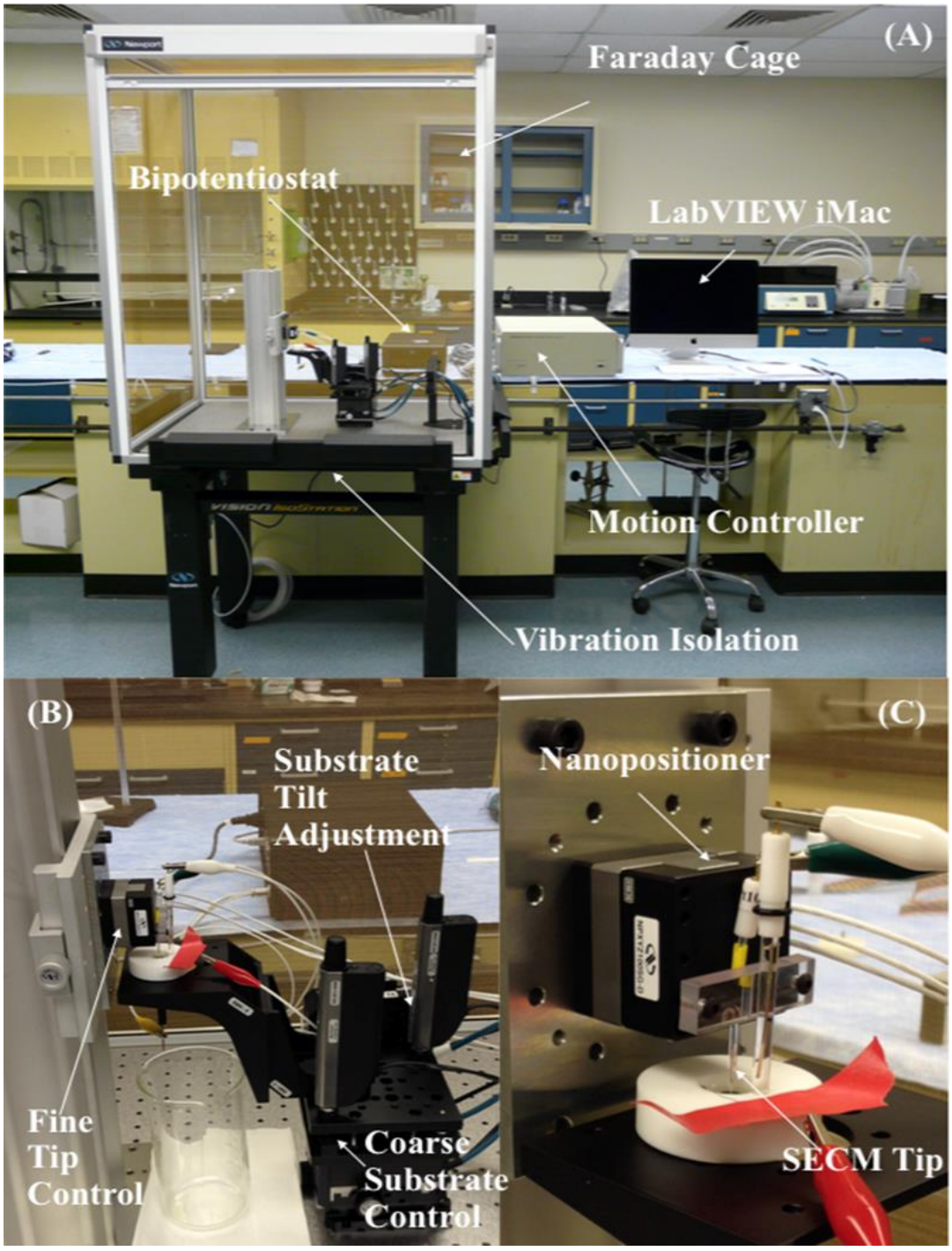

Fig 3.2: (A) Custom made Scanning Electrochemical Microscope (SECM); (B) Newport multi-axis motion controller stages; (C) piezoelectric nanopositioner for SECM electrode tip.

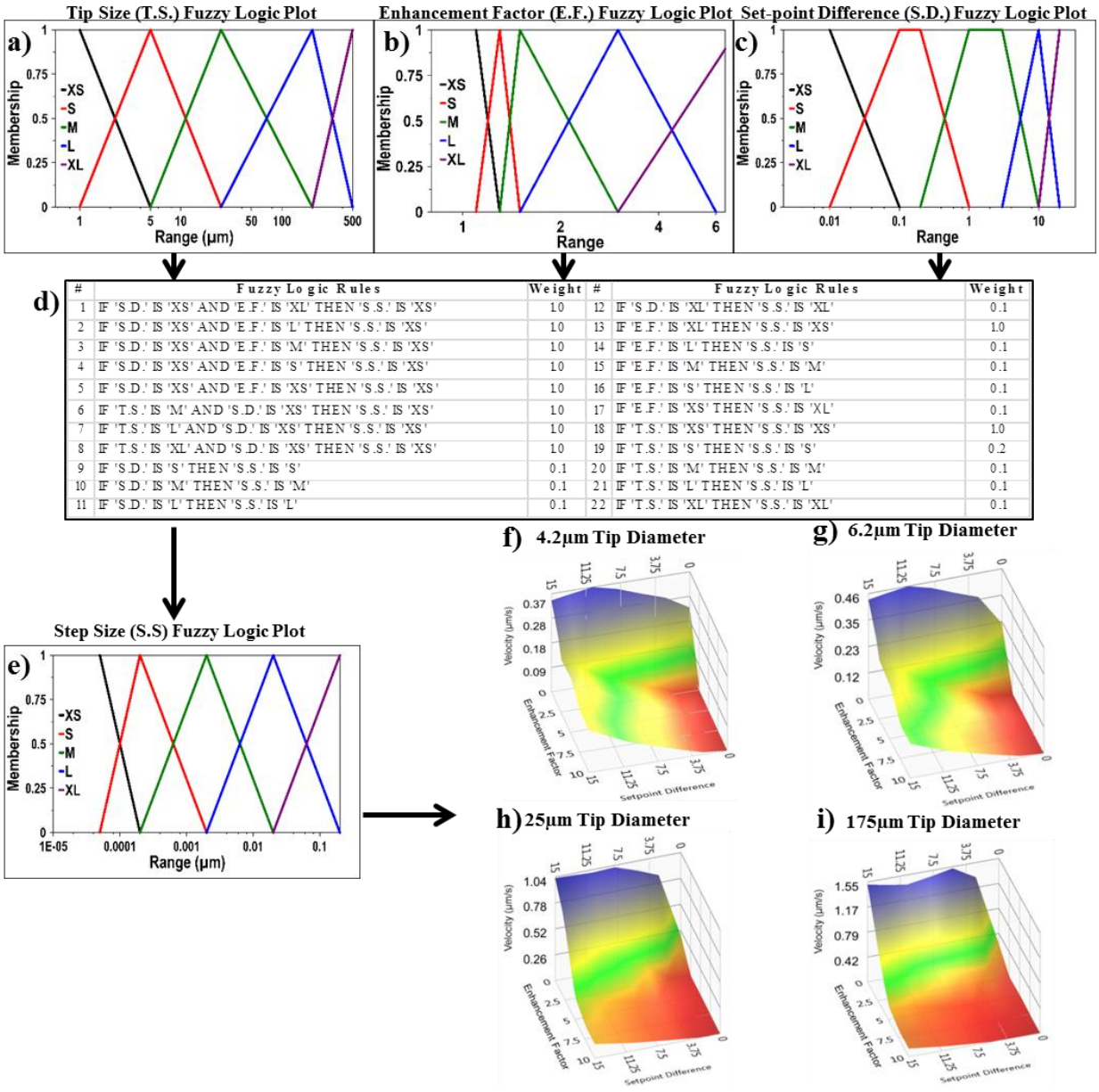

Fig 3.3: SECM Fuzzy Logic process flow chart detailing the membership functions controlling each input parameter (tip size, enhancement factor, set-point) (a-c), the rule table (d), which dictates the step size given the values of the three input parameters, the step size output membership function (e), and the tip velocity plots generated for the automated SECM tip movement showing what the tip velocity should be as a function of the enhancement factor and set-point difference (f-i) for four different tip sizes. For a given tip size, the logic will determine step size for the electrode approach based on the weighted results from the rule table. With a set loop speed for the algorithm, the step size pro-duces an approach velocity for the electrode tip.

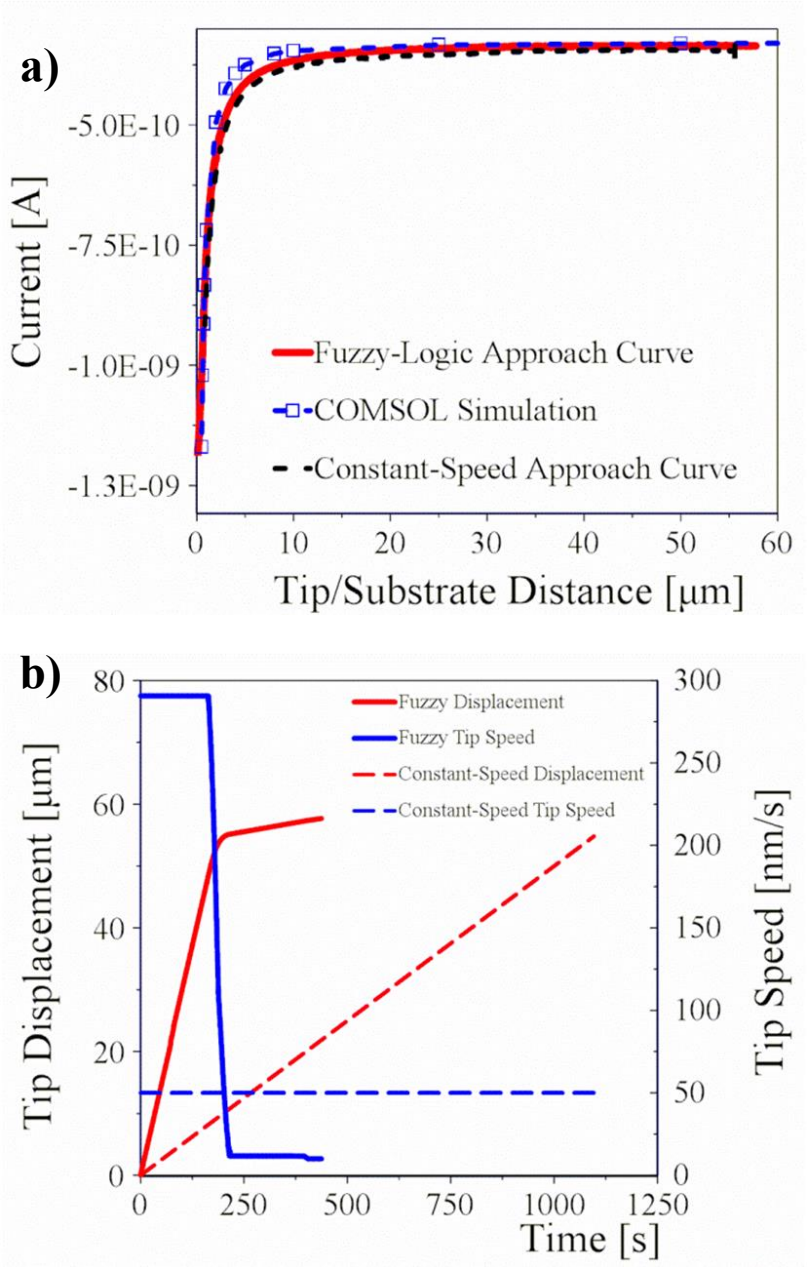

Fig 3.3: (a) SECM approach curves using the fuzzy logic algorithm with a 4.2 µm Pt tip electrode at 0.4 V vs Ag/AgCl and a 2 mm Pt substrate electrode at 0.05 V vs Ag/AgCl in 0.5 mM FcMeOH along with the corresponding constant-speed approach curve and COMSOL simulation; (b) the corresponding tip displacement and tip speed for the fuzzy logic and constant-speed approach comparison plot.

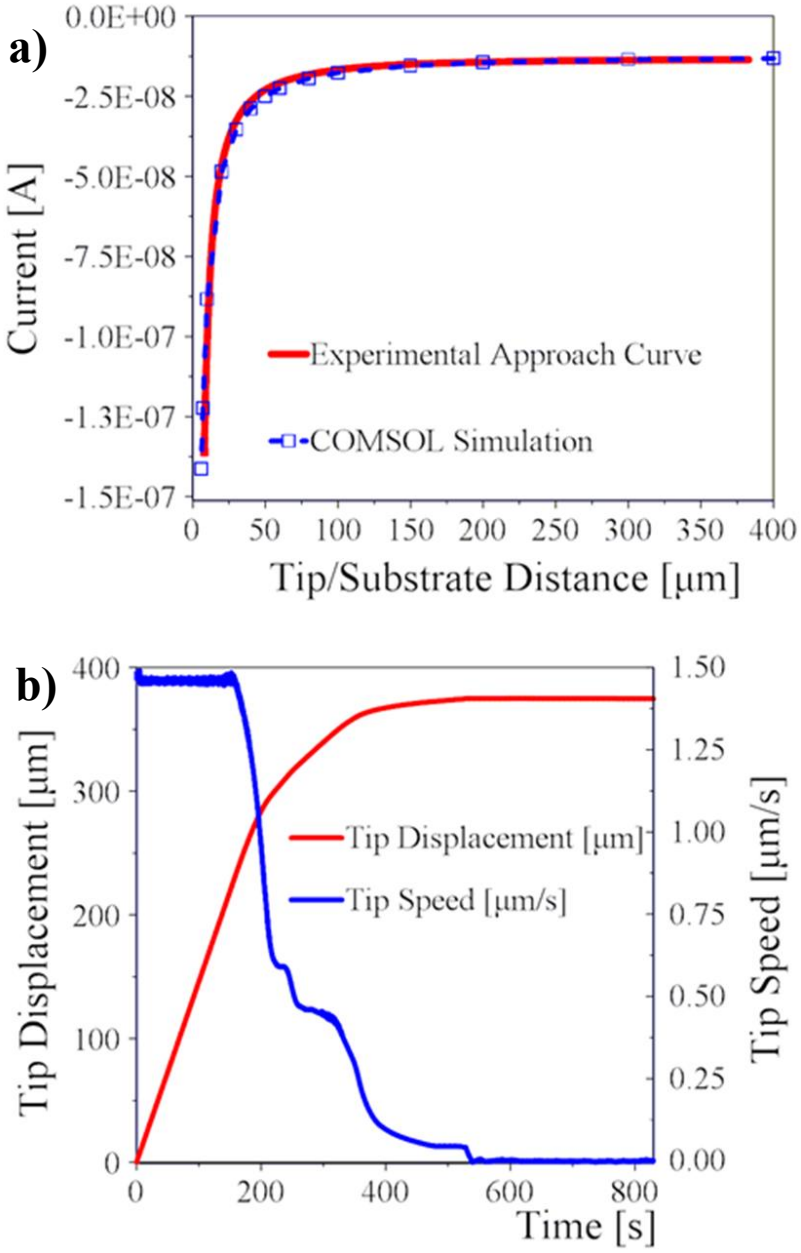

Fig 3.5: (a) SECM approach curve using the fuzzy logic algorithm with a 175 µm Pt tip electrode at 0.4 V vs Ag/AgCl and a 2 mm Pt substrate electrode at 0.05 V vs Ag/AgCl in 0.5mM FcMeOH along with the corresponding COMSOL simulation**.** (b)The corresponding tip displacement and tip speed for the fuzzy logic approach curve comparison plot.

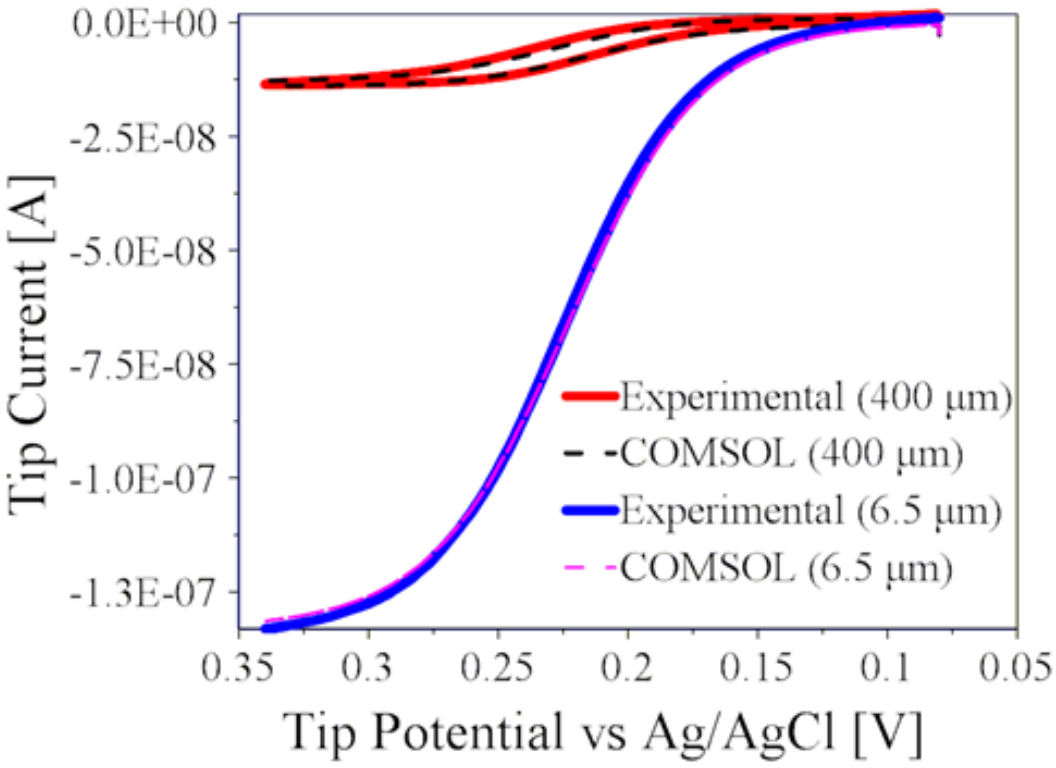

Fig 3.6: Linear sweep voltammogram and corresponding COMSOL simulations at a tip/substrate distance of 400 µm and 6.5 µm for the 175 µm Pt tip electrode at 0.4 V vs Ag/AgCl and a 2 mm Pt substrate electrode at 0.05 V vs Ag/AgCl in 0.5mM FcMeOH.

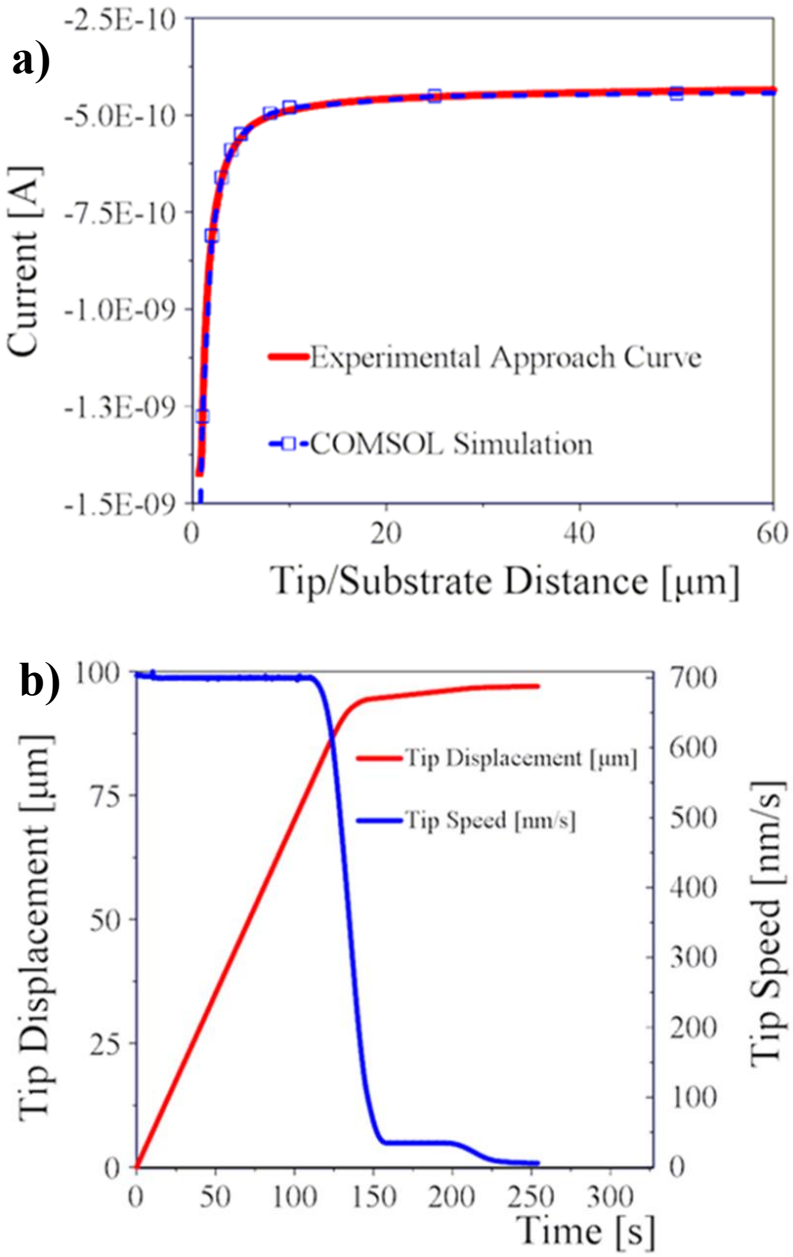

Fig 3.7: SECM approach curve using the fuzzy logic algorithm with a 6.2 µm Pt tip electrode at 0.4 V vs Ag/AgCl and a 2 mm Pt substrate electrode at 0.05V vs Ag/AgCl in 0.5 mM FcMeOH along with the corresponding COMSOL simulation. (b) The corresponding tip displacement and tip speed for the fuzzy logic approach curve comparison plot.

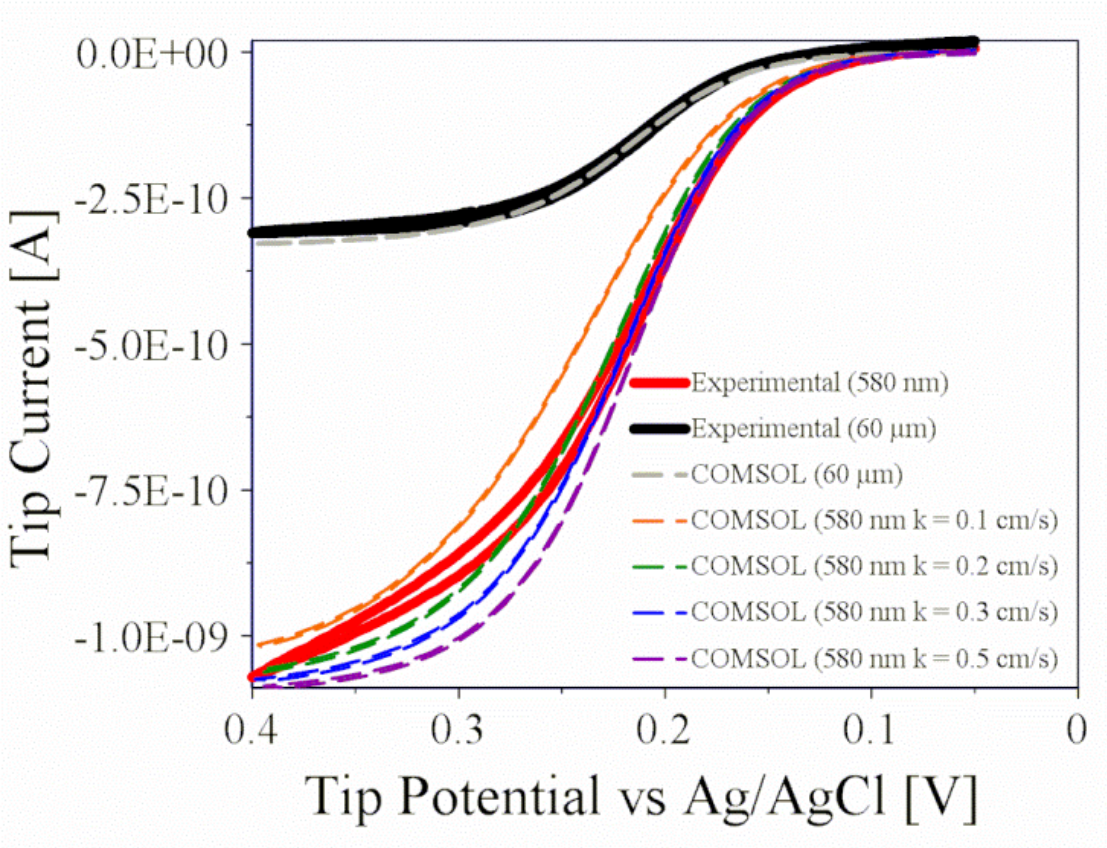

Fig 3.8: Cyclic voltammograms showing both the experimental data and COMSOL simulations of a range of potential k^0 values for FcMeOH oxidation with the 4.2 µm Pt UME at a tip/substrate distance of 60 µm and 580 nm.

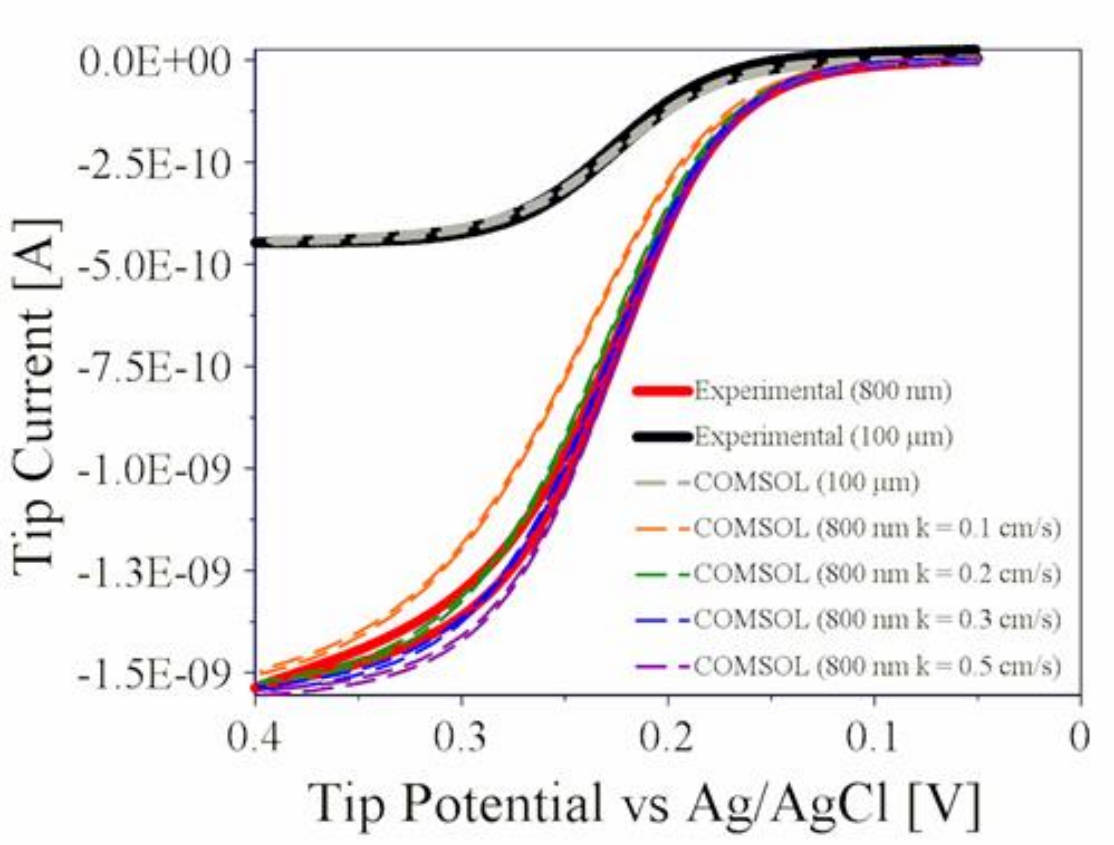

Fig 3.9: Cyclic voltammograms and COMSOL simulation parameter fitting for k^0 values for the FcMeOH redox reaction simulating a range of potential k^0 values with the 6.2 µm UME at an electrode gap distance of 800 nm and 100 nm. An improvement in accuracy is seen with the smaller electrode gap from Fig 3.8.

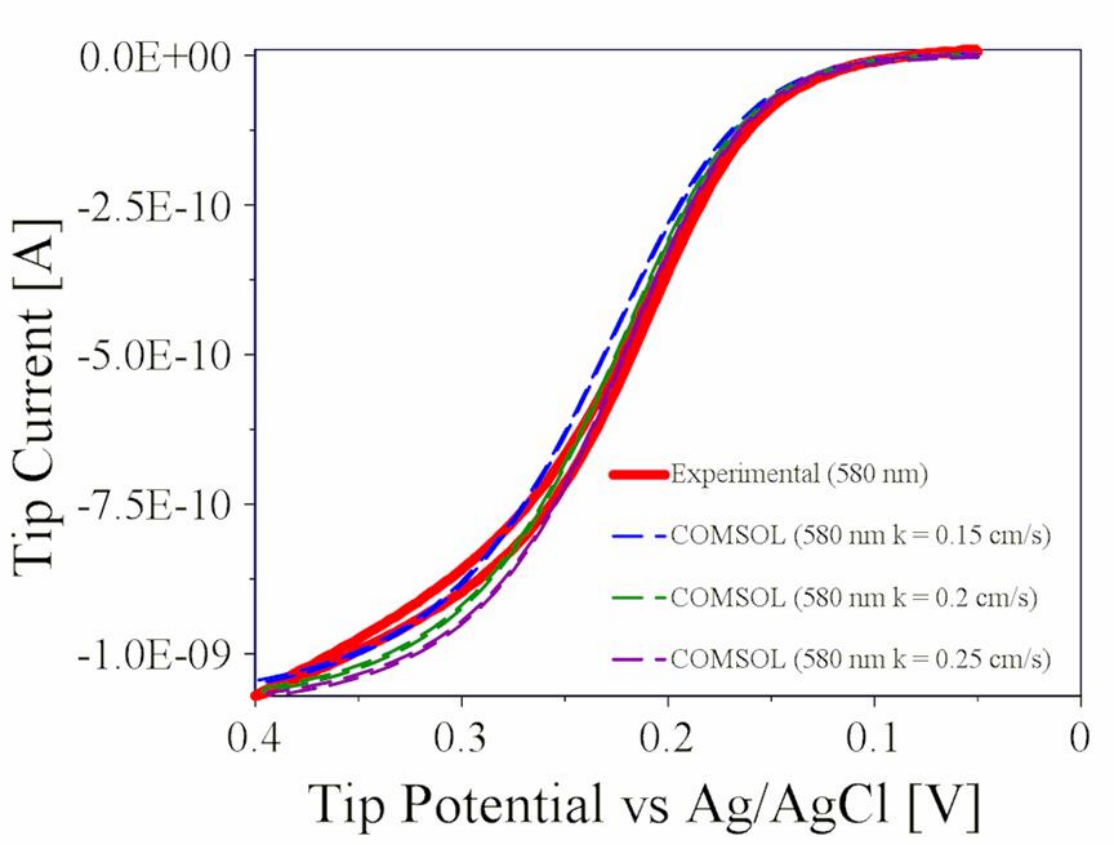

Fig 3.10: Cyclic voltammogram and COMSOL simulation parameter fitting for k^0 values for the FcMeOH redox reaction simulating the identified accurate region of k^0 values (based on results from Fig 3.9) with the 4.2 µm UME at an electrode gap distance of 580 nm. From these results k^0 =0.20±0.05 cm s^{-1}.

CHAPTER 4: Future Work

The benefit of this new rapid screening method for electrocatalysts goes beyond the NiMo catalyst for the aqueous hydrogen evolution reaction. Conceivably, any catalyst system capable of reacting within an electrolytic cell can be studied using this method. Other methods of catalyst deposition (i.e. sputter coating, drop casting, film growth, electrodeposition,[79] etc.) can be used in cases where the piezoelectric printing of metal precursor solutions is not viable. For metal oxide catalysts, firing the precursors in air, rather than reducing under a H_2 flow, will result in oxides forming. Because of this inherent versatility, the scope of this method is very broad and applicable to finding new catalysts by a much more efficient method.

An array of iron nickel oxide ($Fe_zNi_{1-z}O_x$) was analyzed to demonstrate the viability of studying water oxidation reactions on metal oxides as an application of this rapid screening method. The same procedure was used as in Chapter 2 to print the sample slide, but using iron(III) nitrate nonahydrate (ACS grade Acros Organics) instead of the molybdenum salt. Then the samples were fired at 525°C in a box furnace in air for 3 hours to form metal oxides. A 1.0 M NaOH (ACS grade Fisher Scientific) electrolyte solution (pH 14) was bubbled for 10 minutes with argon and then used with the 2% increment array of iron-nickel oxide catalysts. A platinum counter electrode was used with a Ag/AgCl reference electrode and an argon purged reaction cell headspace. The linear sweep voltammetry was performed from 0 – 1.5V at 1 mV s^{-1}. From the data collected, there are definite trends to suggest areas of high catalytic activity within the incremental composition array (Figure 4.1).

At the current development stage of this analytical method, it is not a perfectly accurate method. There is room for vast improvement to all facets of instrumentation. That being said, it is wholly viable as a means of screening catalysts to determine which are worthy of undergoing much more time consuming and more in-depth analytical methods, such as assorted SECM techniques.

Combining these methods will result in a much more efficient way of screening catalysts. In this work, the effectiveness of these new screening methods is clearly shown. Even though a relatively well known reaction and catalyst system was studied, there has not previously been a NiMo study this in-depth, analyzing 2% differences in concentration. By applying the ease of operation, inherent versatility, and speed of sampling, data collection for preliminary catalytic studies on electrocatalysts will be much easier and faster to complete, allowing for a more educated decision on which catalysts are worth time and expense to analyze more fully with SECM techniques.

Conceivably, the larger amount of data collected on electrocatalysts by this method will allow for a database of kinetic results to compare with physical properties of the catalyst components, such as melting point, bulk modulus, crystal structures, etc. in order to further understand what characteristics contribute to favorable catalysts and how to predict catalytic behaviors.

Future work refining these techniques will improve capabilities and efficiency of catalyst design. By simply altering the reaction setup, one can create a purpose built rapid screening apparatus for catalyst testing. For example, by adding a light source, this method could be used for high-throughput tests on photocatalysts. Goals for future work on the

SECM part of this project include reaching electrode gap sizes of < 100 nm to allow for high resolution measurements of electron transfer kinetics. To accomplish this level of accuracy, electrode tip sizes of < 500 nm must be used. This level of resolution would allow for catalyst interrogation to determine the effect of surface characteristics, crystal structures, lattice spacing, etc. on catalytic activity. There is great potential for these rapid screening methods to push the envelope or high throughput electrocatalyst testing and adding to the field of electrochemistry.

CHATER 4 FIGURES

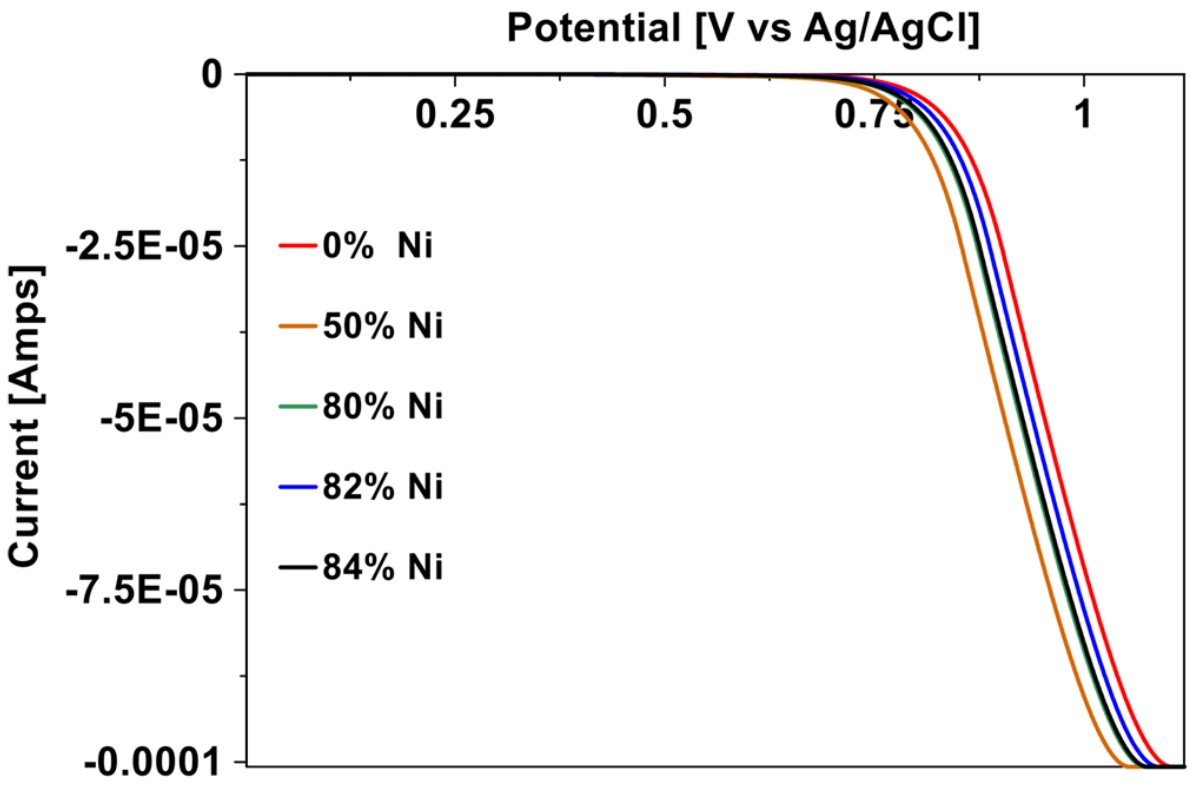

Fig 4.1: $Fe_zNi_{1-z}O_x$ water oxidation catalyst preliminary results in 1 M NaOH aqueous electrolyte. The gradient of LSV results shows that the data is matching expected trends in catalytic activities.

REFERENCES

1. Assessing Current, Near-term, and Long-term U.S. Hydrogen Markets. http://www.dis.anl.gov/news/HydrogenMarkets.html (accessed October 2, 2014).
2. Scholz, W. H., Processes for industrial production of hydrogen and associated environmental effects. *Gas Sep. Purif.* **1993,** *7*, 131-139.
3. Alsema, E. A.; Nieuwlaar, E., Energy viability of photovoltaic systems. *Energ Policy* **2000,** *28* (14), 999-1010.
4. Vennestrøm, P. N. R.; Osmundsen, C. M.; Christensen, C. H.; Taarning, E., Beyond Petrochemicals: The Renewable Chemicals Industry. *Angew Chem Int Edit* **2011,** *50*, 10502-10509.
5. Xu, J. G.; Froment, G. F., Methane Steam Reforming, Methanation and Water-Gas Shift .1. Intrinsic Kinetics. *Aiche J* **1989,** *35* (1), 88-96.
6. Armor, J. N., The multiple roles for catalysis in the production of H-2. *Appl Catal a-Gen* **1999,** *176* (2), 159-176.
7. Rostrup-Nielsen, J. R.; Sehested, J.; Norskov, J. K., Hydrogen and synthesis gas by steam- and CO2 reforming. *Adv Catal* **2002,** *47*, 65-139.
8. Strohm, J. J.; Zheng, J.; Song, C. S., Low-temperature steam reforming of jet fuel in the absence and presence of sulfur over Rh and Rh-Ni catalysts for fuel cells. *J Catal* **2006,** *238* (2), 309-320.
9. Group, S. E., *Instrumental methods in electrochemistry*. Wiley: New York, 1985.
10. Warren, E. L.; McKone, J. R.; Atwater, H. A.; Gray, H. B.; Lewis, N. S., Hydrogen-evolution characteristics of Ni-Mo-coated, radial junction, n(+)p-silicon microwire array photocathodes. *Energ Environ Sci* **2012,** *5* (11), 9653-9661.
11. Hu, K.; Gao, Y.; Wang, Y.; Yu, Y.; Zhao, X.; Rotenberg, S. A.; Gökmeşe, E.; Mirkin, M. V.; Friedman, G.; Gogotsi, Y., Platinized carbon nanoelectrodes as potentiometric and amperometric SECM probes. *Journal of Solid State Electrochemistry* **2013,** *17* (12), 2971-2977.
12. Lewis, N. S.; Nocera, D. G., Powering the planet: Chemical challenges in solar energy utilization. *P Natl Acad Sci USA* **2006,** *103* (43), 15729-15735.
13. Kanan, M. W.; Nocera, D. G., In situ formation of an oxygen-evolving catalyst in neutral water containing phosphate and Co2+. *Science* **2008,** *321* (5892), 1072-1075.
14. Gray, H. B., Powering the planet with solar fuel. *Nat Chem* **2009,** *1* (1), 7-7.
15. Leonard, K. C.; Bard, A. J., Pattern Recognition Correlating Materials Properties of the Elements to Their Kinetics for the Hydrogen Evolution Reaction. *Journal of the American Chemical Society* **2013,** *135* (42), 15885-15889.
16. Fosdick, S. E.; Berglund, S. P.; Mullins, C. B.; Crooks, R. M., Evaluating Electrocatalysts for the Hydrogen Evolution Reaction Using Bipolar Electrode Arrays: Bi- and Trimetallic Combinations of Co, Fe, Ni, Mo, and W. *Acs Catal* **2014,** *4* (5), 1332-1339.
17. Haber, J. A.; Cai, Y.; Jung, S. H.; Xiang, C. X.; Mitrovic, S.; Jin, J.; Bell, A. T.; Gregoire, J. M., Discovering Ce-rich oxygen evolution catalysts, from high throughput screening to water electrolysis. *Energ Environ Sci* **2014,** *7* (2), 682-688.

18. Jaramillo, T. F.; Ivanovskaya, A.; McFarland, E. W., High-throughput screening system for catalytic hydrogen-producing materials. *J Comb Chem* **2002,** *4* (1), 17-22.
19. Fosdick, S. E.; Berglund, S. P.; Mullins, C. B.; Crooks, R. M., Parallel Screening of Electrocatalyst Candidates Using Bipolar Electrochemistry. *Anal Chem* **2013,** *85* (4), 2493-2499.
20. Dang, T.; Ramsaran, R.; Roy, S.; Froehlich, J.; Wang, J.; Kubiak, C. P., Design of a High Throughput 25-Well Parallel Electrolyzer for the Accelerated Discovery of CO2 Reduction Catalysts via a Combinatorial Approach. *Electroanal* **2011,** *23* (10), 2335-2342.
21. Walsh, D. A.; Fernandez, J. L.; Bard, A. J., Rapid screening of bimetallic electrocatalysts for oxygen reduction in acidic media by scanning electrochemical microscopy. *Journal of the Electrochemical Society* **2006,** *153* (6), E99-E103.
22. Nam, K. M.; Park, H. S.; Lee, H. C.; Meekins, B. H.; Leonard, K. C.; Bard, A. J., Compositional Screening of the Pb-Bi-Mo-O System. Spontaneous Formation of a Composite of p-PbMoO4 and n-Bi2O3 with Improved Photoelectrochemical Efficiency and Stability. *J Phys Chem Lett* **2013,** *4* (16), 2707-2710.
23. Bhattacharya, C.; Lee, H. C.; Bard, A. J., Rapid Screening by Scanning Electrochemical Microscopy (SECM) of Dopants for Bi2WO6 Improved Photocatalytic Water Oxidation with Zn Doping. *J Phys Chem C* **2013,** *117* (19), 9633-9640.
24. Leonard, K. C.; Nam, K. M.; Lee, H. C.; Kang, S. H.; Park, H. S.; Bard, A. J., ZnWO4/WO3 Composite for Improving Photoelectrochemical Water Oxidation. *J Phys Chem C* **2013,** *117* (31), 15901-15910.
25. Damian, A.; Omanovic, S., Ni and Ni-Mo hydrogen evolution electrocatalysts electrodeposited in a polyaniline matrix. *J Power Sources* **2006,** *158* (1), 464-476.
26. Navarro-Flores, E.; Chong, Z. W.; Omanovic, S., Characterization of Ni, NiMo, NiW and NiFe electroactive coatings as electrocatalysts for hydrogen evolution in an acidic medium. *J Mol Catal a-Chem* **2005,** *226* (2), 179-197.
27. Huot, J. Y.; Trudeau, M. L.; Schulz, R., Low Hydrogen Overpotential Nanocrystalline Ni-Mo Cathodes for Alkaline Water Electrolysis. *Journal of the Electrochemical Society* **1991,** *138* (5), 1316-1321.
28. McKone, J. R.; Warren, E. L.; Bierman, M. J.; Boettcher, S. W.; Brunschwig, B. S.; Lewis, N. S.; Gray, H. B., Evaluation of Pt, Ni, and Ni-Mo electrocatalysts for hydrogen evolution on crystalline Si electrodes. *Energ Environ Sci* **2011,** *4* (9), 3573-3583.
29. Kubisztal, J.; Budniok, A.; Lasia, A., Study of the hydrogen evolution reaction on nickel-based composite coatings containing molybdenum powder. *Int J Hydrogen Energ* **2007,** *32* (9), 1211-1218.
30. Birry, L.; Lasia, A., Studies of the hydrogen evolution reaction on Raney nickel-molybdenum electrodes. *J Appl Electrochem* **2004,** *34* (7), 735-749.
31. Chen, W. F.; Sasaki, K.; Ma, C.; Frenkel, A. I.; Marinkovic, N.; Muckerman, J. T.; Zhu, Y. M.; Adzic, R. R., Hydrogen-Evolution Catalysts Based on Non-Noble Metal Nickel-Molybdenum Nitride Nanosheets. *Angew Chem Int Edit* **2012,** *51* (25), 6131-6135.
32. McKone, J. R.; Sadtler, B. F.; Werlang, C. A.; Lewis, N. S.; Gray, H. B., Ni-Mo Nanopowders for Efficient Electrochemical Hydrogen Evolution. *Acs Catal* **2013,** *3* (2), 166-169.
33. Hu, H. Q.; Fan, Y. Z.; Liu, H., Optimization of NiMo catalyst for hydrogen production in microbial electrolysis cells. *Int J Hydrogen Energ* **2010,** *35* (8), 3227-3233.

34. Martinez, S.; Metikos-Hukovic, M.; Valek, L., Electrocatalytic properties of electrodeposited Ni-15Mo cathodes for the HER in acid solutions: Synergistic electronic effect. *J Mol Catal a-Chem* **2006,** *245* (1-2), 114-121.
35. Highfield, J. G.; Claude, E.; Oguro, K., Electrocatalytic synergism in Ni/Mo cathodes for hydrogen evolution in acid medium: a new model. *Electrochimica acta* **1999,** *44* (16), 2805-2814.
36. Ezaki, H.; Nambu, T.; Morinaga, M.; Udaka, M.; Kawasaki, K., Development of low hydrogen overpotential electrodes utilizing metal ultra-fine particles. *Int J Hydrogen Energ* **1996,** *21* (10), 877-881.
37. Minguzzi, A.; Alpuche-Aviles, M. A.; Lopez, J. R.; Rondinini, S.; Bard, A. J., Screening of oxygen evolution electrocatalysts by scanning electrochemical microscopy using a shielded tip approach. *Anal Chem* **2008,** *80* (11), 4055-4064.
38. Merilampi, S.; Laine-Ma, T.; Ruuskanen, P., The characterization of electrically conductive silver ink patterns on flexible substrates. *Microelectron Reliab* **2009,** *49* (7), 782-790.
39. Jahn, S. F.; Blaudeck, T.; Baumann, R. R.; Jakob, A.; Ecorchard, P.; Ruffer, T.; Lang, H.; Schmidt, P., Inkjet Printing of Conductive Silver Patterns by Using the First Aqueous Particle-Free MOD Ink without Additional Stabilizing Ligands. *Chem Mater* **2010,** *22* (10), 3067-3071.
40. Schultz, D. L.; Curtis, C. J.; Ginley, D. S. Direct Printing of Thin-Film Conductors Using Metal-Chelate Inks. US 6,830,778 B1, Dec. 12, 2004, 2004.
41. Sullivan, M. G.; Utomo, H.; Fagan, P. J.; Ward, M. D., Automated electrochemical analysis with combinatorial electrode arrays. *Anal Chem* **1999,** *71* (19), 4369-4375.
42. Feng, X. J.; Shankar, K.; Varghese, O. K.; Paulose, M.; Latempa, T. J.; Grimes, C. A., Vertically Aligned Single Crystal TiO2 Nanowire Arrays Grown Directly on Transparent Conducting Oxide Coated Glass: Synthesis Details and Applications. *Nano letters* **2008,** *8* (11), 3781-3786.
43. Fernandez, J. L.; Walsh, D. A.; Bard, A. J., Thermodynamic guidelines for the design of bimetallic catalysts for oxygen electroreduction and rapid screening by scanning electrochemical microscopy. M-Co (M : Pd, Ag, Au). *Journal of the American Chemical Society* **2005,** *127* (1), 357-365.
44. Bard, A. J.; Faulkner, L. R., Electrochemical Methods: Fundamentals and Applications. 2001 ed.; Wiley: New York, 2001.
45. Zhou, F. M.; Unwin, P. R.; Bard, A. J., Scanning Electrochemical Microscopy .16. Study of 2nd-Order Homogeneous Chemical-Reactions Via the Feedback and Generation Collection Modes. *J Phys Chem-Us* **1992,** *96* (12), 4917-4924.
46. Treichel, D. A.; Mirkin, M. V.; Bard, A. J., Scanning Electrochemical Microscopy .27. Application of a Simplified Treatment of an Irreversible Homogeneous Reaction Following Electron-Transfer to the Oxidative Dimerization of 4-Nitrophenolate in Acetonitrile. *J Phys Chem-Us* **1994,** *98* (22), 5751-5757.
47. Zhou, J. F.; Zu, Y. B.; Bard, A. J., Scanning electrochemical microscopy Part 39. The proton/hydrogen mediator system and its application to the study of the electrocatalysis of hydrogen oxidation. *J Electroanal Chem* **2000,** *491* (1-2), 22-29.
48. Sun, P.; Mirkin, M. V., Kinetics of electron-transfer reactions at nanoelectrodes. *Anal Chem* **2006,** *78* (18), 6526-6534.

49. Leonard, K. C.; Bard, A. J., The Study of Multireactional Electrochemical Interfaces via a Tip Generation/Substrate Collection Mode of Scanning Electrochemical Microscopy: The Hydrogen Evolution Reaction for Mn in Acidic Solution. *Journal of the American Chemical Society* **2013,** *135* (42), 15890-15896.
50. Noel, J. M.; Yu, Y.; Mirkin, M. V., Dissolution of Pt at moderately negative potentials during oxygen reduction in water and organic media. *Langmuir : the ACS journal of surfaces and colloids* **2013,** *29* (5), 1346-50.
51. Zhao, C.; Wittstock, G., Scanning electrochemical microscopy for detection of biosensor and biochip surfaces with immobilized pyrroloquinoline quinone (PQQ)-dependent glucose dehydrogenase as enzyme label. *Biosens Bioelectron* **2005,** *20* (7), 1277-1284.
52. Kaya, T.; Nagamine, K.; Oyamatsu, D.; Shiku, H.; Nishizawa, M.; Matsue, T., Fabrication of microbial chip using collagen gel microstructure. *Lab Chip* **2003,** *3* (4), 313-317.
53. Watanabe, H.; Velmurugan, J.; Mirkin, M. V.; Svirsky, M. A.; Lalwani, A. K.; Llinas, R. R., Scanning Electrochemical Microscopy as a Novel Proximity Sensor for Atraumatic Cochlear Implant Insertion. *IEEE Trans. Biomed. Eng.* **2014,** *61* (6), 1822-32.
54. Kim, J.; Izadyar, A.; Nioradze, N.; Amemiya, S., Nanoscale mechanism of molecular transport through the nuclear pore complex as studied by scanning electrochemical microscopy. *Journal of the American Chemical Society* **2013,** *135* (6), 2321-9.
55. Lee, C. M.; Kwak, J. Y.; Bard, A. J., Application of Scanning Electrochemical Microscopy to Biological Samples. *P Natl Acad Sci USA* **1990,** *87* (5), 1740-1743.
56. Lee, J. W.; Ye, H. C.; Pan, S. L.; Bard, A. J., Screening of photocatalysts by scanning electrochemical microscopy. *Anal Chem* **2008,** *80* (19), 7445-7450.
57. Rodriguez-Lopez, J.; Alpuche-Aviles, M. A.; Bard, A. J., Interrogation of Surfaces for the Quantification of Adsorbed Species on Electrodes: Oxygen on Gold and Platinum in Neutral Media. *Journal of the American Chemical Society* **2008,** *130* (50), 16985-16995.
58. Rodriguez-Lopez, J.; Bard, A. J., Scanning Electrochemical Microscopy: Surface Interrogation of Adsorbed Hydrogen and the Open Circuit Catalytic Decomposition of Formic Acid at Platinum. *Journal of the American Chemical Society* **2010,** *132* (14), 5121-5129.
59. Park, H. S.; Leonard, K. C.; Bard, A. J., Surface Interrogation Scanning Electrochemical Microscopy (SI-SECM) of Photoelectrochemistry at a W/Mo-BiVO4 Semiconductor Electrode: Quantification of Hydroxyl Radicals during Water Oxidation. *J Phys Chem C* **2013,** *117* (23), 12093-12102.
60. Sun, T.; Yu, Y.; Zacher, B. J.; Mirkin, M. V., Scanning Electrochemical Microscopy of Individual Catalytic Nanoparticles. *Angew Chem Int Edit* **2014,** *53*.
61. Chen, C. H.; Meadows, K. E.; Cuharuc, A.; Lai, S. C.; Unwin, P. R., High resolution mapping of oxygen reduction reaction kinetics at polycrystalline platinum electrodes. *Physical chemistry chemical physics : PCCP* **2014,** *16* (34), 18545-52.
62. Aaronson, B. D.; Lai, S. C.; Unwin, P. R., Spatially resolved electrochemistry in ionic liquids: surface structure effects on triiodide reduction at platinum electrodes. *Langmuir : the ACS journal of surfaces and colloids* **2014,** *30* (7), 1915-9.
63. Takahashi, Y.; Shevchuk, A. I.; Novak, P.; Zhang, Y. J.; Ebejer, N.; Macpherson, J. V.; Unwin, P. R.; Pollard, A. J.; Roy, D.; Clifford, C. A.; Shiku, H.; Matsue, T.;

Klenerman, D.; Korchev, Y. E., Multifunctional Nanoprobes for Nanoscale Chemical Imaging and Localized Chemical Delivery at Surfaces and Interfaces. *Angew Chem Int Edit* **2011,** *50* (41), 9638-9642.
64. McKelvey, K.; Edwards, M. A.; Unwin, P. R., Intermittent Contact-Scanning Electrochemical Microscopy (IC-SECM): A New Approach for Tip Positioning and Simultaneous Imaging of Interfacial Topography and Activity. *Anal Chem* **2010,** *82* (15), 6334-6337.
65. Laforge, F. O.; Velmurugan, J.; Wang, Y. X.; Mirkin, M. V., Nanoscale Imaging of Surface Topography and Reactivity with the Scanning Electrochemical Microscope. *Anal Chem* **2009,** *81* (8), 3143-3150.
66. Shen, M.; Ishimatsu, R.; Kim, J.; Amemiya, S., Quantitative imaging of ion transport through single nanopores by high-resolution scanning electrochemical microscopy. *Journal of the American Chemical Society* **2012,** *134* (24), 9856-9.
67. Wipf, D. O.; Bard, A. J.; Tallman, D. E., Scanning Electrochemical Microscopy .21. Constant-Current Imaging with an Autoswitching Controller. *Anal Chem* **1993,** *65* (10), 1373-1377.
68. Kurulugama, R. T.; Wipf, D. O.; Takacs, S. A.; Pongmayteegul, S.; Garris, P. A.; Baur, J. E., Scanning electrochemical microscopy of model neurons: Constant distance imaging. *Anal Chem* **2005,** *77* (4), 1111-1117.
69. Ghorbal, A.; Grisotto, F.; Charlier, J.; Palacin, S.; Goyer, C.; Demaille, C.; Brahim, A., Nano-Electrochemistry and Nano-Electrografting with an Original Combined AFM-SECM. *Nanomaterials* **2013,** *3* (2), 303-316.
70. Etienne, M.; Moulin, J.-P.; Gourhand, S., Accurate control of the electrode shape for high resolution shearforce regulated SECM. *Electrochimica acta* **2013,** *110*, 16-21.
71. Amemiya, S.; Kim, J.; Izadyar, A.; Kabagambe, B.; Shen, M.; Ishimatsu, R., Electrochemical Sensing and Imaging Based on Ion Transfer at Liquid/Liquid Interfaces. *Electrochimica acta* **2013,** *110*.
72. Guell, A. G.; Meadows, K. E.; Dudin, P. V.; Ebejer, N.; Macpherson, J. V.; Unwin, P. R., Mapping nanoscale electrochemistry of individual single-walled carbon nanotubes. *Nano letters* **2014,** *14* (1), 220-4.
73. Amemiya, S.; Bard, A. J.; Fan, F. R. F.; Mirkin, M. V.; Unwin, P. R., Scanning Electrochemical Microscopy. *Annual review of analytical chemistry* **2008,** *1*, 95-131.
74. Bard, A. J.; Mirkin, M. V., *Scanning Electrochemical Microscopy*. 2nd ed. ed.; CRC Press: Boca Raton, FL, 2012.
75. Bose, B. K., Expert System, Fuzzy Logic, and Neural Network Applications in Power Electronics and Motion Control. *Proceedings of the IEEE* **1994,** *822* (8), 1303-23.
76. Chang, J. H.; Leonard, K. C.; Cho, S. K.; Bard, A. J., Examining Ultramicroelectrodes for Scanning Electrochemical Microscopy by White Light Vertical Scanning Interferometry and Filling Recessed Tips by Electrodeposition of Gold. *Anal Chem* **2012,** *84* (11), 5159-5163.
77. Bourdillon, C.; Demaille, C.; Moiroux, J.; Saveant, J., Catalysis and Mass Transport in Spatially Ordered Enzyme Assemblies on Electrodes. *Journal of the American Chemical Society* **1995,** *117*, 11499-11506.
78. Zoski, C. G.; Aguilar, J. C.; Bard, A. J., Scanning electrochemical microscopy. 46. Shielding effects on reversible and quasireversible reactions. *Anal Chem* **2003,** *75* (13), 2959-2966.

79. Lacnjevac, U. C.; Jovic, B. M.; Jovic, V. D.; Krstajic, N. V., Determination of kinetic parameters for the hydrogen evolution reaction on the electrodeposited Ni-MoO2 composite coating in alkaline solution. *J Electroanal Chem* **2012,** *677,* 31-40.

APPENDIX: A

Source Code for Catalyst Dot Optimization Program

Using Microsoft Visual Studio Ultimate 2013, a program was written in C# language to determine the optimum precursor ink concentrations for accomplishing the most efficient print, using 4 inks, by finding the minimum number of depositions necessary. Then the program returns the optimum concentration set values with the number depositions from each ink at a given component percentage.

The following is the code for this program:

```
using System;
using System.Collections.Generic;
using System.Linq;
using System.Text;
using System.Threading.Tasks;

namespace Playground
{
    internal class Program
    {
        private static void Main(string[] args)
        {
            const int MAX = 100;

            var p = new List<int>();
            // List of all quadruplets that create the min amount of
                  drops req'd
            var lowestList = new List<Tuple<List<int>, Dictionary<int,
                  Dictionary<int, int>>>>();
            // The min amount of drops req'd
            int lowestAmount = int.MaxValue;
            int total = 0;

            var EvenNumbers = new List<int>();
            for (int i = 0; i <= MAX; i += 2)
            {
                EvenNumbers.Add(i);
            }
```

```
//Ensure p1 > p2 > p3 > p4 is always true. This fact is
      crucial to the 'algorithm'
for (var p1 = MAX; p1 >= 8; p1 -= 2)
{
    for (var p2 = p1 - 2; p2 >= 6; p2 -= 2)
    {
        for (var p3 = p2 - 2; p3 >= 4; p3 -= 2)
        {
            p = new List<int>() { p1, p2, p3, 2 };

            /* Loop through and keep hacking away at the
                  number. Should
                     * always end up with 0 based on initial
                        conditions. Better code would
                     * check that and throw error if not
                     */


            Dictionary<int, Dictionary<int, int>>
                  cachedResults = new Dictionary<int,
                  Dictionary<int, int>>();


            foreach (var number in EvenNumbers)
            {
                // Console.WriteLine("Point % = " + number);
                if (number == 0)
                {
                    cachedResults.Add(0, new Dictionary<int,
                        int>());
                    foreach (var p_i in p)
                    {
                        cachedResults[0].Add(p_i, 0);
                    }
                }
                else
                {
                    var min = int.MaxValue;
                    var minIdx = 0;
                    foreach (var p_i in p)
                    {
                        if (cachedResults.ContainsKey(number
                              - p_i) && cachedResults[number
                              - p_i].Values.Sum() < min)
                        {
                            min = cachedResults[number -
                              p_i].Values.Sum();
                            minIdx = p_i;

                        }

                    }
                    cachedResults.Add(number, new
                        Dictionary<int,
                        int>(cachedResults[number -
                        minIdx]));
                    cachedResults[number][minIdx]++;
```

```
                        }

                    }
                    /* If we tied the lowest score, add it to the
                          list of quadruplets. If we beat
                             * the lowest score, create new list of
                                quadruplets
                             */
                    total = cachedResults.Values.SelectMany(x =>
                          x.Values).Sum();

                    if (total == lowestAmount)
                    {
                        lowestList.Add(new Tuple<List<int>,
                          Dictionary<int, Dictionary<int, int>>>(p,
                          cachedResults));
                    }
                    else if (total < lowestAmount)
                    {
                        lowestAmount = total;
                        lowestList = new List<Tuple<List<int>,
                          Dictionary<int, Dictionary<int, int>>>>
                        {
                            new Tuple<List<int>, Dictionary<int,
                                Dictionary<int, int>>>(p,
                                cachedResults)
                        };
                    }
                }
            }
        }

        // Print winners
        Console.WriteLine(lowestAmount);


        foreach (var tuple in lowestList)
        {
            Console.WriteLine("p1 = {0}, p2 = {1}, p3 = {2}, p4 = 2",
              tuple.Item1[0], tuple.Item1[1], tuple.Item1[2]);
            foreach (var n in EvenNumbers)
            {
                Console.WriteLine("Point % : " + n);

                foreach (var tup in tuple.Item2[n])
                {
                    //Console.WriteLine("Point % : ");
                    Console.WriteLine(tup);
                 }

            }
        }
    }

    }
}
```

APPENDIX: B

Laboratory Procedures

1. GIX Print Code Generation

In order to have a successful print, the first step is to make sure all of the code for the print is correct, consistent, and in the desired order (i.e. correctly divided into print files, print features following the correct sequence, etc.). To generate the print code in a rapid fashion, a LabVIEW program was created. The purpose of this program is to read Excel files for sequence, print coordinates, and number of printed catalyst spots at each coordinate. The following process will get the correct output for your print features:

Catalyst Spot Print Code Generation:

Step 1: Take the results of the C# optimization program for number of depositions for each precursor at each spot and create a spreadsheet with these values cataloged by electrode number. This spreadsheet was created (for a bimetallic 2% increment with 4 precursor inks per metal salt) and stored on the SECM computer under the file path: C:\Users\SECM\Desktop\Sonoplot Generate Print File VIs\Catalyst Spot Plain.csv

Step 2: Make spreadsheet with coordinate values for each electrode number. This spreadsheet was created for multiple generations of electrode architectures. The most recent version when this was written is stored on the

SECM computer under the file path: C:\Users\SECM\Desktop\Sonoplot Generate Print File VIs\CatalystDotsCurrent.csv

Step 3: Use the LabVIEW program, selecting the correct .csv files for inputs. **NOTE: The LabVIEW program reads in the data based on cell number, and it ONLY reads integers, so if you have the .csv incorrectly formatted it may completely crash because of syntax.** Once the files are selected, the ink number must be specified (for the spreadsheets previously mentioned inks 1-4 are for bimetallic metal #1 precursors, while inks 5-8 are for the metal #2 precursors). Running the program will return the print code for the specified ink.

Step 4: From here the code needs to be separated into individual print files, because each spot needs to dry before a subsequent deposition is made. The LabVIEW program returns the print code header needed for a Sonoplot print, so it must be included with all print files. The best way to separate the files is to use the Mac Text Edit program or Windows Notepad to go through by hand and separate the ink specific code by number of catalyst spots, meaning all of the first dots for that ink are isolated into the first file; next, all of the spots that will require 2 or more spots will have the second layer in another file; then spots requiring 3 or more depositions will have the third layer in another file…..etc. until all of the print features are accounted for with that ink. **NOTE: Once the print order is correctly set, DO NOT save it through SonoDraw, since doing so will reorder the print randomly and undo all of the hard work required to ensure the**

correct print sequence. Any edits should be done through the Text Edit program.

Gold Electrode Wire Print Code Generation:

Generating the code for gold electrode architectures is not easy, as it requires high levels of concentration and detail oriented analysis to debug any issues that occur.

Step 1: First, the desired architecture of print lines for the electrodes must be created using SonoDraw. Depending on what architecture is created, the position of each feature position and dimension can be seen or modified by highlighting the feature and clicking on the "inspect element" option. In order to get the lines, spots, etc. all to line up correctly it will require setting these feature positions from this "inspect element" menu. Take note of every individual feature's start and end positions so that they can be identified within the print code later.

Step 2: Once the file is made and the architecture is correct, the next step is to reorder the print so that the electrode features print in sequence. SonoDraw likes to reorder the features in a random way, but to print these features they must be in the proper order to prevent issues. Therefore, the code must be opened in Text Edit or Notepad and reordered by hand to put the print features in the correct sequence by using the start and end positions of each element as an identifier. **NOTE: Once the print order is correctly set, DO NOT save it through SonoDraw again, since doing so will**

reorder the print randomly and undo all of the hard work required to ensure the correct print sequence. Any edits should be done through the Text Edit program.

2. **Sonoplot GIX Microplotter Desktop Operation – Tip Rinsing, Printing Guide**

Printing with the Sonoplot GIX Microplotter Desktop requires a developed "feel" of the system in order to become efficient and comfortable with operation. In order to obtain this "feel" for the system, it takes time and experience. There is no shortcutting this aspect of operation.

To complete a print certain procedures must be followed. The following procedures are general and apply to the specific printing processes across the board.

Part 1: Program and Printer Startup

To complete startup, first turn on the Mac computer controlling the printer. Second, turn on the printer (switch on the right side of the back panel on the printer). Third, turn on the electronic relay box (under the Mac screen, switch on the back right corner). Once all three of these have been completed, then the SonoGuide software can be opened (if there is an issue with a connection or one of the components is not turned on you will get an error message stating that communication with the printer is not working). You will be prompted to "Home" the printer: tell it to complete the "Home" procedure, which calibrates the zero point for the 3 different axes. Once the program is ready to operate, open up the

"Dispenser Calibration", "Dispenser Control", and "Solutions" windows from the menu on top of the "CCD Camera" image window. Also, open the diagnostic feedback window by accessing the top menu on the top of the screen: Dispenser → Show Dispenser Diagnostics. From here the status of the tip frequency reading can be seen in real time.

Part 2: Dispenser Tip Cartridge Connection

To connect a new dispenser tip cartridge, first the old one needs to be removed. This is accomplished by disconnecting the cord where it connects to the printer on the z-axis. Once it is disconnected, the cartridge can be removed by firmly gripping it on either side of the mount and gently (but firmly) wiggle it up and out of the friction fit holding it in place.

Once the old cartridge has been removed, replace with a new one, making sure that you do not damage the glass tip in the process of mounting the new cartridge in the friction fit mount. Once it is mounted, connect the cord to the port on the z-axis.

After installation, the camera will most likely need to be repositioned and focused on the new tip. To accomplish this, the best method is to sweep left and right looking for a shadow of the tip. If the tip is not found, adjust the height of the camera and sweep left and right again. Continue until the dispenser tip is found, then focus to the dispensing end of the tip.

Part 3: Motion Control, Printer Movements, and Setting Location Coordinates

The printer moves by means of motion controllers for each of the 3 axes, with sub 10 μm accuracy. The x-axis is increasing value left to right, the y-axis is back to front, and the z-axis is top to bottom. The software controls have a xy-axis control (right and left buttons are x-axis and top and bottom are y-axis) and a z-axis control (up/down). Each of these has a coarse and fine adjustment button where the values for each step size user controllable. **Note: Do not set step size above roughly ¼ of the estimated distance to travel to avoid guessing wrong and over travel and crashing the tip. Also, if you use a large step size to travel, as soon as that travel is done make sure to change step size back to something smaller to prevent accidentally traveling too far in another axis and crashing the tip.**

To save a location and its coordinates, simply go to the desired coordinates and click the "+" on the coordinates pane next to the "Manual Controls" window. Once the coordinates are saved, they may be named. **Note: To save from having to redo your positions when a new tip is installed, save a general version to speed up reconfiguring new locations. Example: for the ink well, set a location 5000 μm above the well in addition to the actual ink well location. This allows for a new tip to be installed, but if it is longer (and will crash if you tell it to go to the actual well location) you can simply go to the elevated general position and**

approach the well to make the newly configured location instead of having to do it all from scratch.

Part 4: Tip Frequency Calibration

To perform any printing, the system **MUST** be calibrated to sense the substrate surface. Otherwise it will not know when to print at the substrate surface and will crash the tip on the surface, breaking it. So a frequency calibration needs to occur any time the resonant frequency of the tip changes (this could be due to filling with ink, printing enough ink out of the tip to alter properties, the tip is polished, the ink is changed….etc.). To accomplish this, from the SonoGuide program menu above the camera feed, select "Dispenser Calibration" to open the calibration window, then click the "calibrate" button to perform the calibration procedure. In order to calibrate, the tip must not be in contact with any surface, as this would alter the frequency characteristics of the tip.

To ensure that the tip is calibrated, open the tip diagnostics (as mentioned in Part 1) and make sure the frequency reading line (red) is below the set-point line (blue). If it is not below the set-point line, the tip did not properly calibrate.

This procedure can be done during a print, but not while printing is happening. Only perform calibrations while the tip is not traveling or in contact with a surface or ink well. A good time to complete this function is right when the tip starts a

surface approach during the print, since at this point it will pause the approach to calibrate and then resume the approach once completed.

Part 5: Surface Approach (Find Surface)

An integral part of the printing process is the surface approach, since this is how the tip gets close enough to the substrate to print. It is also used in other procedures, such as the topographical mapping, finding the substrate for alignment, setting coordinates for ink wells, and other applications. Because of the broad scope of this process, it is an important one to understand fully.

First, make sure that the tip has been properly calibrated (see Part 4). Next, align the tip above the surface for approach (roughly a few hundred microns above) and click on the "Find Surface" option in the motion control window. The tip should begin its approach in 8 μm step sizes. Monitor the tip diagnostics (as discussed in Part 4) to ensure the tip is functioning properly. Once the tip contacts the surface the frequency reading line (red) should spike up above the set-point line (blue) and the automated system should cease the approach and retract roughly 10 μm from contacting the surface. If the tip contacts the substrate without the frequency reading tripping the set-point, there is most likely something wrong with the tip, which may require installing a new tip.

Part 6: Surface Cant and Topography Calibration

To perform a surface calibration, an empty dispenser tip must be used. This procedure uses a series of surface approach operations on a grid to determine any cant or irregularities on the substrate plane. To successfully accomplish this surface calibration the substrate must be aligned precisely to get an accurate reading. In order to align the substrate glass slide, magnets were used as a barrier on the steel stage on the edge line (make sure magnet placement does not interfere with the movement of the tip). This allows for the glass slide to be lined up with the machined flat on the stage. Once it is secured in place, the tip is approached to the surface and the tip is aligned with the top-left corner (TLC) of the glass substrate slide. The reason for this alignment is due to the printer performing operations from the origin of printing. From the point at which you begin printing or calibration, the printing happens in the positive x- and y-axis directions.

To begin the surface calibration once the tip is located at the proper origin (TLC), on the top menu of the SonoGuide program select the “Dispenser” menu and then click on “Surface Topography Mapping”. Once you enter in the dimensions of the print surface and the grid spacing size desired for the surface calibration, it is ready to start. As with the surface approach procedure, keeping an eye on the frequency diagnostics is necessary to ensure the tip correctly senses the substrate surface.

Part 7: Filling the Tip with Ink

To prepare the system to fill the tip with ink, first ensure that the ink well (Teflon watch glass) is secured on the print stage surface. Next, position the dispenser tip centered above the ink well and perform an approach to the surface (see Part 5). Once the surface is found, retract the tip roughly 400-600 μm above the surface and save the ink location (both in the "Manual Controls" window coordinates pane and in the ink solutions window discussed in Part 8).

To fill the tip, move the dispenser tip away from the ink well and add in the ink solution desired (a few hundred microliters should be enough, but it depends on the surface tension of the ink and how deep it sits in the ink well) and then use the saved ink well coordinates to return the dispenser tip to the ink well and submerge in the ink. The tip should fill with capillary action, however, if the tip is very small and the ink surface tension does not lend well to fast filling, capillary action can be jump started by using a quick "Spray" (discussed in Part 9) of about 0.2-0.4 seconds (voltage will depend on the solution and the tip). With low viscosity inks, the tip will likely fill quickly and must be watched closely to prevent over-filling and spilling out the top of the pipet tip. If the ink (mainly the gold or other high concentration inks) dries on the top of the capillary tip it may seal that end of the tip, preventing the ink from flowing out of the dispensing side of the tip.

Part 8: Setting Ink Parameters

To set the ink parameters, first open the "Solutions" menu from the "CCD Camera" image window. From this new "Solutions" window the following parameters can be set:

Solution Name – To set this, add a new ink by clicking on the "+" on the bottom left part of the window and name the solution. To change an existing name, double click on the name within the solution list.

Column, Row, Plate, Type – This allows for an ink array to be designed. This is not necessary in the printing this group has done to this point.

Coordinates – The location of the well for that given ink. To set these coordinates the tip must be positioned manually at the desired ink location and then click the "Use current coordinates as custom position" button at the bottom of the window. This will set the coordinates of the current dispenser position as the ink position.

Draw Distance per Reload – This relates to how much the dispenser will print before automatically returning to the ink well to refill the tip. There are two (2) options for this: **microns** – this applies to printing features such as lines and fills, limiting based on print distance covered; **droplets** – this applies to

printing spots or dot-type depositions, limiting based on the number of drops deposited.

Length of Reload – The length of dwell time set for the tip to remain submerged in the ink while refilling.

Time to Empty – How long the tip sprays in automatic dispenser cleaning procedures. This has rarely worked with our inks, so it is not used.

Rinse Cycles – The number of times a tip would be rinsed with a cleaning solvent during the automatic dispenser cleaning procedure. This has not been used with our research.

Part 9: Printing basics – Fluid Bridge, TLC, Spray

To accomplish a print, it is important to fully understand the system so that you may make on-the-fly adjustments and quickly troubleshoot issues as they arise. A few important concepts include how the printer indexes a given print based on location as well as what is critically important for the fluid ink to flow from the tip during printing.

Print Indexing – The first part of beginning a print requires lining up the substrate on which the print is occurring. The reason for this is that the printer moves in individual steps with each axis. Because of this, it indexes the print based off of an x-y grid requiring the substrate to be properly lined up with the x-y origin.

This index point occurs in the top left corner (TLC) of the rectangular glass microscope slides used in our printing, due to the print taking place in the positive quadrant of the x-y spatial plane. The location of the dispenser tip at the beginning of a print is seen as the origin of the x-y plane, hence starting at the TLC. If the print substrate is not lined up properly the printed features will be skewed on the substrate and reproducing print locations will not be repeatable on that sample.

Fluid Bridge – The key to the fluid ink flowing out of the dispenser is creating and maintaining a fluid bridge between the dispenser and the substrate. The dispenser tip does not maintain contact with the substrate during printing, since the fragile glass tip would break if it did contact the surface while moving. For the print to happen, the tip approaches the substrate surface until it contacts, at which point the fluid in the tip also contacts the substrate, and then the tip retracts roughly 10 μm to separate the fragile glass tip from the substrate. When this happens, the surface tension of the fluid ink in the tip draws it out of the tip and maintains contact with the substrate surface. This fluid bridge allows the ink to flow between the dispenser tip and the substrate while keeping a small gap between the two components. If this fluid bridge is not created, the surface tension of the ink will not allow the printer to flow the ink without erratic spraying. If the fluid bridge is having trouble establishing itself, using the “Dispense” function at a low voltage for a short time interval (0.2-0.4 seconds) can expand the meniscus of the ink on the tip slightly and in some cases create the required contact with the substrate to form the fluid bridge.

Spray Function – To perform the "Spray" function, first click on the "Control Dispenser" tab on the "CCD Camera" image window. This will open the "Dispenser Control" window. From this window, the "Spray" and "Dispense" functions are accessible. The "Dispense" function operates the piezoelectric in the tip to perform a controlled pumping of the ink for a set length of time at a moderate voltage and frequency. The "Spray" function also operates the piezoelectric but with higher voltages and higher pumping speeds, which gives a spraying of the ink rather than a controlled pumping. This is mostly useful for emptying the tip and rinsing or filling very small tips that require the "Spray" for efficient solvent rinsing.

Part 10: Rinsing Tip

To rinse the tip, first the ink must be evacuated from the tip. Using the "Spray" function can accomplish this with some inks, but others require the use of a Kimwipe touched to the tip to draw out the ink. This is a delicate process and requires a steady hand and some practice. Once the ink is evacuated, a proper rinsing solvent for the ink is the drawn up into the tip and then evacuated in the same manner. This process is repeated until the tip is clean. Never leave the tip filled with ink for any extended period of time, this will result in coagulating of the ink and jamming up the tip, likely ruining it.

3. Gold Ink Print Directions

Printing the gold requires a few intricate steps:

Step 1: Preparing the glass microscope slide substrate requires cleaning. Maintaining clean slides is paramount to the print going smoothly (organics, such as a finger print, will prevent the gold ink from coating the glass like it should), therefore, all handling of the slides requires wearing nitrile gloves to prevent contamination of the glass surface. To accomplish this cleaning, the slides are set in the acid bath overnight to remove all organics and other contaminations on the glass surfaces. While working with the acid bath, wear proper gloves, eye protection, and a lab coat. Once the slides are cleaned, remove them from the back with forceps and rinse well with DI water, dry with a Kimwipe, and then use compressed argon or nitrogen to remove any leftover dust from the Kimwipe. **DO NOT use any of the in-line compressed air from the hoods, only use the tank gases to avoid issues with oils and debris in the compressed air line contaminating the slide!** To prepare the gold ink, combine the Bright Brushing Gold ink with tetrachloroethylene in a 5:4 ratio (BBG:TCE).

Step 2: Now that the slide is prepped for printing, the next step is to make sure the print files are correct and ready (see Section 1) and align the slide for printing and map the topography (see Section 2 Part 6). Once aligned and the TLC is set, retract 300 μm from the surface of the substrate and begin the print.

Step 3: During the print, be ready to use the "Dispense" function to help the fluid bridge form if the tip is having trouble doing so on approach. If a print feature is missed, take note of which one it is, then at the end of the print a new print file with that feature can be made to fill in the missing feature.

4. Ethylene Glycol Ink/Precursor Solutions: Fabrication and Printing

To make the metal precursor inks, a metal salt for the desired metal is dissolved in ethylene glycol. Depending on the concentration ratios desired and the individual salts, the procedure will vary for each ink. Following the procedure described in this thesis should be sufficient, however slight heating, sonication or vortex mixing may help with faster dissolving of the salts into solution.

For printing the precursor inks, the print files generated in Section 1 should be prepped and ready. Once the files are ready, the slide must be aligned properly and the topography mapped (see Section 2 Part 6). After all prep is complete, the ink should be fed into the tip, then the TLC alignment should be verified. Printing is now ready to commence. Make note of all printed dots with a check or fail marking to catalog any missed prints so that they can be reprinted if need be.

5. PMMA Solution: Fabrication and Printing

The insulating polymer solution requires some preparation. To create this solution, 0.125 g/L of poly(methyl methacrylate) (PMMA) in tetrachloroethylene (TCE) is prepared in a vial. The PMMA requires help dissolving in the TCE. To speed up

dissolving, a water bath of 90 °C (stirred) in a beaker is used to heat the PMMA and TCE mixture (also stirred in a vial, covered bun not sealed! Don't make a pressure bomb!!). Once the PMMA and TCE mixture is mixed at temperature for 3 hours, the PMMA crystals should be dissolved. Remove from heat, allow the solution to cool to room temperature, and seal the vial for storage.

Printing the PMMA is more difficult than the other inks due to the low viscosity making it splay out further and less predictably on the substrate. Be wary of what is being covered with this printing, since it can be hard to see (the TCE evaporates rather quickly, making the swath of coverage difficult to gauge at times), and make sure the catalyst spots aren't being covered by the insulating solution.

6. Pulling and Installing Replacement GIX Dispenser Tips – Sutter P2000

Making new capillary tips for the Sonoplot GIX Microplotter Desktop is important, since they are the main high-wear part on the printer and are a general maintenance procedure for the tool. To make these tips, the Sutter P2000 laser pipette puller is used to pull borosilicate capillary tubes into micropipettes. If used properly, 4-6 pipettes can be made from each capillary tube. The program settings used with the printer for this procedure is as follows:

HEAT=260, FIL=3, VEL=45, DEL=200, PUL=

HEAT=230, FIL=4, VEL=45, DEL=200, PUL=

HEAT=245, FIL=3, VEL=30, DEL=200, PUL=

Using these settings in a 3-line program the puller will make tips that are roughly 30-40 microns at the tip, sometimes smaller.

Once the tips are made, a wire cutter/stripper is used (with the stripper notch size slightly smaller than the capillary tube) to trim down the pipette tip to roughly 1-1¼" long (take note of the length of the previous pipette tip). The trimmed tip can then be installed on the dispenser cartridge. First, remove the old tip from the cartridge (apply pressure at the junction of the super glue between the tip and the piezoelectric element with a fingernail and gently pry, it should pop off). With the cartridge setting on the counter top, piezoelectric up (with the edge where the pipette attaches facing straight up), apply a SMALL drop of Duro super glue to the piezoelectric element surface (just enough to whet the edge where the pipette attaches) and gently place the pipette on top of the glue. The glue should pull it into place and hold it. Make sure it is only in contact with the piezoelectric, not any part of the cartridge. Allow the glue to dry overnight.

When using a new tip, it is likely too small to print the features required for the purposes of this lab, so some fine polishing of the tip will help to remove material up the taper to provide a larger tip size. In addition, polishing back the tip will provide a more symmetric tip with a flat face, making printing more reliable. To perform this polishing, first attach the new dispenser tip cartridge to the printer and focus the camera on the tip. Draw some ethanol up into the tip. Use a section of one of the micropolishing grit discs from the electrode polishing station to GENTLY

polish back the tip by hand. The process can be viewed as it happens on the camera at the small scale of the tip. Simple side-to-side motions should accomplish the polishing (limiting the motion to a minimum will help to prevent accidental tip breakage). The ethanol is important because it whets the polishing to prevent binding issues as well as preventing glass shavings from making their way into the tip and causing issues.

7. Maintenance for GIX – Replacing Tensioner O-ring for z-axis

At times, the tensioner O-ring on the GIX Microplotter may wear out. To replace this O-ring, first remove the roller that the O-ring rides on, using the proper allen wrench. Once the roller is removed from the z-axis guide arm, the O-ring can be removed and replaced. Position the new O-ring on the far side of the brown positioning feature on the roller (so that the O-ring is lined up on the mount side of the brown feature in the roller, not the screw head side). The O-ring should settle into the recess on the side of the brown feature. The tricky part is installing the roller: first, make sure the roller remains flush against the mounting surface while installing, DO NOT have it flush with the screw head, since this will result in the roller moving with the screw during installation and the O-ring binding on the z-axis arm. Place the roller in place on the mount, apply slight pressure from the right side of the roller to apply some crush on the O-ring in order to get the hole in the roller with the screw hole in the mounting surface, only then should the screw be inserted and tightened. While tightening the screw, make sure the roller is

completely stationary and flush against the mount to prevent binding and stretching the O-ring (if stretching occurs, the O-ring is most likely ruined).

8. Firing Printed Slides in Barnstead 4800 Box Furnace

After the gold slides and oxide catalysts are printed, they need to be fired under air in a box furnace. For the Barnstead 4800 Box Furnace, the following settings are needed for a successful bake:

Temperature – To set the baking temperature of the dwell period, scroll through the top menu (using the page button on far left of controller) until the current temperature is displayed (if the oven is cooled to room temp this should be 21-25 °C). Once the temp is displayed, pressing the up/down arrow buttons will bring up the dwell temp setting momentarily, adjust it accordingly.

Program – To set the correct program, first the menus need to be navigated to the program submenu. Use the page button (far left) to scroll through the top menu until it reads “SP”, then press the submenu button (the second from the left, looks like a circular arrow) repeatedly until the display reads “tmOP” which is the timer operating program, press one of the arrow buttons to enter this parameter menu. Once in the program menu, use the

arrow buttons to change the program until the display reads “Opt.1” for the correct program (ramp/dwell/switch off).

Ramp Rate – Setting the ramp rate is accomplished by accessing the “SP” submenu just as in the **Program** section and using the submenu button to scroll through until the display reads “SPrr”, and set the value using the arrow buttons to the desired value in units of °C/min.

Dwell Time – Setting the dwell time of the bake is accomplished by accessing the “SP” submenu just as in the **Program** section and using the submenu button to scroll through until the display reads “dwEll", and set the value using the arrow buttons to the desired dwell time at the set dwell temperature in units of hr:min.

Operating Status – To initiate the bake, the operating status must be reset, first off then on to start the procedure. This is accomplished by accessing the “SP” submenu just as in the **Program** section and using the submenu button to scroll through until the display reads “StAt”, and set the value using the arrow buttons to “OFF”, then exit to the top menu and access the “StAt” parameter menu again, but this time setting it to “On” and exiting to the top menu. The light on the front of the oven should start flashing and the temperature should soon begin to rise at the ramp rate.

9. Firing Printed Slides in Tube Furnace Under H_2

The tube furnace is what is used to fire the precursors in a way to reduce the metal ions in the salts to metallic compounds. The process is potentially dangerous, due

to the use of H_2 gas and high temperatures. If a safe mixture of inert and H_2 is being used, the process will have lower overall possibility of risk. Nevertheless, since high temps are present with H_2 gas, and potentially hazardous byproducts, proper safety attire is **REQUIRED** for this procedure (eye protection, lab coat, hair restrained and not loose, long pants, and gloves at a minimum).

Step 1 – For the first step, the slides/samples ready to fire must be certified that firing is the next step (no PMMA printed yet, but all catalysts have been printed). From this point, make sure that the tube furnace and components are ready for firing. This is accomplished by verifying that all pieces are present (ceramic tube, 2 steel end plates, 2 rubber gasket seals, 2 insulating plungers, ceramic kiln blocks). Check the ceramic tube to ensure there are no cracks or reasons for concern over the integrity of it.

Step 2 – Transport the tube, components, and the samples to the room with the tube furnace. The easiest way to set up the furnace for a print without damaging the samples is to rest the ceramic tube in the furnace harness, leaving the top open and the furnace off, and then remove the end caps and the insulating plungers. Once the tube is empty, place a sample/slide centered on top of a ceramic kiln block and place in the tube, ensuring that it is level and the slide is still centered. Once in the tube, use the insulating plunger to gently and slowly push the kiln block into position so that the insulating plunger is also fully inside of the tube. If at any point you hear the slide/sample slip off of the kiln block stop immediately and remove the plunger and the block, then once the sample is the only thing remaining in the tube, tip the tube to allow the sample to slide out. (**Note:** Due to the curve of the

tube, even a face-down sample should not be harmed by this, since it is sliding on the very edge of the slide where no printing has occurred.) Once the first sample is in place, repeat with subsequent samples (preferably from the other end of the tube) and take care not to knock any samples off of the blocks, because you will have to take everything out and restart the process.

Step 3 – Once all of the samples are in place and the plungers are fully inserted into the tube, install the downstream end cap with the rubber gasket and connect to the silicon oil 1-way flow trap. Then connect the system end cap (with the gas feed tube attached to it) with the gasket for that ceramic tube (not the dirty one that is there for other groups). Tighten the end caps firmly. Test the seal of the gaskets by flowing roughly 100 ccm of N_2 gas through the tube and watching the flow trap at the end for bubbles. They should correspond to the flow rate going into the tube.

Step 4 – After the system is ready, turn on the power for the furnace by flipping on both top switches on the control box (to the right). Next, set the furnace bake procedure with the controls box. It allows up to 8 steps, so step through the menu options and set the ramp rate unit as desired (previously min has been used), then set the dwell time unit (previously hr has been used), then set the ramp rate, bake temp, and dwell time for step 1 (previously RR = 3 °C/min, Temp = 150 °C, dwell = 0:30 hr). Then do the same for step 2 (previously RR = 3 °C/min, Temp = 300 °C, dwell = 3:00 hr). And again for subsequent steps (previously steps 3-8 RR = 0 °C/min, Temp = 0 °C, dwell = 0:00 hr resulting in the furnace shutting off and cooling to ambient temperatures) (when it has ID leave it at 0). When the program settings are input, then close the top half of the furnace and latch it shut. Then turn

on the N_2 flow to roughly 100 ccm (to purge the tube of all oxygen) and begin running the heating program by pressing both up/down arrow keys simultaneously. The light should start flashing on the controls box to indicate heating and the temp should soon begin to rise. Once the step 1 dwell is half way done, turn off the N_2 flow and begin the H_2 flow (previously 100 ccm). Check the system as the temp changes to ensure the flow rates are as expected. Adjust flow with the flow meter, not the tank regulator. Allow the H_2 flow to continue through step 2 and into the ambient cooling until it drops below 200 °C, then switch back to N_2 flow to purge the tube of H_2 and allow it to continue cooling to room temp. Do not open tube until it is down to room temp, because elevated heat in open air may cause unwanted oxidation of the metals. Once cooled, disassemble the tube, trying to remove the samples while keeping the tube flat and level.

10. Rapid Scanning Experimental Setup and Procedure

To set up the rapid scanning experiments, the following steps must be followed.

Step 1 – Make sure the sample is complete and ready to test. Use Ar gas to remove any dust or debris from the slide without touching any of the catalyst samples.

Step 2 – Remove the base plate from the rapid screening cell and correctly align the slide in its place (the top plate has the electrode numbers on marked, but to ensure that it is lined up properly with the PTFE section make sure that the red line on each of the parts line up). Secure the acrylic base plate to seal the slide in place.

Step 3 – Boot up the computer, turn on the potentiostat and ensure connections (both the potentiostat and the NI control box should be connected to the computer

via USB). On the computer, open the Rapid Screening VIs folder on the desktop and then open the CVMain LabVIEW file. Once in LabVIEW, set the parameters for the measurement just as with the CH software for the potentiostat, set the location for where the .tdms data file will save, and set the order of electrode numbers to be run (default is ascending numerical order, flip the switch on the top left to go in descending numerical order, or use the left pane to set a custom order to run from the top to bottom values as input).

Step 4 – Prepare the electrolyte solution by purging roughly 30 mL with Ar gas for 10 minutes, removing all non-inert gases. Cover the top of the cell top plate with parafilm, but have a small hole for each of the counter and reference electrodes and the Ar purge needle (See following pictures for visual example of experimental setup). Pipet the electrolyte into the cell through one of the parafilm holes, up to the top of the solution well, making sure not the flood any of the electrode lugs on top. Once the electrolyte is in place, set the reference electrode in the solution (make sure there are no bubbles on the base of the reference, securing it in place with a ring stand clamp), and then position the counter electrode (use a pipet to push it down into the electrolyte once the potentiostate clip is connected to the Pt counter and secured in the ring stand clamp). It is difficult to get this in place, but practice and patience will make it easier. Then use a second ring stand with a clamp to hold the Ar purge needle in place within the headspace (with a small flow of roughly 40-60 ccm), taking care not to have the needle flexed under tension against the parafilm (this may pull the parafilm off of the top of the cell causing oxygen to invade).

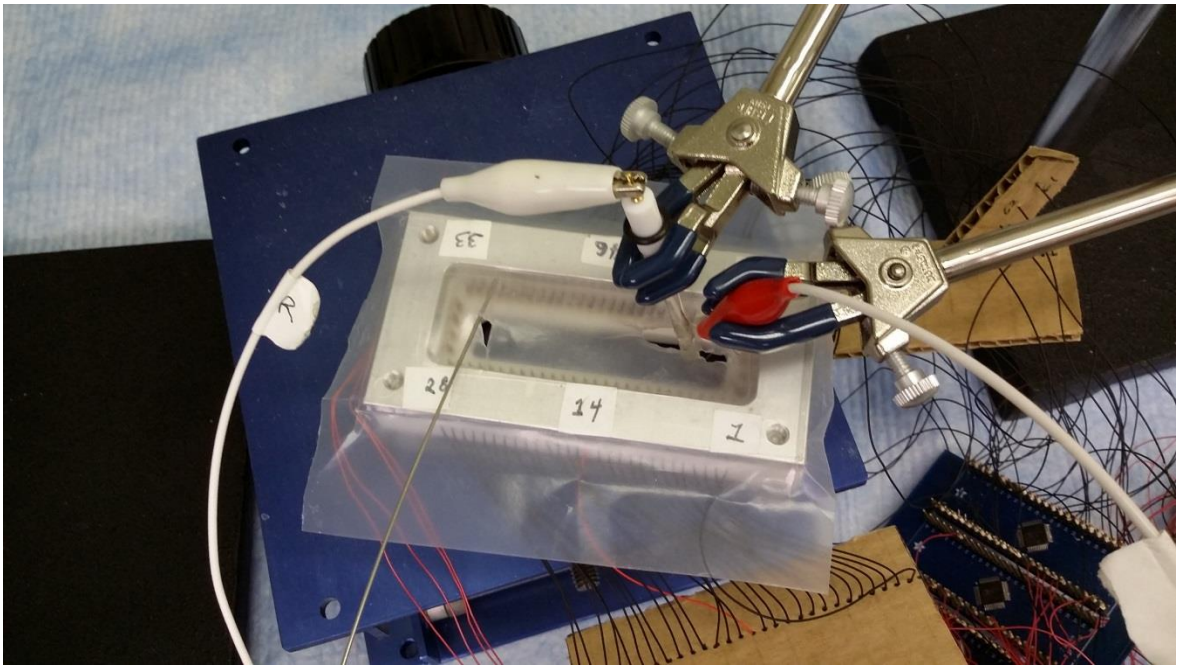

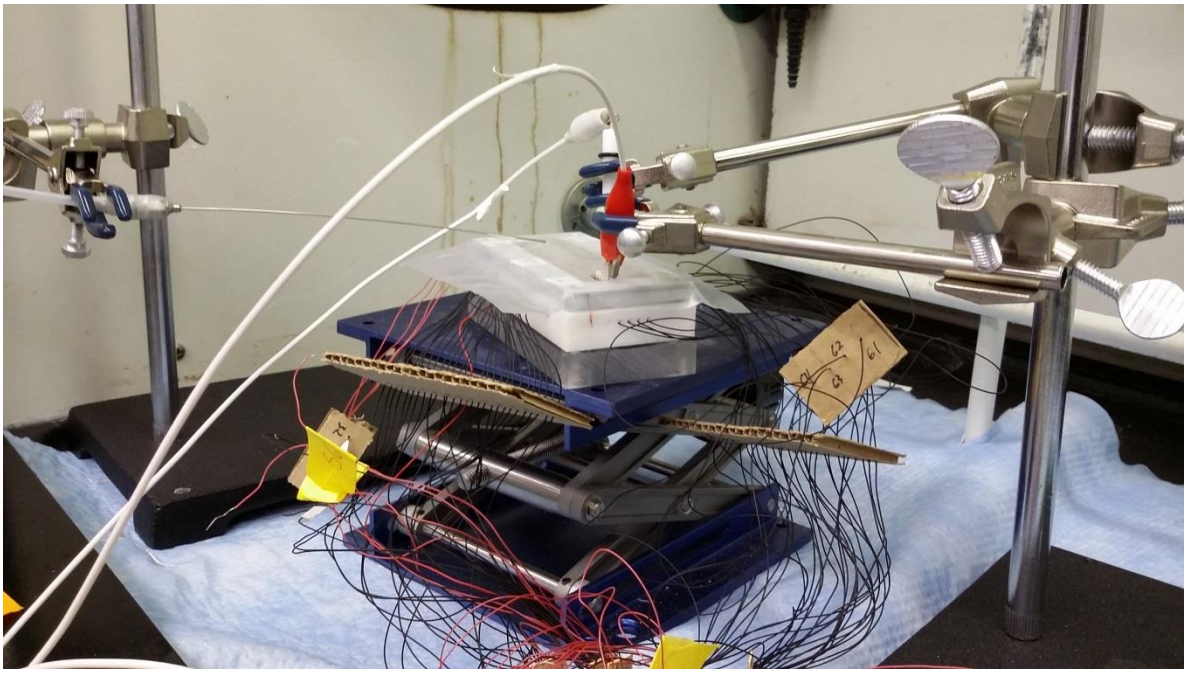

Step 5 – Connect all electrodes to the potentiostat (Green (working) = 2 joined black wires from controls box marked working, Red (counter) = counter electrode in electrolyte, White (reference) = Ag/AgCl reference electrode in electrolyte,

Black (ground) not connected to anything) and make sure none of the connections are grounded out on anything (taping them in place sometimes helps). Once all connections and setup is verified to be complete, the program is ready to run. First triple check that the file path for saving the data is correct and not that of a past experiment (it will overwrite your previous data if you forget to update the file name between runs). Click the "run" button to start measurement, and keep an eye on the first few LSVs to make sure the connections are good and the experiment is working.

11. Pulling UMEs – Procedures

Pulling UMEs requires lots of trial and error to develop a good program, and changing the capillary and/or the electrode wire will change what program works best for that pull procedure. In our work we have developed the following programs that work best for each of the specific electrodes we make:

200 µm – Use a quartz 0.3 mm ID/1.0 mm OD capillary and 200 µm diameter Pt wire with the following program: 1 line program

HEAT=850, FIL=1, VEL=50, DELAY=100, PULL=225

10 µm – Use a borosilicate 0.5 mm ID/1.0 mm OD capillary and 10 µm diameter Pt wire with the following procedure:

Step 1: 5 line program to stretch the capillary

HEAT=300, FIL=4, VEL=14, DELAY=120, PULL=0

HEAT=300, FIL=4, VEL=14, DELAY=120, PULL=0

HEAT=300, FIL=4, VEL=14, DELAY=120, PULL=0

HEAT=300, FIL=4, VEL=14, DELAY=120, PULL=0

HEAT=0, FIL=4, VEL=14, DELAY=120, PULL=0

Step 2: 1 line program repeated 8 times with 5 second intervals

First install razor blades as stoppers to prevent the puller from pulling, since the aim is just to heat the glass to seal around the wire.

HEAT=320, FIL=4, VEL=12, DELAY=120, PULL=0

Step 3: 1 line program, same as Step 2, but without the razor blade stoppers, allowing the pull to occur.

HEAT=320, FIL=4, VEL=12, DELAY=120, PULL=0

The results of this procedure for the 10 μm UMEs will actually return < 1 μm sized electrode tips, but polishing back the tip will increase the size to an intermediate value.

100 μm Gold – Use a borosilicate 0.5 mm ID/1.0 mm OD capillary and 200 μm gold wire with the following program: 1 line program

HEAT=450, FIL=4, VEL=50, DELAY=175, PULL=50

Electrode Polishing Techniques

To polish the UMEs, the techniques will vary depending on the size of the electrode:

200 µm – For these electrodes, using quartz capillaries has been the norm, so using the grit paper to shave back the glass and the wire works best to level off the tip, but it takes a while. Once the tip is leveled with the grit paper, the alumina micro polish is used to finish the polishing process, requiring heavy use of the 1 µm alumina to buff out the coarse cuts from the grit paper. Once smoothed, moving to the finer polishes will give a mirror-like finish.

10 µm – For these electrodes, using the grit paper is rarer, since the tapered glass at the tip is super fragile. More often, the polishing simply entails taking the pulled electrode and using light polishing with the alumina polishes to level off the tip.

12. Sutter P-2000 Laser Puller Maintenance – Gold Mirror Cleaning

Cleaning the mirror on the laser puller is simple. To access the mirror, first make sure the unit is off and that the laser will not turn on, then remove the two screws on either side of the laser pulling block (in the middle, where the capillary goes through). Once the screws are removed, the cover of the mirror should just lift up and off to expose the mirror. Take a Kimwipe and spray some ethanol on it, then wipe the concave face of the gold mirror with the ethanol to clean off the surface

(some firm scrubbing may be needed, but do not apply torque on the mirror without supporting it, you don't want to affect alignment in any way) and then use a dry Kimwipe to dry it off. Once clean, replace the cover and screws.